STUDIA

UNIVERSITATIS BABEŞ-BOLYAI

PHYSICA

1

1988

CLUJ-NAPOCA

ANUL XXXIII 1988

STUDIA

UNIVERSITATIS BABEŞ-BOLYAI

PHYSICA

1

Redacţia: 3400 CLUJ-NAPOCA, str. M. Kogălniceanu, 1 Telefon ● 1 61 01

SUMAR — CONTENTS — SOMMAIRE

IOAN URSU

Professor Ioan Ursu, member of the Academy of the S R of Romania, Romanian physicist of high national and international renown, a prominent son of his Cluj homeland, has come into the 60th year of his life Founder of the research in Solid State Physics in Cluj-Napoca as well as of the Romanian school of magnetic resonances, initiator of the research on laser active media, solid state lasers, resonant and non-resonant interaction of laser radiation with matter, particularly active in the field of nuclear materials and nuclear power, and originating several major projects in the field of isotope separation, Ioan Ursu has brought an important contribution to the development of Physics in our country.

An offspring of the schools and the University in Cluj, Professor Ursu has started his research career in the local Division of the Institute of Atomic Physics —

IFA, originally doing investigations on transport phenomena in gases. Selected results obtained at that time were gathered in his monograph Efecte magnetomecanice la oxigen *(Editura Academiei, Bucharest, 1959). Subsequently the study of gas/solid interface phenomena was approached, with particular emphasis on the catalysis of the hydrogen-deuterium isotopic exchange.*

Beginning with the year 1957, Ioan Ursu has much contributed to the development of Solid State Physics at the University of Cluj and at IFA—Cluj, guiding the research geared to the understanding of the gas/solid interface phenomena, of the electric, magnetic and structural properties of solids, as well as to the many-sided investigation of radiation effects on solids Drawing upon his own results and turning to the best account the experience gained during his dynamic interaction with renowned laboratories worldwide, Professor Ursu laid firm principial and methodological grounds to this research enterprise. Classic measurement techniques such as X-ray diffraction, magnetic susceptibility and electric, and thermal, conductivity determinations were soon to profitably compete with modern methods that were brilliantly and most efficiently implemented through Professor Ursu's efforts; among these — the electron paramagnetic resonance, the nuclear magnetic resonance, the electron microscopy and others. The results obtained through his work at the University of Cluj as well as with various renowned laboratories in the USSR, USA, GDR, Switzerland were soon recognized as important scientific achievements. Over the years, these brought increasing praise on behalf of the international expert community to the Romanian school of radio-frequency spectroscopy, thereby created.

In recognition of his outstanding scientific merits, in 1963 Professor Ioan Ursu has been elected a corresponding member of the Academy of the S.R of Romania, to become full member in 1974. He held offices with the steering bodies of the international societies AMPERE and ISMAR, ever since their foundation. In 1976 Professor Ioan Ursu has been elected President of the European Physical Society The good name the Romanian Physics owes to Professor Ursu has been time and again confirmed, by the establishment in our country of the Summer School of the international Groupment AMPERE (Atomes et Molécules par Etudes Radio—Electriques) — the first of the kind, by the organizing of the 16th AMPERE Congress, of the 7th AMPERE Specialized Colloque, of the 3rd General Conference of the European Physical Society, as well as of the international series of Conferences "Trends in Quantum Electronics", hosted by the Central Institute of Physics, at their 3rd edition this fall

The main contributions by Professor Ioan Ursu in the field of electron paramagnetic resonance and nuclear magnetic resonance are gathered in the books Rezonanţa electronică de spin *(Editura Academiei, Bucharest, 1965),* La resonance paramagnétique électronique *(Dunod, Paris, 1968),* Rezonanţa magnetică în compuşi cu uraniu *(Editura Academiei, Bucharest, 1979),* Magnitny rezonans v soyedineniah urana, *(Energya, Moscow, 1982). Ioan Ursu has also brought outstanding contributions to other, modern and important, domains of Physics, such as the Nuclear Physics, Laser Physics, Surface Physics, the Physics of high technologies and new materials a.o His work in these fields is illustrated by books such as* Energia atomică *(Editura Ştiinţifică, Bucharest, 1973),* Fizica şi tehnologia materialelor nucleare, *(Editura Academiei, Bucharest, 1982),* Physics and Technology of Nuclear Materials *(Pergamon Press, Oxford, 1985), and* Interacţiunea radiaţiei laser cu metalele *(Editura Academiei, Bucharest, 1986).*

Professor Ioan Ursu has much contributed to the organizing and sound evolvement of the Physics educational system in Cluj, as Dean of the Department of Mathematics and Physics, and then Vice President of the University of Cluj-Napoca. Great many students among those who were privileged to enjoy his teaching and the influence of his charismatic personality were to be assigned tasks and public responsibilities commensurate with the skills their mentor knew to reveal and educate in them, with unparalleled didactic and pedagogic talent. The academic life in Cluj, as well as the Romanian Physics in general, were always given the considerate attention and support by Professor Ursu, during the years of his serving as Director General of the Central Institute of Physics in Bucharest, President of the State Committee for Nuclear Energy, President of the National Council for Science and Technology, and First Vice President of the National Committee for Science and Technology.

Professor Ioan Ursu has always demonstrated profound care for the public needs, and dedication in their solutioning. He is a member of Romania's Great National Assembly.

Ioan Ursu is the son of Ioan Ursu and Ana Ursu. He is married to Lucia Ursu. They have three children.

At his 60th Birthday, we heartedly wish Professor Ioan Ursu many happy returns, an ever sound health and strength, and new, accomplished successes in the many-sided activity that he devotes to the Physical Sciences in the benefit of Romania's progress and welfare.

THE EDITORIAL BOARD

STUDIA UNIV BABEŞ-BOLYAI, PHYSICA, XXXIII, 1, 1988

MAGNETIC BEHAVIOUR OF THE Ni—Pt ALLOYS

I. POP* and H. LITSCHEL**

Dedicated to Professor IOAN URSU on his 60 th anniversary

Received February 10, 1988

ABSTRACT. — The magnetic behaviour of the $Ni_{1-x}Pt_x$ alloys ($x = 1, 2; 3, 4, 5, 8, 10, 15, 20, 25, 30$ at %) has been investigated It was pointed out that the temperature dependence of the spontaneous intensity of magnetization satisfies the $T^{3/2}$ law in the temperature range $0 \div 0.4\ T_c$, and T^2 law between $0.4\ T_c - 0.7\ T_c$ The concentration dependence of the magnetic moment values per alloys atom is linear only in the low domain of concentrations The extrapolated values for pure nickel and for pure platinum atoms are in good agreement with other earlier reported data

Introduction. The magnetic properties of the Ni—Pt alloys can be explained in a similar way as in Ni—Rh, Ni—Pd and Pd—Pt alloys by using the magnetic environment model [1,2] and coherent potential approximation as well [3] The reported experimental results concerning temperature dependence of the spontaneous magnetization for $Ni_{53.3}\ Pt_{46.7}$ showed a T^2 dependence of this quantity [4], while for the concentration higher than 40 at % Pt the $T^{3/2}$ law was found [5]. The linear concentrations dependence of the magnetic moment [6] is confirmed only for the low concentrated Ni—Pt alloys [7] In order to study the transport phenomena in the Ni—Pt alloys, we have also investigated some magnetic properties of the system to which this paper is devoted.

Experimental. The samples $Ni_{1-x}Pt_x$ (x = 1, 2, 3, 4, 5, 8, 10; 15, 20; 25; 30 at %) have been prepared by electric arc melting furnace under pure argon atmosphere from the high purity base-metals. In order to obtain homogenous solid solutions, the samples have been annealed at 1,173 K during 24 hours. The temperature dependence of the specific intensity of magnetization using a Weiss—Forrer balance type, having a 10^{-8} e m u sensivity, relative to pure Ni value of the magnetization

Experimental Results and Discussion. Some of the obtained experimental results $\sigma = f(H)_T$ are presented in Fig 1 By extrapolation of the linear part of the isotherms for H=0, we obtained the spontaneous intensity of magnetization values. The temperature dependence of the spontaneous intensity of magnetization for all investigated samples is given in Figs. 2 and 3.

In order to see which model is more appropriate to describe the $Ni_{1-x}Pt_x$ metallic system, we plotted in Fig. 4 the dependence of the spontaneous intensity of magnetization versus $T^{3/2}$. One can see from the figure that this depen-

* *Departament of Physics, Cluj-Napoca University, 3400 Cluj-Napoca, Romania*
** *Technical Institute of Sibiu, B-dul Victoriei, no. 5, 2400 Sibiu, Romania*

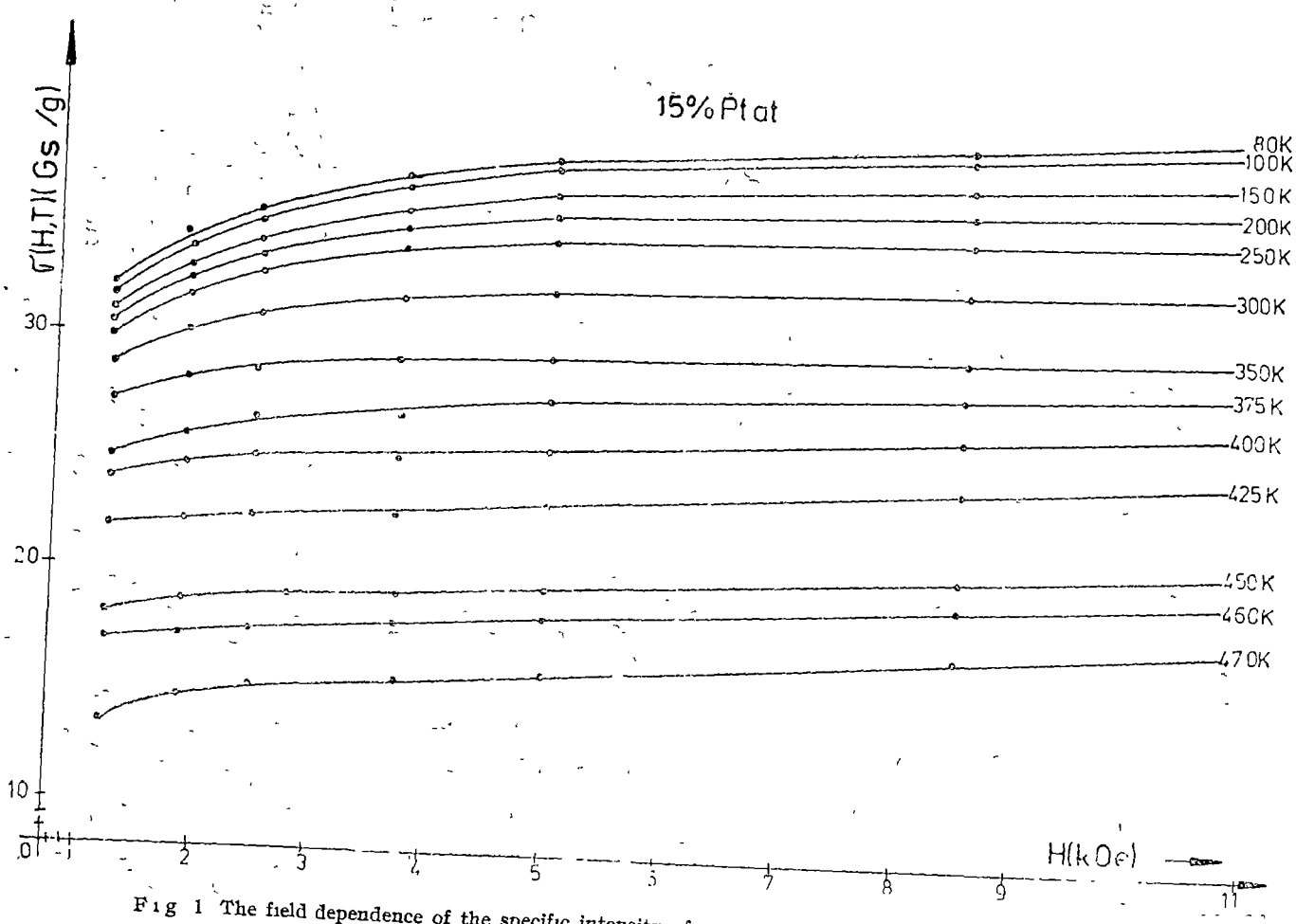

Fig 1 The field dependence of the specific intensity of magnetization for different temperatures

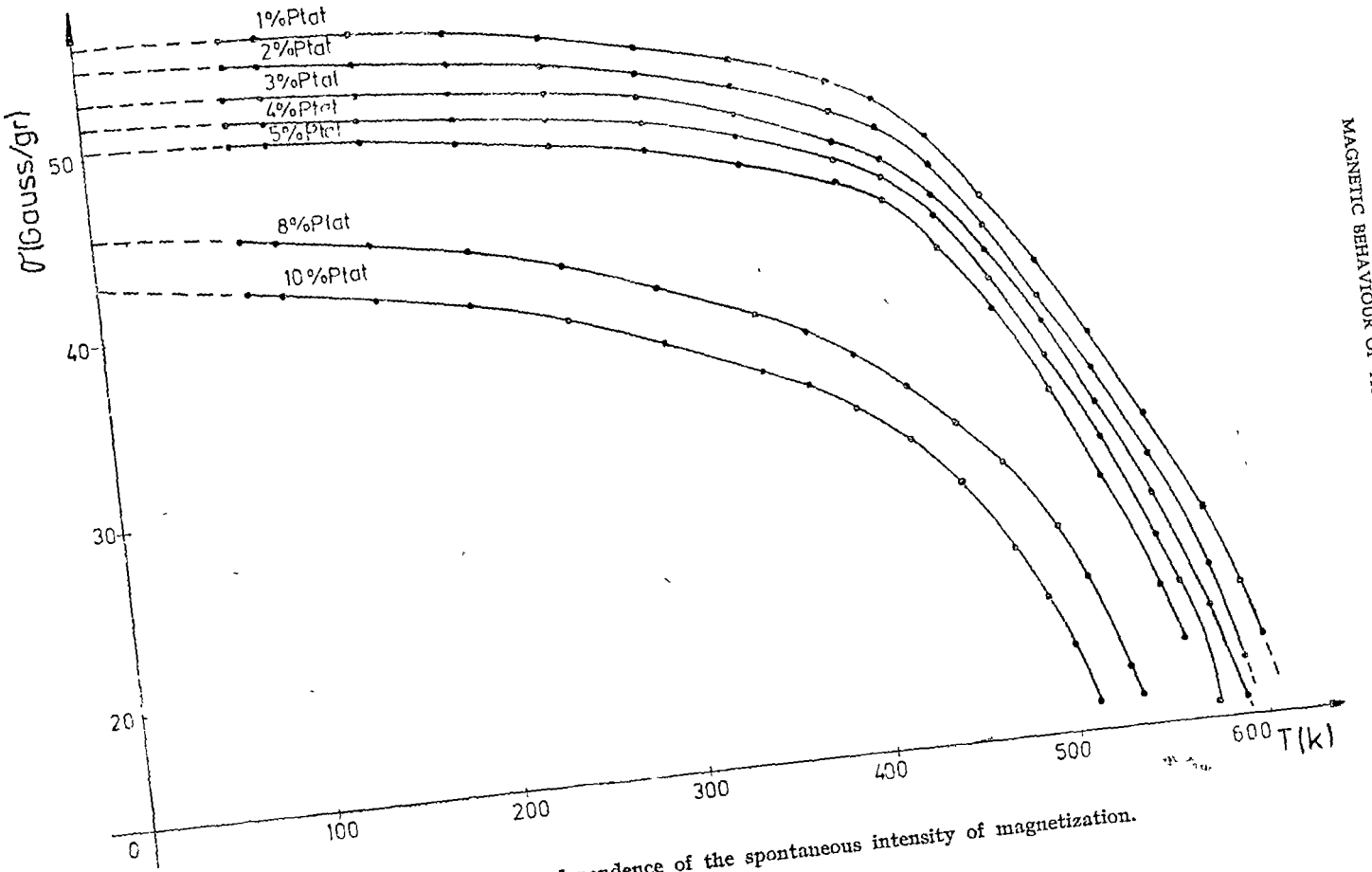

Fig. 2 The temperature dependence of the spontaneous intensity of magnetization.

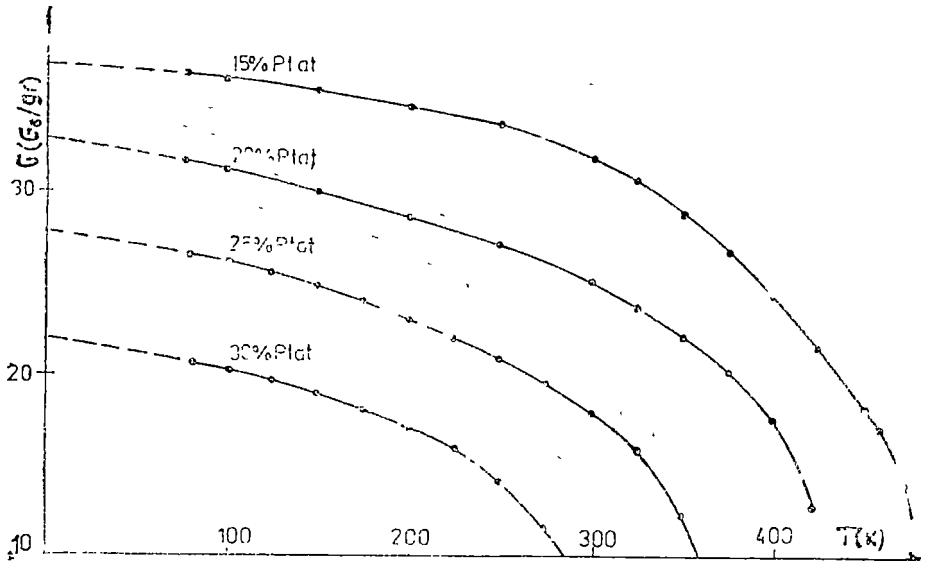

Fig 3 The temperature dependence of the spontaneous intensity of magnetization

dence is linear up to the $T \simeq 0.4\ T_c$ temperatures even for the spin wave model for the temperature dependence of spontaneous magnetization is well verified in a sufficiently broad temperature range $(0 \div 0\ 4\ T_c)$.

For the higher temperature region $(0.4\ \mathrm{Tc} \div 0.7\ T_c)$ the $\sigma = f(T^2)$ dependence is verified, as one can see in Fig. 5. In this temperature range the itinerant-electron model in the approximation of the molecular field theory is verified

The extrapolated values of the spontaneous intensity of magnetization presented in Figs. 2, 3 and 4 for $T = 0$ have the same values. From these values the moment values per alloy atom were determined. The concentration dependence of the magnetic moment per alloy atom is plotted in Fig 6, in comparison with other reported experimental results [6, 7, 8, 9] and the theoretical curve is given by continuous line [3]

One can see that the magnetic moment values decrease approximately linearly with the platinum concentration for the low concentrated alloys. This linear dependence and the slow decrease may be given by the fact that the Fermi level of the spontaneous magnetic moment is not displaced to the higher energies domain when the platinum concentrations increase. The pronounced modification of $\mu(c)$ for $c > 8\%$ at. Pt pointed out that for these concentrations the rigid-band model cannot be applied in this domain On the other hand we have to mention that this non-linear dependence can be also suggested the specific heat data [10, 11].

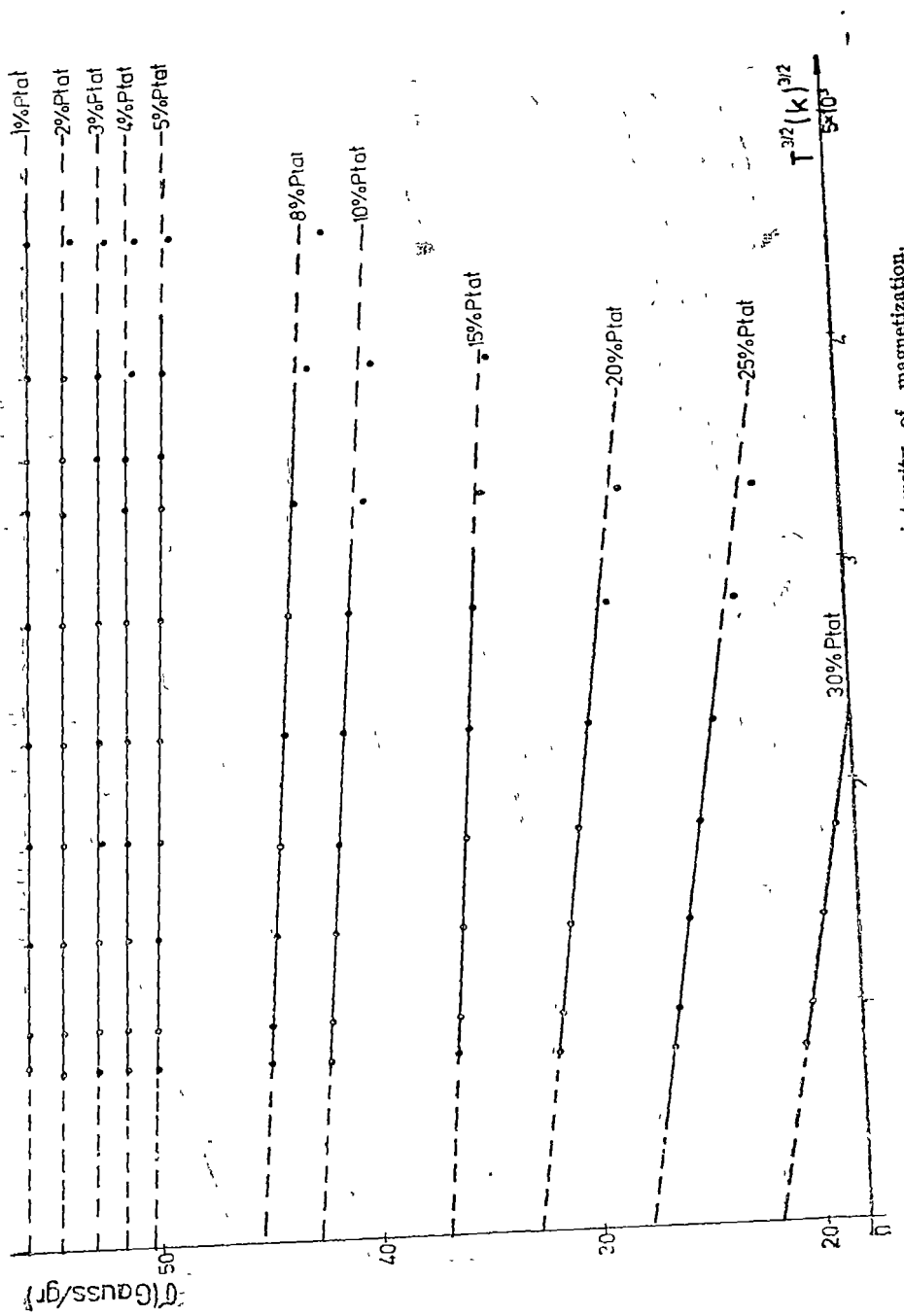

Fig. 4. $T^{3/2}$ — dependence of the spontaneous intensity of magnetization.

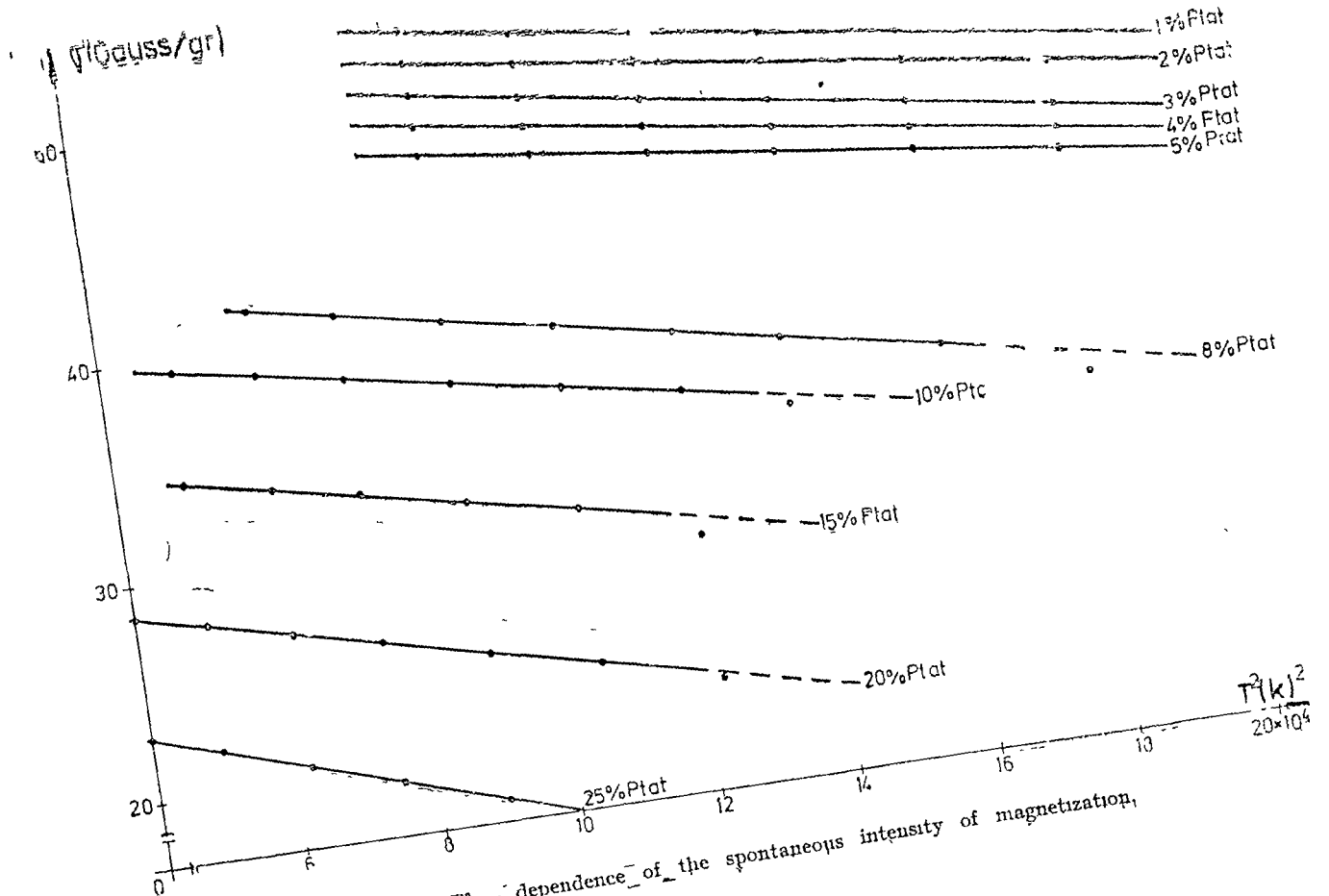

Fig 5 T^2 – dependence of the spontaneous intensity of magnetization,

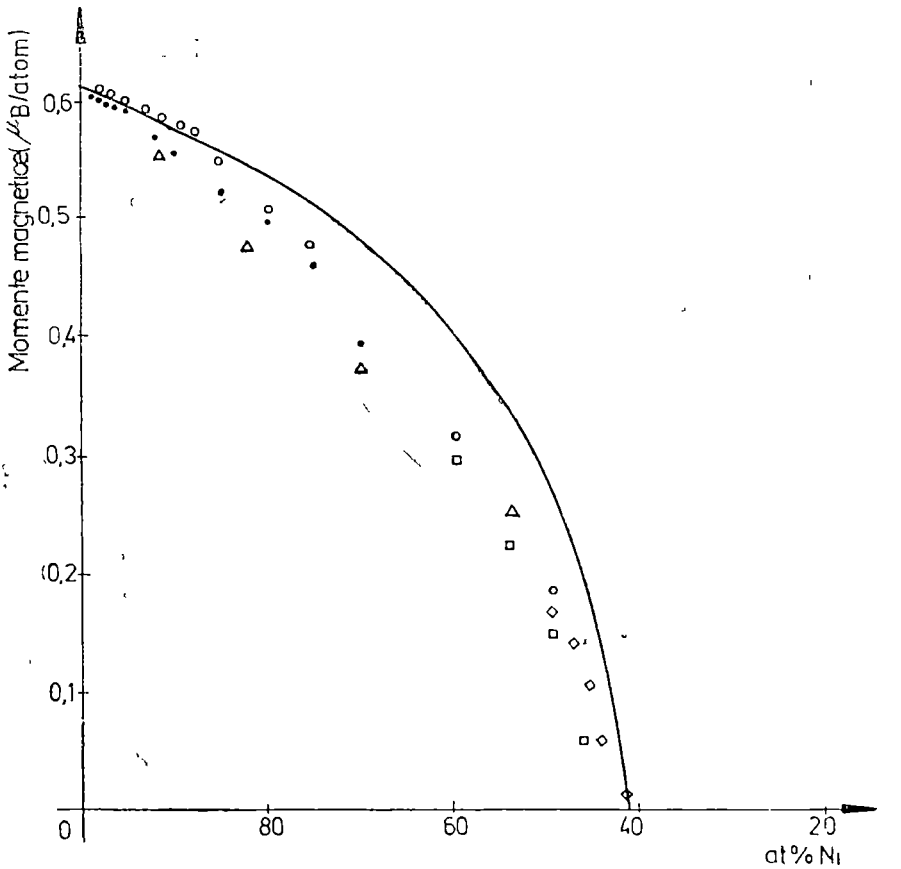

Fig 6 The concentration dependence of the magnetic moment per alloy atom. ● This study, ○ Fischer and Besnus [7], △ Marian [6], □ Besnus and Herr [8], ◇ Alberts et al [9], the continuous line is the theoretical curve (Inoue and Shimizu [3])

REFERENCES

1 R E Parra and J W Cable, *J Appl Phys*, **50**, (11), 7522 (1979)
2 R E Parra and R Medina, *Phys Rev*, *B*. **22**, (11), 5460 (1980)
3 J Inoue and M Shimizu, *J Phys Soc Japan*, **42**, 1547 (1977)
4 M Watanabe and S Miyahara, *J Phys Soc Japan*, **23**, 451 (1967)
5 F Bolling, *Phys kondens Materie*, **7**, 162 (1968)
6 V Marian, *Ann Phys*, **7**, 514 (1937)
7 G Fisher and M J Besnus, *Solid State Commun* **7**, 1527 (1969)
8 M J Besnus and A Herr, *Phys Letters*, **39A**, 83 (1972)
9 H L Alberts, J Beille, D Bloch, and E P Wohlfarth, *Phys Rev*, **B9**, 2333 (1974)
10 D J Gillespie, C A Maclıet, and A I Schindler, *Boulder conf Low Temp Phys*, 1972
11. J Beille, D Bloch, and R Kuentzler, *Solid State Commun*, **14**, 963 (1974).

STUDIA UNIV BABEŞ-BOLYAI, PHYSICA, XXXIII, 1, 1988

APPLICATION OF THE FAST FOURIER TRANSFORM ALGORITHM FOR DECONVOLUTION OF EPR IMAGING SPECTRA

AL. NICULA*, S. AŞTILEAN* and M. TODICA*

Dedicated to Professor IOAN URSU on his 60th anniversary

Received March 15, 1988

ABSTRACT. — The development and testing of a useful Fast Fourier Transform (FFT) routine on a personal computer is described The feasibility to perform the deconvolution procedure of EPR imaging spectra by Fourier methods is also examined.

1 **Introduction.** The Fast Fourier Transform (FFT) is a well-known and well-appreciated algorithm for reducing the number of calculations required to compute the Discrete Fourier Transform (DFT) compared to using a straightforward numerical evaluation. Probably, the most common application of the FFT is to produce frequency domain spectra from time domain data. For example in NMR or NMR Imaging, after a suitable sequences r f pulses, the resulting free induction decay is Fourier transformed to generate the frequency spectrum which contains structural and dynamical information [1] Also, in EPR Imaging, the analysis for the observed spectra requires the deconvolution procedure and for this purpose the Fourier transform was used in a FFT algorithm [2, 3].

In I R Spectroscopy the resulting interferogram can be digitized and Fourier transformed to yield a frequency spectrum detailing certain molecular motions. In general, one, two, and three dimensional DFT's are of wide use in several domains of pure and applied physics (optics, solid state physics, plasma physics, astrophysics, ...) and it is fair to say that the FFT is used widely in many disciplines.

Information regarding the spatial distributions of paramagnetic species is very important for studies on transport phenomena in solid and liquid films, biological systems, chemical reactions, surface diffusion etc. For these purpose EPR Imaging has been developed during the last five years [4].

Papers of previons authors have contributed to present EPR Imaging measurements and mathematical developments of the deconvolution procedure and image reconstruction [5, 6]

The aim of this paper is to present the feasibility of performing the deconvolution procedure of EPR Imaging spectra by Fourier methods Also, the particularity of derivation and implementation of a simple, but efficient FFT algorithm on an P C is presented

This feasibility is examined to allow performing an interface with EPR and NMR spectrometer.

* *University of Cluj-Napoca, Faculty of Mathematics and Physics, 3400 Cluj-Napoca, Romania*

2 **The FFT Algorithm.** The FFT algorithm devised by Cooly and Tukey (1965) greatly reduces the time required to compute the DFT. The development and theory of this technique is well documented [7, 8]. We shall therefore only discuss the FFT algorithm briefly. What is required is the evaluation of the DFT, i.e the following expression:

$$A(k) = \frac{1}{N} \sum_{n=0}^{N-1} X(n) W^{kn}, \qquad k = 0, 1, \ldots, N-1 \qquad (1)$$

where $W = exp\,(-2\pi i/N)$. The sequence appearing on the left side is usually a function of frequency and the sequence appearing on the right is usually a function of time, space, or it may also be referred to as merely "input data".

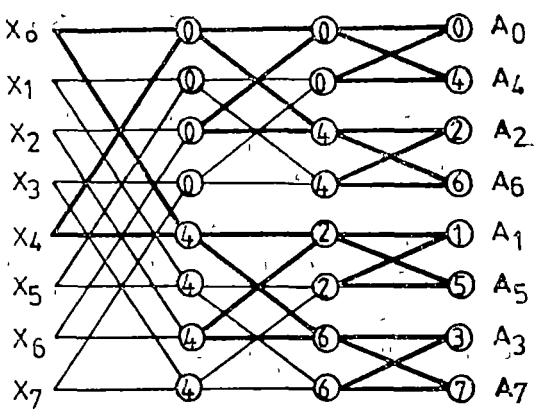

Fig 1 Signal — flow graph for a FFT of complex points

This equation can be written as a matrix equation

$$\{A_k\} = \frac{1}{N} \{W_{kn}\} \{X_n\} \qquad (2)$$

where $\{A_k\}$ and $\{X_n\}$ are column vectors containing the N frequency samples and the N time samples, respectively, $\{W_{kn}\}$ is a square matrix of order N containing the complex unit vectors, $exp(-2\pi i\, kn/N)$ It can be seen that a direct calculation of this matrix equation would require N^2 complex multiplications The saving of FFT algorithm result from a *factorization* of the matrix into a number $log_2 N$ of matrices, assuming N is a power of two.

A schematic representation of the logic flow during the FFT is most commonly illustrated under the form of a signal flow graph, which is shown in Fig 1. for the transform of 8 complex points.

In the diagram, the complex points to be transformed are displayed on the left $X_0 - X_7$, and the resulting transformed points are shown at the right as $A_0 - A_7$. It is well-known that the FFT "scrambles" the points into a modified order obtained by inverting the binary representation of the subscripts. It is necessary to rearrange the order of the final array into the more useful order of sequential subscripts.

The diagram serves as a flow-chart of the calculations and can be broken into three basic substructures *pairs, cells* and *passes* In Fig. 1., *pairs* are connected by a "butterfly" pattern of lines which symbolically represents the mathematical *operations being performed* We consider, for example, the 2 complex points X_0 and X_4 The operations performed on these 2 points are:

$$X_0' = X_0 + W^0 \quad X_4 = X_0 + [cos\,(-2\pi\emptyset/N) + i\,sin\,(-2\pi\emptyset/N)]X_4$$
$$X_4' = X_4 - W_4 \quad X_0 = X_4 - [cos\,(-2\pi 4/N) + i\,sin\,(-2\pi/N)]X_0 \qquad (3)$$

Cells consist of a variable number of pairs and are visually identified as group of overlapping "butterflies". In Fig. 1, one can find 1, 2, and 4 cells, respectively. Finally, the largest structure in Fig 1 is *the pass*. There are always $log_2 N$ passes for a transformation of N complex points, equal to the number of matrices resulting from a factorisation. In the first pass, there are $N/2$ pairs per cells and each succeeding pass contains one-half as many pairs per cell as a preceding pass

The interactive FFT subroutine has been written in BASIC language for an HC — 85 personal computer (PC). Note that it contains three FOR—NEXT loops which is the major reason for long execution times required to the transform of 256 data points Fortunately, there are various tricks which can be used to reduce the amount of work Our subroutine introduces some additional simplifications which further enhance the execution speed of FFT

3. **The correspondence between discret and integral Fourier transforms.** In the application of digital computers to Fourier methods with continuous function, one must necessarily treat a discrete set of sampled values over a finite interval of time or distance. From this, we present some features which relate the Fourier integral transform to the DFT.

Consider the integral Fourier transform of a function $x(t)$:

$$a(f) = \int_{-\infty}^{+\infty} x(t)\, exp\ (-2\pi\, ift)\, dt \tag{4}$$

and its inverse:

$$x(t) = \int_{-\infty}^{+\infty} a(f)\, exp\ (2\pi\, ift)\, df \tag{5}$$

In order to observe the effect of sampling at finite intervals, express (5) evaluated at the points $x_n = n\Delta t$, $n = 0, \pm 1, \pm 2, \ldots$, with $F \simeq 1/\Delta t$:

$$x(t_n) = \int_{-\infty}^{+\infty} a(f)\, exp\ (2\pi\, inf/F)\, dt = \sum_{K=-\infty}^{+\infty} \int_{kF}^{(k+1)F} a(f)\, exp\ (2\pi\, inf/F)\, df =$$

$$= \int_{0}^{F} \sum_{k=-\infty}^{+\infty} a(f + kF) \quad exp\ (2\pi\, inf/F) \cdot df \tag{6}$$

$$\text{where} \sum_{k=-\infty}^{+\infty} a(f + kF) \equiv a_p(f)$$

Thus, knowing $x(t)$ only as sampling points, the best one can do about obtaining $a(f)$ is to compute $a_p(f)$ The latter differs from $a(f)$ by the sum of the $a(f)$ displaced by all multiples of F This error is referred to as "aliasing"

In general, if $x(t)$ and $a(f)$ are coupled by Fourier integral transform, then

$$T \quad x_p(n\Delta t) \leftrightarrow a_p(k\Delta f), \quad n, k = 0, 1, 2, \qquad N - 1 \tag{7}$$

where $N = 1/\Delta t \quad \Delta f$

It is well-known that the Fourier transform of a product of two functions is proportional to the convolution of the individual transforms.

This effect is shown in Fig. 2 in which the Fourier transform of a sampled function is shown to repeat at intervals corresponding to the inverse of the spacing between the impulse functions The important thing to observe is Fig 2 *e* in which the function on the interval $[1/2\Delta t, 1/\Delta t]$ is *an image* of the function on the interval $[-1/2\Delta t, 0]$. For an N points transform, the first $N/2$ points are the positive frequencies and the second $N/2$ points are the negative frequencies

The Nyquist sampling theorem states that a wave-form must be sampled at a rate at least twice that of the highest frequency present in order to prevent aliasing. By this criterion, a sampling interval of Δt would suffice to sample components of frequecy $f \leqslant 1/2\,\Delta t = F/2$

An example of the use of this theorem is as follows One may select F, a maximum frequency interval, and N, a number of points The parameters, $\Delta f = F/N$, $T = 1/\Delta f$ and $\Delta t = 1/F$ are all determined.

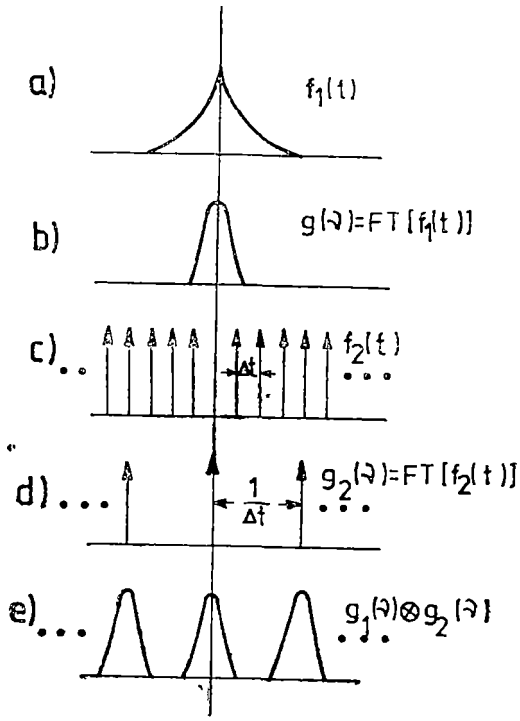

Fig 2 A schematic representation of the effect of discretely sampling of a continuous function which is Fourier transformed The Fourier transform of f_1 multiplied by f_2 is the convolution of g_1 and g_2, shown in *e*)

As an example, we present the results of the Fourier transform of the trial function.

$$x(t) = exp\,(-t) \quad \text{for } t \geqslant 0 \tag{8}$$

$$x(t) = 0 \qquad \text{for } t < 0$$

The correct results is $a(f) = 1/(1 + 2\pi i f)$ (9)

The test for our program is depicted in Fig 3 For $N = 32$ and $F = 4$ the aliasing is reduced, and a reasonable approximation to $a(f)$ is obtained over a wider range of f

4 **Fourier Transform of a real function.** Thus far we have dealt exclusively with FFT of complex data, but in EPR Imaging only input of real data is used for the transform The output, however, will always be complex, consisting of a real and an imaginary part.

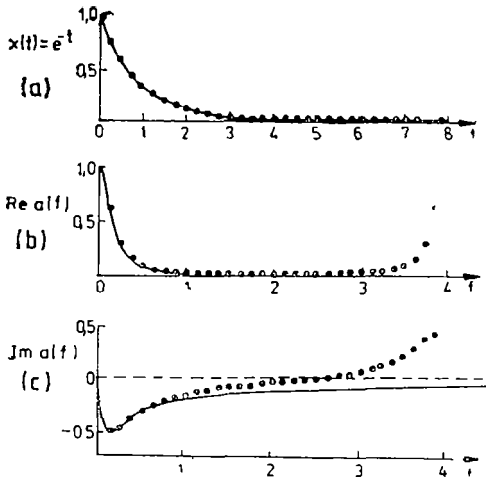

Fig 3 The calculation of the discrete Fourier transform of the trial function using T = 8, N = 32, $\Delta t = 1/4$ and F = 4 The two solide curves are the real and imaginary parts of $a(f)$ and the computed results are indicated by dots Aliasing errors in the solution are reduced

There are many alternative approaches to perform the DFT of real data .

a) The Fourier transform of two sets of real data in one pass through a DFT subrutine

Using the linearity property, we see that if $X(n)$ and $Y(n)$ are real sequences such that

$$X(n) \leftrightarrow A_x(k) + iB_x(k)$$
$$Y(n) \leftrightarrow A_y(k) + iB_y(k) \tag{10}$$

if we form $Z(n) = X(n) + iY(n)$ (11)

then $Z(n)$ has the transform

$$Z(n) \leftrightarrow A_z(k) + iB_z(k) \tag{12}$$

Replacing k by $N - k$, taking complex conjugate of both sides and applying an important property, we get .

$$A_x(k) = \frac{1}{2}\,[A_z(k) + A_z(N - k)] \tag{13}$$

$$A_y(k) = \frac{1}{2}\,[B_z(k) + B_z(N - k)] \tag{14}$$

$$B_x(k) = \frac{1}{2}\,[B_z(k) - B_z(N - k)] \tag{15}$$

$$B_y(k) = \frac{1}{2}\,[A_z(N - k) - A_z(k)] \tag{16}$$

Hence, this procedure is to

1) form $Z(n)$ as defined by (11),

2) compute $A_z(k) + i\,B_z(k)$ by means of the DFT subroutine

3) compute $A_x(k)$, $B_x(k)$, $A_y(x)$ and $B_y(k)$ according to (13—16) for $k = 0, 1, 2, \ldots, N/2$

b) Doubling algorithm-computing the Fourier transform of $2N$ points from the transform of two N-points sequences

This alternative consists in splitting the input sequence (which is assumed to contain an even number of terms) into two alternating subsequences, to be combined in one single complex sequence of one half length The DFT of this single complex sequence is then post-processed to recover the FT of the input sequence.

5. Applications of the Fourier Transform in processing of EPR and EPR Imaging spectra. Application of Fourier transform to NMR and NMR Imaging is well-established [9] In this section we will present only the use of FT in processing of EPR Imaging spectra

There are several differences between EPR and NMR Imaging EPR Imaging encounters greater spectral width because of large magnetic anizotropy, large nuclear hyperfine splitting, or short relaxation times For this and other reasons, EPR cannot take advantage of the pulse techniques used in NMR Imaging Of particular concern in EPR Imaging is the problem of hyperfine structure · it is difficult to distinguish between spectral components separated by hyperfine splittings and spattially distinct spectral components separated by magnetic field gradients For these reasons it is necessary to use the deconvolution process In addition, in the measurement under moderate magnetic gradients which do not reduce S/N ratios greatly, the observed spectra must be deconvoluted to become distributions of paramagnetic species

Then, in both cases, the analysis for the observed spectra requires the d e c o n v o l u t i o n p r o c e d u r e [2, 3]

In a previous paper [6] we have described mathematical manipulation of the deconvolution procedure. For this purpose, the Fourier transformation was used

In this paper, after derivation and implementation of an efficient FFT subroutine on a PC, we can report the first processing of EPR spectrum by deconvolution procedure

As an example, Figs. 4 (a) and (b) display a simulated Gaussian spectrum without noise of two phantoms under the homogeneous external magnetic field (response function). Figs 4 (*b*) and (*c*) show a convoluted spectrum under the magnetic field gradient and a deconvoluted spectra, respectively. The response spectrum was transformed by the FFT into frequency domain and an inverse filter function, in accordance to some other works, was determined [2, 3].

After the determination of the inverse filter function, the convoluted spectrum was deconvoluted to obtain a spin density projection function. A great effectiveness of deconvolution is achieved when the optimal inverse filter function is well adjusted. Note that this procedure introduces small fiction peaks on either side of the singlet which will interfere in the exterior region of the object (see, Fig. 4, *c*).

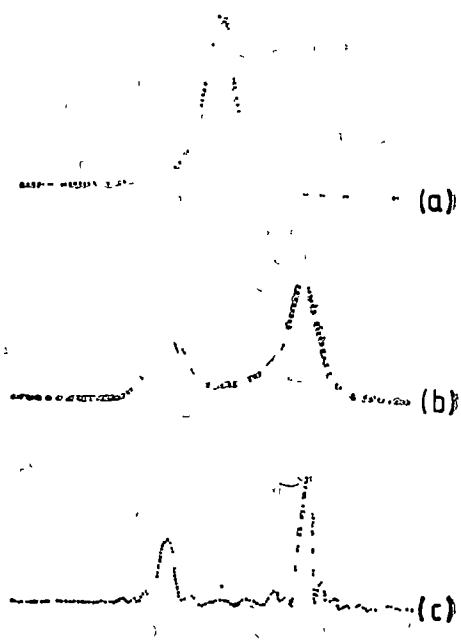

Fig 4. Deconvolution for simulated single line EPR spectrum without noise *a) response function* (Gaussian lineshape), *b) convoluted spectrum,* and *c) deconvoluted spectrum* The peak-to-peak linewidth was 8G and spatial separation was aprox. 3 mm.

The extracted spectrum or deconvoluted is defined by an integral with respect to the perpendicular axis to the direction of the magnetic field gradient. The contribution of each point toward the resonance signal is denoted by a density function $f(x, y)$, proportional to the density of paramagnetic species. If the external magnetic field gradient is applied along the coordonate axis x, the integral of $f(x, y)$ along y is called the resonance sum or resonance projection:

$$P(x) = \int f(x, y)dy \tag{17}$$

A complete set of resonance-sums is called *a projection* or profils and corresponds to a deconvoluted spectrum Finally the reconstruction process is performed with the theory of *the convolution filtering back-projection method* [10].

The resonance-sums are observed at different angles by rotating the sample within cavity.

After the filtering we have:

$$f(x, y) = \sum_{j=1}^{m} P'(x \cos \Phi_j + y \sin \Phi_j ; \Phi_j)\Delta\Phi \tag{18}$$

where m is the number of projections and $\Delta\Phi$ is the interval between projections.

6. **Conclusions.** In conclusion we remark the usefulness of the Fourier method in deconvolution procedure of the EPR Imaging spectra. In turn we have attempted the deconvolution method to single line spectrum, only to test our FFT program developed on a PC, but the method could be extended to more general hyperfine patterns

Finally, FFT subroutine is a very good choice for implementing on PC, because it is a fast and particularly simple algorithm. Also, it is clear that any FFT algorithm should take advantage of a few basic enhancements.

REFERENCES

1 T C Farrar, E D Becker, *Pulse and Fourier Transform NMR*, Acad. Press (1971)
2 K Ohno, *J Magn Reson*, **50**, 145–150 (1982)
3 H Fuji, L J Berliner, *J Magn Reson*, **68**, 377–382 (1986)
4 S S Eaton, G R Eaton, *Spectroscopy*, vol 1, No 1 (1986)
5. Al. Nicula, S Nicula, L. Giurgiu, I Ursu, *Studia Univ Babeş-Bolyai, Physica* **31** (1), 3–8 (1986).
6 Al. Nicula, S Aştilean, M Todică, *Studia Univ Babeş-Bolyai Physica*, **32** (2) (1987)
7 J. Lifermann, *Théorie et applications de la TF rapide*, Masson, 1977
8 J W Cooley, P A Lewis, P D Welch, *J Sound Vib*, **12**, 315–337 (1970).
9 P Mansfield, P G Morris, *NMR Imaging in Biomedicine*, Acad Press (1982)
10 G T. Herman, *Image Reconstruction from Projections*, Acad Press (1980).
11 N Aldea, E Indrea, G. Borodi, S Aştilean, *Studia Univ. Babeş-Bolyai, Physica* **31** (1), 58–64 (1986).

STUDIA UNIV BABEŞ-BOLYAI, PHYSICA, XXXIII, 1, 1988

L'ÉQUATION DE DISPERSION D'UN FLUIDE COMPOSÉ, EN MOUVEMENT DE ROTATION UNIFORME, EN PRÉSENCE D'UN EFFET DE CONDUCTIBILITE TERMIQUE

M. VASIU*

Dedicated to Professor IOAN URSU on his 60th anniversary

Manuscrit reçu le 26 février 1988

ABSTRACT — Relation of a Composite Fluid (in the Rayleigh—Bénard Model). The Rayleigh—Bénard model for a composite fluid has been studied to include the effect of a uniform rotation on the thermal convection The collision interaction between the particles of fluid is to be considered The purpose of this paper is to give the dispersion equation

Introduction. Nous nous proposons de déduire l'équation de dispersion d'un fluide composé, incompressible, constitué d'un composant visqueux r et d'un composant non-visqueux, s Nous considérons une couche de fluide étendue à l'infinie, en présence d'un effet des collisions entre les particules du fluide et sous l'action d'un mouvement de rotation uniforme avec une vitesse angulaire $\vec{\Omega}$ $(0, 0, \Omega)$ dirigée d'après l'axe Oz La couche de fluide est chauffée de bas en haut sous l'action de l'accélération gravitationnelle $\vec{g}$ $(0, 0, -g)$ (l'effet Rayleigh—Bénard)

Nous utilisons les résultats obtenus par S. Chandrasekhar [1], M. Vasiu [2], mais à la différence de travaux cités nous considérons un modele de fluide composé, nonionisé, en presence d'un effet des collisions entre les particules du fluide

Équations fondamentales pour l'état perturbé du fluide. Le système des équations pour l'état perturbé du fluide s'écrit de la manière suivante

$$\frac{\partial \vec{v}_r'}{\partial t} = -\frac{1}{\rho_0}\frac{\partial p'}{\partial \vec{r}} + c\nu_c(\vec{v}_s' - \vec{v}_r') + \nu\Delta v_r' - \varkappa\theta\vec{g} + 2\vec{v}_r' \times \Omega \tag{1}$$

$$\frac{\partial \vec{v}_s'}{\partial t} = -\nu_c(\vec{v}_s' - \vec{v}_r') \tag{2}$$

$$\nabla \vec{v}_r' = 0\,; \quad \nabla \vec{v}_s' = 0 \tag{3}$$

$$\frac{\partial \theta}{\partial t} - \varkappa\Delta\theta = \beta w_r', \tag{4}$$

où $\vec{v}_r'$ est la perturbation de la vitesse du composant r, p' est la perturbation de la pression hydrostatique du composant r, $\vec{v}_s'$ est la perturbation de la vitesse du composant s, α est le coefficient thermique de expansion de volume du

* *Université de Cluj Napoca, Departement de Physique, 3100 Cluj Napoca, Roumanie*

fluide, θ est la perturbation de la température, $\varkappa$ est la coefficient de conductibilité thermique, $\beta = -\left|\frac{dT}{dz}\right|$, T est la température du fluide ($T = T_0 - \beta z$, où $T_0 = T$ pour $z = 0$), ∇ est l'opérateur *nabla*, $\Delta = \nabla^2$ est l'opérateur de Laplace, $w'_r = v'_{z(r)}$, $\varepsilon = \rho_s/\rho_0$, où ρ_s est la densité du composant s, ρ_0 est la densité du composant r, ν est le coefficient de viscosité cinematique du composant r. Admettons que des petites perturbations $\varphi(x, y, z, t)$ se propagent dans le fluide sous la forme

$$\varphi'(x,,y,\ z,\ t) = \varphi^*(z) \exp\left(\imath k_x x + \imath k_y y + nt\right), \tag{5}$$

où $\varphi^*(z)$ est l'amplitude d'onde, k_x et k_y sont les composantes du vecteur d'onde $\vec{k}$, n est la pulsation (cette grandeur peut-être un nombre complexe).
En tenant compte de (5) l'équation (2) s'écrit sous la forme

$$\vec{v}'_s = \left(\frac{\nu_c}{n + \nu_c}\right) \vec{v}'_r \tag{6}$$

Introduisant les grandeurs

$$n^* = nA,$$

$$A = 1 + \frac{\varepsilon\nu_c}{n + \nu_c}, \tag{7}$$

l'équation (1) prend la forme suivante

$$n^*\vec{v}'_r = -\frac{1}{\rho_0} \nabla p' + \nu\Delta\vec{v}'_r - \alpha\theta\vec{g} + 2\vec{v}'_r \times \vec{\Omega} \tag{8}$$

Par l'application du l'opérateur „rot" sur l'équation (8), s'obtient

$$n^* \operatorname{rot} \vec{v}'_r = \nu\Delta(\operatorname{rot} \vec{v}'_r) - \alpha \operatorname{rot} (\theta\vec{g}) + 2 \operatorname{rot} (\vec{v}'_r \times \vec{\Omega}) \tag{9}$$

En tenant compte des relations

$$\begin{aligned} \operatorname{rot} (\theta\vec{g}) &= \nabla\theta \times \vec{g} + \theta \operatorname{rot} \vec{g} = \nabla\theta \times \vec{g} \\ \operatorname{rot} (\vec{v}'_r \times \vec{\Omega}) &= (\vec{\Omega} \cdot \nabla)\vec{v}'_r = \Omega \frac{\partial v_r}{\partial z}, \end{aligned} \tag{10}$$

l'equation (9) s'écrit sous la forme

$$n^* \operatorname{rot} \vec{v}'_r = \nu\Delta (\operatorname{rot} \vec{v}'_r) - \alpha\nabla\theta \times \vec{g} + 2\Omega D\vec{v}'_r \tag{11}$$

où $D = \frac{d}{dz}$. Introduisons maintenant la grandeur

$$\zeta = (\operatorname{rot} \vec{v}'_r)_z = \frac{\partial v'_r}{\partial x} - \frac{\partial u'_r}{\partial y} = ik_x v'_r - ik_y u'_r = \tag{12}$$

où v_r' et u_r' sînt les composantes du vecteur vitesse $\vec{v_r'}(u_r', v_r', w_r')$. L'équation (11), en projection sur l'axe Oz, prend la forme

$$n^*\dot{\zeta} = \nu\Delta\zeta + 2\Omega D w_r' \tag{13}$$

Par l'application du l'opérateur rot (rot) sur l'équation (8) on obtient, en projection sur l'axe Oz, la forme modifiée de l'équation (8)

$$n^*(\text{rot}\,(\text{rot}\,\vec{v_r'}))_z = \nu\Delta\,(\text{rot}\,(\text{rot}\,\vec{v_r'}))_z + 2\,(\text{rot}\,(\text{rot}\,(\vec{v_r'}\times\vec{\Omega})))_z - \\ - \alpha(\text{rot}\,(\text{rot}\,)\theta g)))_z. \tag{14}$$

Faisant les calculs on obtient

$$n^*\Delta w_r' = \nu\Delta^2 w_r' + \alpha g\left(\frac{\partial^2\theta}{\partial x^2} + \frac{\partial^2\theta}{\partial y^2}\right) - 2\Omega D\zeta, \tag{15}$$

parce que $\text{rot}\,(\text{rot}\,\vec{v_r'}) = \nabla\cdot(\nabla\cdot\vec{v_r'}) - \Delta\vec{v_r'} = -\Delta\vec{v_r'}$ et $\nabla\cdot\vec{v_r'} = 0$ et $\text{rot}\,(\text{rot}\,(\vec{v_r'}\times\vec{\Omega})))_z = \Omega D\zeta$, $(\text{rot}\,(\text{rot}\,(\theta\vec{g})))_z = \vec{g}\left(\frac{\partial^2\theta}{\partial x^2} + \frac{\partial^2\theta}{\partial y^2}\right)$. En tenant compte des perturbations (5), de l'opérateur $\Delta = D^2 - k^2$ où $D^2 = d^2/dz^2$ et $k^2 = k_x^2 + k_y^2$, les équations (4), (13) et (15) s'écrivent sous la forme

$$n - \varkappa(D^2 - k^2)\Theta(z) = \beta W(z), \tag{16}$$

$$n^* - \nu(D^2 - k^2)Z(z) = 2\Omega D W(z), \tag{17}$$

$$[n^*(D^2 - k^2) - \nu(D^2 - k^2)^2]W(z) = -\alpha g k^2\Theta(z) - 2\Omega D Z(z), \tag{18}$$

où $\varphi'(x, y, z, t) = \theta$, w, ζ et respectivement $\varphi^*(z) = \Theta(z)$, $W(z)$, $Z(z)$ sont les perturbations et respectivement lea amplitudes des perturbations.

L'équation de dispersion Introduisons maintenant les grandeurs suivantes

$$a = kd,\ \sigma^* = \frac{n^* d^2}{\nu},\ \sigma = \frac{n d^2}{\nu},\ p = \frac{\nu}{\varkappa},\ z = dz \tag{19}$$

où d est une longeur caractéristique pour le fluide (l'épaisseur de la couche du fluide). Remplacons les grandeurs (19) en (16)—(18) Nous obtiendrons ces équations sous la forme

$$(D^2 - a^2 - \sigma p)\Theta = -\left(\frac{\beta d^2}{\varkappa}\right) W \tag{20}$$

$$(D^2 - a^2 - \sigma^*)Z = -\left(\frac{2\Omega d}{\nu}\right) WD \tag{21}$$

$$(D^2 - a^2)(D^2 - a^2 - \sigma^*)W = \left(\frac{2\Omega d^3}{\nu}\right) DZ + \left(\frac{\alpha g d^2}{\nu}\right) a^2\Theta \tag{22}$$

où $D = \frac{d}{dz}$, $D^2 = \frac{d^2}{dz^2}$. Introduisant les nombres

$$R = \frac{\alpha\beta g d^4}{\nu\varkappa}, \quad T = \frac{4\Omega^2 d^4}{\nu^2}$$

où R est le nombre de Rayleigh et T est le nombre de Taylor, éliminant les fonctions Θ et Z entre les équations (20)—(22), on obtient l'équation de dispersion

$$\begin{aligned}(D^2 - a^2 - \sigma p)\{(D^2 - a^2)[(D^2 - a^2 - \sigma^*)^2] + TD^2\}W = \\ = -Ra^2(D^2 - a^2 - \sigma^*)W.\end{aligned} \tag{23}$$

Cas particulier Pour le cas d'un modèle de fluide non-composé en l'absence de l'effet des collisions : $\nu_c = 0$, $A = 1$, $n^* = n$, $\sigma^* = \sigma$, $\vec{v}_s = 0$, l'équation de dispersion (23) se réduit à la forme obtenue par Chandrasekhar. Le problème d'un modèle de fluide ionisé en présence d'un effet des collisions sera analysé dans un autre article.

BIBLIOGRAPHIE

1 S Chandrasekhar, *Hydrodynamic and Hydromagnetic Stability*, Oxford, 1961, § 29
2 M Vasiu, *Studia Univ Babeş-Bolyai, Physica*, **30**, 40 (1985)

STUDIA UNIV BABEŞ-BOLYAI, PHYSICA, XXXIII, 1, 1988

L'ÉQUATION DE DISPERSION D'UN FLUIDE COMPOSÉ, IONISÉ, EN PRÉSENCE D'UN EFFET DE CODUCTIBILITÉ THERMIQUE

M. VASIU*

Dedicated to Professor IOAN URSU on his 60 th anniversary

Manuscrit reçu le 26 février 1988

ABSTRACT. — Dispersion Relation of a Composite Plasma (in the Rayleigh—Bénard Model with Thermosolutal Effect). The purpose of this paper is to give the dispersion equation for a composite fluid The fluid consists of an ionized component and a neutral component The Rayleigh—Bénard model (thermal convection in the presence of the gravitational acceleration) has been studied to include the thermosolutal effect and the collision interaction between the particles of fluid in the presence of Hall effects

Introduction. Dans le présent article nous voulons déduire l'équation de dispersion d'un fluide composé, constitué d'un composant visqueux, ionisé, incompressible, doué d'une conductivité électrique finie, en présence de l'effet Hall (composant noté par l'indice p) et d'un composant neutre (de point de vue électrique), noté par l'indice n, sous l'action d'un champ magnétique uniforme $\vec{B}_0(0, 0, B_0)$ dirigé d'après l'axe Oz et aussi sous l'action de l'accélération gravitationnelle $\vec{g}$ $(0, 0, -g)$

Nous considérons une couche de fluide, de l'épaisseur d, étendue à l'infinie, qui est chauffée de bas en haut (admettons l'existence d'un gradient de température $\beta' = \left|\frac{dT}{dz}\right|$ et aussi d'un gradient de concentration $\beta' = \left|\frac{dC}{dz}\right|$ à l'intérieur du fluide) (modèle Rayleigh—Bénard généralisé), en présence d'un effet des collisions entre les particules du fluide

Nous utilisons les resultats obtenus par S. Chandrasekhar [1], M Vasiu [2], R. Sharma, K. Sharma [3], [4], [5], P. Gupta. K. Singh [6].

Équations fondamentales pour l'état perturbé du fluide. Pour le modèle de fluide considéré le système des équations magnétohydrodynamiques s'écrit sous la forme

$$\frac{\partial \vec{u}_p}{\partial t} = -\frac{1}{\rho}\nabla p + \varepsilon\nu_c(\vec{u}_n - \vec{u}_p) + \nu\Delta\vec{u}_p - \alpha\theta\vec{g} + \alpha'\gamma\vec{g} + \frac{1}{\mu_0\rho}(\nabla \times \vec{B}) \times \vec{B}_0 \tag{1}$$

$$\frac{\partial \vec{u}_n}{\partial t} = -\nu_c(\vec{u}_n - \vec{u}_p) \tag{2}$$

* *Université de Cluj-Napoca, Departement de Physique, 3400 Cluj-Napoca, Roumanie*

$$\frac{\partial \vec{B}}{\partial t} = \nabla \times (\vec{u} \times \vec{B}_0) + \nu_m \Delta \vec{B} - \mathcal{K} \nabla \times [(\nabla \times \vec{B}) \times \vec{B}_0] \tag{3}$$

$$\frac{\partial \theta}{\partial t} = \varkappa \Delta \theta + \beta w \tag{4}$$

$$\frac{\partial \gamma}{\partial t} = \varkappa' \Delta \gamma + \beta' w \tag{5}$$

$$\nabla \quad \vec{u}_p = 0, \ \nabla \quad \vec{u}_n = 0 \tag{6}$$

où $\vec{u}_p$ est la perturbation de la vitesse du composant p, $\vec{u}_n$ est la perturbation de la vitesse du composant n, ρ est la densité du composant p, $\varepsilon = \rho_n/\rho$, où ρ_n est la densité du composant n, α est le coefficient thermique de expansion de volume, α' est le coefficient solvant de expansion de volume, $\varkappa$ est le coefficient de conductibilité thermique, $\varkappa'$ est le coefficient de diffussion de dissolution, ν_m est le coefficient de diffusion magnétique, p est la perturbation de la pression du composant p du fluide, $\vec{B}$ est la perturbation du champ magnétique, θ est la perturbation de la température, γ est la perturbation de la concentration, ∇ est l'opérateur nabla, Δ est l'opérateur de Laplace, w est la perturbation du composant $u_{z(p)}$ de la vitesse $\vec{u}_p$, $\mathcal{K} = 1/Nc\mu_0$, $1/Ne$ est la constante de Hall

Admettons que des petites perturbations se propagent dans le fluide sous la forme

$$\varphi(x, y, z) = \varphi(z) \exp (\imath k_x x + \imath k_y y + nt) \tag{7}$$

où $\varphi = u, B_z, \theta, p, \gamma$, $\varphi(z)$ est l'amplitude d'onde, k_x, k_y sont les composantes du vecteur d'onde, n est la pulsation d'onde

En introduisant [2] la grandeur $n^* = nA$, où $A = 1 + \frac{\varepsilon \nu_c}{n + \nu_c}$, l'équation (1) prend la forme

$$(n^* - \nu\Delta)\vec{u} = -\frac{1}{\rho}\nabla p - \alpha\theta\vec{g} + \alpha'\gamma\vec{g} + \frac{1}{\mu_0\rho}(\nabla \times \vec{B}) \times \vec{B}_0 \tag{8}$$

Pour simplifier la notation nous omettons l'indice p

Par l'application du l'opérateur *rot* sur l'équation (8), en tenant compte des relations vectorielles

$$\begin{gathered} \operatorname{rot}(\theta\alpha\vec{g}) = \nabla \times (\theta\alpha\vec{g}) = \alpha\nabla\theta \times \vec{g}, \quad \operatorname{rot}(\alpha'\gamma\vec{g}) = \nabla \times (\gamma\alpha'\vec{g}) = \\ = \alpha'\nabla\gamma \times \vec{g} \\ \operatorname{rot}[(\operatorname{rot}\vec{B}) \times \vec{B}_0] = \nabla \times [(\nabla \times \vec{B}) \times \vec{B}_0] = (\vec{B}_0 \quad \nabla)(\nabla \times \vec{B}) \end{gathered} \tag{9}$$

où $\nabla \times [\nabla(\vec{B}_0 \quad \vec{B})] = 0$, l'équation (8) prend la forme

$$(n^* - \nu\Delta)(\nabla \times \vec{u}) = -\alpha\nabla\theta \times \vec{g} + \alpha'\nabla\gamma \times \vec{g} + \frac{1}{\mu_0\rho}(\vec{B}_0 \cdot \nabla)(\nabla \times \vec{B}) \tag{10}$$

En projection sur l'axe Oz les equations (3) et (10), s'écrivent

$$(n - \nu_m\Delta)B_z = B_0Dw - \mathcal{R}B_0D(\nabla \times \vec{B})_z \tag{11}$$

et

$$(n^* - \nu\Delta)(\nabla \times \vec{u})_z = \frac{1}{\mu_0\rho} B_0D(\nabla \times \vec{B})_z, \tag{12}$$

où $D = \frac{d}{dz}$. Introduisons maintenant les grandeurs

$$\zeta = (\nabla \times \vec{u})_z, \quad \xi = (\nabla \times \vec{B})_z. \tag{13}$$

Les équations (11) et (12) prendent la forme

$$(n - \nu_m\Delta)B_z = B_0Dw - \mathcal{R}B_0D\xi \tag{14}$$

et

$$(n^* - \nu\Delta)\zeta = \frac{B_0}{\mu_0\rho} D\xi. \tag{15}$$

L'application du l'opérateur *rot* (*rot*) sur l'équation (8), écrite en projection sur l'axe Oz, nous conduit à la forme

$$(n^* - \nu\Delta)(\text{rot (rot } \vec{u}))_z = -\alpha(\text{rot (rot } (\theta\vec{g})))_z + \alpha'(\text{rot (rot } (\gamma\vec{g})))_z + \frac{B_0}{\mu_0\rho} D(\text{rot (rot } \vec{B}))_z. \tag{16}$$

En tenant compte des relations vectorielles

$$\text{rot (rot } \vec{u})) = \nabla \times (\nabla \times \vec{u}) = \text{grad (div } \vec{u}) - \Delta\vec{u} = \nabla(\nabla \cdot \vec{u}) - \Delta\vec{u} = -\Delta\vec{u}, \tag{17}$$

$$(\text{rot (rot } (\theta\vec{g})))_z = (\text{rot } (\nabla\theta \times \vec{g}))_z = g\left(\frac{\partial^2\theta}{\partial x^2} + \frac{\partial^2\theta}{\partial y^2}\right),$$

$$(\text{rot (rot } (\gamma\vec{g})))_z = (\text{rot } (\nabla\gamma \times \vec{g}))_z = g\left(\frac{\partial^2\gamma}{\partial x^2} + \frac{\partial^2\gamma}{\partial y^2}\right),$$

$$\text{rot (rot } \vec{B})) = \nabla \times (\nabla \times \vec{B}) = \text{grad (div } \vec{B}) - \Delta\vec{B} = -\Delta\vec{B},$$

l'équation (16) s'écrit de la manière suivante

$$(n^*\Delta - \nu\Delta^2)w = \alpha g\left(\frac{\partial^2\theta}{\partial x^2} + \frac{\partial^2\theta}{\partial y^2}\right) - \alpha' g\left(\frac{\partial^2\gamma}{\partial x^2} + \frac{\partial^2\gamma}{\partial y^2}\right) + \frac{B_0}{\mu_0\rho} D(\Delta B_z). \tag{18}$$

Par l'application du l'opérateur rot sur l'équation (3), écrite en projection sur l'axe Oz, on obtient

$$(n - \nu_m\Delta)\xi = B_0D\zeta + \mathcal{R}B_0D(\Delta B_z) \tag{19}$$

En tenant compte de la forme (7) des perturbations, de l'opérateur $\Delta =$

$= D^2 - k^2$, où $D^2 = \frac{d^2}{dz^2}$, $k^2 = k_x^2 + k_y^2$, le système des équations (4), (5), (14), (15), (18) et (19) s'écrit sous la forme

$$(n - \varkappa(D^2 - k^2))\Theta = \beta W, \tag{20}$$

$$(n - \varkappa'(D^2 - k^2))\Gamma = \beta' W, \tag{21}$$

$$(n - \nu_m(D^2 - k^2))K = B_0 DW - \mathfrak{M} B_0 DX, \tag{21}$$

$$(n^* - \nu(D^2 - k^2))Z = \frac{B_0}{\mu_0 \rho} DX, \tag{22}$$

$$(n^* - \nu(D^2 - k^2))(D^2 - k^2)W = -\alpha g k^2 \Theta + \alpha' g k^2 \Gamma + \frac{B_0}{\mu_0 \rho} D(D^2 - k^2)K, \tag{23}$$

$$(n - \nu_m(D^2 - k^2))X = B_0 DZ + \mathfrak{M} B_0 D(D^2 - k^2)K, \tag{24}$$

où Θ, Γ, K, W, X et Z sont les amplitudes — considérées comme fonctions de z — des perturbations 0, γ, B_z, w, ξ, ζ respectivement Introduisons les grandeurs

$$a = kd, \quad z = dz, \quad \sigma = \frac{nd^2}{\nu}, \quad \sigma^* = \frac{n^* d^2}{\nu}, \quad p_1 = \frac{\nu}{\varkappa}, \tag{25}$$

$$p_2 = \frac{\nu}{\nu_m}, \quad p_3 = \frac{\nu}{\varkappa'},$$

où d est une longueur caractéristique du domaine occupé par le fluide. Remplaçons les grandeurs (25) en équations (20)—(24) Le système des équations (20)—(24) s'écrit de la manière suivante

$$(D^2 - a^2 - p_1\sigma)\Theta = -\left(\frac{\beta d^2}{\varkappa}\right) W, \tag{26}$$

$$(D^2 - a^2 - p_3\sigma)\Gamma = -\left(\frac{\beta' d^2}{\varkappa'}\right) W, \tag{27}$$

$$(D^2 - v^2 - p_2\sigma)K = -\left(\frac{B_0 d}{\nu_m}\right) DW + \left(\frac{\mathfrak{M} B_0 d}{\nu_m}\right) DX, \tag{28}$$

$$(D^2 - a^2 - \sigma^*)Z = -\left(\frac{B_0 d}{\mu_0 \rho \nu}\right) DX, \tag{29}$$

$$(D^2 - a^2)(D^2 - a^2 - \sigma^*)W = \left(\frac{\alpha g d^2}{\nu}\right) a^2 \Theta - \left(\frac{\alpha' g d^2}{\nu}\right) a^2 \Gamma - \tag{30}$$

$$- \left(\frac{B_0 d}{\mu_0 \rho \nu}\right)(D^2 - a^2) DK,$$

$$(D^2 - a^2 - p_2\sigma)X = -\left(\frac{B_0 d}{\nu}\right) DZ - \left(\frac{\mathfrak{M} B_0}{d \nu_m}\right)(D^2 - a^2) DK. \tag{31}$$

Introduisons maintenant les constantes

$$c_0 = \frac{\beta d^2}{\varkappa},\ c_1 = \frac{\beta' d^2}{\varkappa'},\ c_2 = \frac{B_0 d}{\mu_0 \rho \nu},\ c_3 = \frac{\alpha g d^2}{\nu} a^2,\ c_4 = \frac{\alpha' g d^2}{\nu} a^2,\ c_5 = \frac{B_0 d}{\nu_m},$$

$$c_6 = \frac{\varkappa B_0 d}{\nu_m},\ c_7 = \frac{\varkappa B_0}{d\nu_m} \tag{32}$$

et les opérateurs

$$O = D^2 - a^2,\ O_1 = D^2 - a^2 - p_1\sigma,\ O_2 = D^2 - a^2 - p_2\sigma,$$
$$O_3 = D^2 - a^2 - p_3\sigma,\ O^* = D^2 - a^2 - \sigma^* \tag{33}$$

Par conséquent le système des équations (26)—(31) prend la forme

$$O_1\Theta = -c_0 W, \tag{34}$$
$$O_3\Gamma = -c_1 W, \tag{35}$$
$$O_2 K = -c_5 DW + c_6 DX, \tag{36}$$
$$O^* Z = -c_2 DX, \tag{37}$$
$$OO^* W = c_3\Theta - c_4\Gamma - c_2 ODK, \tag{38}$$
$$O_2 X = -c_5 DZ - c_7 ODK. \tag{39}$$

L'équation de dispersion. Finalement on obtient l'équation de dispersion. Éliminant la fonction Z entre les équations (37) et (39) par l'application de l'opérateur $-c_5 D$ dans (37) et du l'opérateur O^* dans (39) il en résulte

$$DX = -\frac{c_7 O^* OD^2 K}{O^* O^2 - c_2 c_5 D^2}. \tag{40}$$

La substitution de la relation (40) dans l'équation (36) nous conduit à la forme

$$LK = -c_5 L_1 DW, \tag{41}$$

où les opérateurs L et L_1 ont la forme

$$L = (O^* O_2 - QD^2)O_2 + MO^* OD^2;\ L_1 = O^* O_2 - QD^2, \tag{41}$$

où $M = c_6 c_7$, $Q = c_2 c_5$. Appliquant l'opérateur $O_1 O_3 L$ dans l'équation (38), en tenant compte de (41), éliminant les fonctions K, Θ, Γ, on obtient l'équation de dispersion

$$O_1 O_3 (LOO^* - QD^2 OL_1)W = -(Ra^2 LO_3 - Sa^2 LO_1)W, \tag{42}$$

où $R = \frac{g\alpha\beta d^4}{\varkappa\nu}$ est le nombre de Rayleigh, $S = \frac{g\alpha'\beta' d^4}{\varkappa'\nu}$, $Q = \frac{B_0^2 d^2}{\mu_0 \rho \nu \nu_m}$ est le nombre de Chandrasekhar.

Remplaçons les grandeurs (32) et les opérateurs (33) dans l'équation (42) nous obtiendrons la forme finale de l'équation de dispersion

$$\begin{aligned}&(D^2-a^2-p_3\sigma)(D^2-a^2-p_1\sigma)\{[[(D^2-a^2-\sigma^*)(D^2-a^2-p_2\sigma)-\\&-QD^2](D^2-a^2-p_2\sigma)+M(D^2-a^2)(D^2-a^2-\sigma^*)D^2](D^2-a^2)(D^2-\\&-a^2-\sigma^*)-QD^2(D^2-a^2)[(D^2-a^2-\sigma^*)(D^2-a^2-p_2\sigma)-QD^2]\}W=\\&=\{[(D^2-a^2-\sigma^*)(D^2-a^2-p_2\sigma)-QD^2](D^2-a^2-p_2\sigma)+M(D^2-\\&-a^2)(D^2-a^2-\sigma^*)D^2][-Ra^2(D^2-a^2-p_3\sigma)+Sa^2(D^2-a^2-p_1\sigma\}W.\end{aligned}\tag{43}$$

Cas particuliers. Pour le cas d'un modèle de fluide ionisé, non-composé ($\nu_e=0$, $\sigma^*=\sigma$), en l'absence du l'effet Hall ($\mathcal{H}=0$, $M=0$) et aussi en l'absence du l'effet de „finite Larmor radius" et du mouvement de rotation on obtient l'équation de dispersion établie par P. Gupta, K. Singh [6].

$$\begin{aligned}&[(D^2-a^2-\sigma)(D^2-a^2-p_2\sigma)-QD^2][(D^2-a^2-p_1\sigma)(D^2-a^2-\\&-p_2\sigma)(D^2-a^2-p_3\sigma)(D^2-a^2)(D^2-a^2-\sigma)-QD^2(D^2-a^2)(D^2-\\&-a^2-p_1\sigma)(D^2-a^2-p_3\sigma)+a^2(D^2-a^2-p_2\sigma)\{R(D^2-a^2-p_3\sigma)-\\&-S(D^2-a^2-p_1\sigma)\}]W=0\end{aligned}$$

Pour le cas d'un modèle de fluide ionisé, composé, en l'absence du l'effet d'un gradient de concentration ($\beta'=0$, $S=0$) et du mouvement de rotation on obtient l'équation de dispersion établie par R. Sharma, K. Sharma [3]:

$$\begin{aligned}&\{(D^2-a^2)(D^2-a^2-\sigma^*)(D^2-a^2-p_1\sigma)+Ra^2\}\{(D^2-a^2-p_2\sigma)^2(D^2-\\&-a^2-\sigma^*)-QD^2(D^2-a^2-p_2\sigma)+MD^2(D^2-a^2)(D^2-a^2-\sigma^*)\}W=\\&=QD^2(D^2-a^2)(D^2-a^2-p_1\sigma)[(D^2-a^2-\sigma^*)(D^2-a^2-p_2\sigma)-QD^2]W.\end{aligned}$$

Pour le cas d'un modèle de fluide ionisé, non-composé, en l'absence du mouvement de rotation on obtient l'équation de dispersion établie par R. Sharma, K. Sharma [4] (cette équation a la même forme comme l'équation (43) où $\sigma^*=\sigma$, $n^*=n$, $A=1$).

Pour le cas d'un modèle de fluide non-ionisé ($Q=0$, $M=0$, $p_1=p$, $p_2=p_3=0$), composé, en l'absence du l'effet d'un gradient de concentration ($\beta'=0$, $S=0$) et du mouvement de rotation (la vitesse angulaire $\Omega=0$) l'équation de dispersion (43) se réduit à la forme obtenue par nous [2]:

$$(D^2-a^2-p\sigma)(D^2-a^2-\sigma^*)(D^2-a^2)W=-Ra^2W.$$

En l'absence de l'effet des collisions entre les particules du fluide (fluide non-composé) ($\nu_e=0$, $A=1$, $n^*=n$, $\sigma^*=\sigma$) l'équation de dispersion se réduit à la forme obtenue par S. Chandrasekhar [1].

$$(D^2-a^2)(D^2-a^2-p\sigma)(D^2-a^2-\sigma)\,W=-Ra^2W.$$

BIBLIOGRAPHIE

1 S Chandraşekhar, *Hydrodynamic and Hydromagnetic Stability*, Oxford, 1961, Chap II Chap. IV
2 M Vasiu, *Studia, Univ Babeş-Bolyai, Phys*, **33** (1), 17 (1988)
3 R Sharma, K Sharma, *Austr J Phys*, **31** (2), 181 (1978)
4 R Sharma, K Sharma, *Austr J Phys*, **35** (2), 125 (1982)
5 R Sharma, K Sharma, *Phys Fluids*, **24**, 2242 (1981)
6 P Gupta, K Singh, *Contrib Plasma Phys*, **26** (5), 353 (1986)

STUDIA UNIV BABEŞ-BOLYAI, PHYSICA, XXXIII, 1, 1988

INVESTIGATIONS CONCERNING THE NONCONVENTIONAL SEPARATION AND PURIFICATION OF HELIUM FROM GASEOUS MIXTURES

I. MASTAN*, A. TODEREAN*, C. COSMA*, O. COZAR* and V. ZNAMIROVSCHI*

Dedicated to Professor IOAN URSU on his 60th anniversary

Received February 12, 1988

ABSTRACT. — Transport phenomena through membranes which take part in nonconventional (noncryogenic) separation and purification of helium from gaseous mixtures are presented in the first part of the paper A brief mathematical description of the diffusive transport of substance through a tubular-cylindrical nonporous membrane is given The second part of the paper is mainly assigned to the description of the experimental installation for helium separation and purification through diffusion and/or activated diffusion in capillary membranes, which was performed in our laboratory The obtained experimental results and possibilities for high purification of helium are discussed Finally, a discussion is approached on the possibilities of large scale applications of nonconventional methods for helium separation and purification from gaseous mixtures and their competitivity with cryogenic ones

1 **Introduction.** Helium is a noble gas with implications of great importance in the modern fields of scientific research and technological developments [1—3].

The conventional method for helium recovery and purification from natural gases with high concentrations, of economic importance, is the cryogenic one.

In the late decades, simultaneously with the development of membranology, the possibility and opportunity of noncryogenic recovery and purification of helium from gas-mixtures has been studied [4—21] Noncryogenic separation and purification of helium involves, in all cases, the use of membranes. According to the widest acceptation, a membrane is a discontinuity region interposed between two phases [16] The elementary process of noncryogenic helium separation and purification is the diffusion through such a ,,discontinuity'' region An ideal membrane should meet two essential qualities great selectivity and high permeation rate But, in fact, these requirements are contradictory Therefore, the choice of the most suitable membrane is decisive for an efficient separation-purification method From the point of view of their structure, the membranes can be porous or nonporous, while after their mode of action they can be adsorptive, diffusive, ion-exchanging etc In all cases membranes can be made up as films, sheets, capillary tubes or hollow fibres

2. **Possibilities offered by nonconventional methods.** From the transport phenomena through membranes the following could be taken into account for noncryogenic separation (recovery) and purification of helium

* *University of Cluj Napoca, Faculty of Mathematics and Physics, 3400 Cluj-Napoca, Romania*

(2 1) Diffusion through nonporous membranes; and
(2 2) Free molecular diffusion (Knudsen flow) through porous membranes.

2 1. *Diffusion through nonporous membranes.* Diffusion is a universal phenomenon, consisting in a substance transfer under the individual or simultaneous action of concentration, pressure and temperature gradients. The most general mathematical description of the diffusion process is given by Fick's laws

$$\vec{J_j} = D_j \cdot \nabla C_j \tag{1}$$

$$-\nabla(Dj \cdot \nabla Cj) + \frac{\partial C_j}{\partial t} = 0 \tag{2}$$

where J_j is the permeate current density of component j, C_j is the concentration of component j in the working phase; and D_j is the diffusivity. The permeability P_j, diffusivity D_j, and solubility S_j, of a given component j, are in the following relation to each other: $P_j = D_j \quad S_j$

Inorganic nonporous membranes have the following features (a) relatively small permeation rate (small substance transfer flow); (b) high, even very high, selectivity, (c) operation at high pressures and temperatures. It seems that these membranes could be suitable for the high purification of helium

Organic nonporous membranes (*polymers*) offer (a) greater permeation rates, (b) smaller selectivities, (c) operation at smaller pressures even at temperatures close to the ambient one A careful choice of structure and shape (capillaries, hollow fibres) of such membranes, could make them very suitable for helium recovery and purification from natural gas-mixtures However, for higher values of helium purity it is necessary to use 2—3 separation-purification stages in cascade.

2 2 *Free molecular diffusion.* In order to obtain separation through microporous membranes the following conditions must be met (1) The pore diameter must be much smaller than the mean free path of the diffusing components; (2) The temperature must be high enough to avoid appreciable surface flow, (3) Trans-membrane pressure must be low enough, so that the mean free path should not be reduced below the limit imposed by condition (1) Thus for helium separation from natural gases, at a transmembrane pressure of 1 atm and an operating temperature of 20 °C, microporous membranes having pore diameter between 5 Å and 300 Å are required For two molecular components, of masses M_1 and M_2, the ideal separation factor is $\alpha^* = (M_2/M_1)^{1/2}$ The main advantage and disadvantage of the separation by free molecular diffusion might respectively be the relatively great flows and the small separation factors, involving the necessity of cascades if reasonable purities are wanted. So far, large scale application cases of free molecular diffusion, through microporous membranes, for helium separation from natural gases are not yet known

3 **Substance transport through solid nonporous membranes.** It is conventionally considered that the membranes having pore diameter between 5—10 Å are nonporous

3 1 *Processes involved in substance transport* Qualitatively, the transport stages of a substance, through a solid nonporous membrane, are. (1) Superfi-

cial adsorption, followed by absorption, i e. by the penetration of the gas molecules from the high pressure side, in the membrane; (2) Selective diffusion through the interstitial „empty" places, or through place-changes to the small pressure side of the membrane, this step being, in fact, decisive for the separation process; (3) Desorption from the membrane, at the small pressure side.

3 2. *Necessity of capillary membranes.* To judge the efficiency, and thus the competitivity, of nonconventional helium recovery-purification methods, as compared to the conventional ones, the separation factor (selectivity) and the substance amount, transported through the membrane, for comparable energetic and initial investments cost, must be discussed The substance quantity, in our case of helium, transported through solid nonporous membranes is directly proportional to the membrane surface and the applied trans-membrane pressure. Capillary membranes offer the possibility of using very high transmembrane pressure (more than 100 bar) increasing, at the same time, to a great extent, the permeation area.

3 3 *Substance transport equations in the case of tubular — cylindrical membrane.* For simplification we consider the unidimensional case of a substance transport by diffusion only along the direction r of the radius of the tubular-cylindrical membrane. In fact this is the direction of the pressure gradient. In this particular case, using cylindrical coordinates, Fick's equations become:

$$J_{js} = -D_j \frac{\partial C_j}{\partial r} \tag{3}$$

$$\frac{\partial C_j}{\partial t} = D_j \left(\frac{\partial^2 C_j}{\partial r^2} + \frac{1}{r} \frac{\partial C_j}{\partial r} \right) \tag{4}$$

where r_1, r_2 are the external and internal radius of the membrane, C_{j1}, C_{j2} are the concentrations of component j at the outer, inner walls of the membrane, respectively.

Stationary state. This physical fact is described mathematically by $(\partial C_j/\partial t) = 0$. The following notations are made: $J_{sj} = \dot{n}_{sj}/A$, where J_{sj} [mol/m^2 s] is the density of the stationary current of the substance quantity (j — component) which will be transported through the tubular-cylindircal membrane, A is that membrane area which is crossed vertically by the current of substance quantity transported. Solving differential equations (3) and (4) for the stationary case one can obtain:

$$J_{sj} = D_j S_j \frac{p_{j1} - p_{j2}}{\ln (r_1/r_2)} \cdot \frac{1}{r} = P_j \frac{p_{j1} - p_{j2}}{\ln (r_1/r_2)} \cdot \frac{1}{r} \tag{5}$$

where p_{j1}, p_{j2} are the partial pressures of the component j at the external and the internal walls of the tubular membrane, respectively

Nonstationary state In order to determine the diffusivity, D_j, and the permeability, P_j, it is necessary to know the nonstationary current, $\dot{n}_{js}$, and the stationary current, $\dot{n}_{sj}$, of the substance quantity of component j, through the considered membrane Paper [15] presents the solutions of the diffusion equations obtained by some authors We have taken into account the solution given in paper [22], taken as a convergent series, for long periods of time, for

which the Fourier numbers F_0^* fulfil the condition $F_0^* = (D_j t/l^2) > 0.03$ The initial and limiting conditions are chosen to give a solution as simple as possible, but at the same time, with not too rough approximations, namely $C_j = 0$ for $t = 0$ and $r_2 < r < r_1$, $C_j = 0$ for $t > 0$ and $r = r_2$, $C_j = C_{j1}$ for $t < 0$ and $r = r_1$. We are considering also that our cylinder is "empty", with very thin walls related to the diameter and to its length, that means $(L/r) \to \infty$. Under these conditions, the solution of equation (4) for $r = r_2$, i.e. at the internal wall of the tubular membrane, will be.

$$J_{jg} = -D_j \left(\frac{\partial C_j}{\partial r}\right)_{r=r_2} = -\frac{D_j C_{j1}}{r_2} \times$$

$$\times \left[\frac{1}{\ln (r_1/r_2)} + 2 \sum_{m=1}^{\infty} \frac{I_0(r_1\alpha_m)\ \ I_0(r_2\alpha_m)}{I_0^2(r_2\alpha_m) - I_0^2(r_1\alpha_m)} \cdot \exp\{-\alpha_m^2 D_j t\}\right] \qquad (6)$$

where J_{jg} is the density of the nonstationary current of the substance quantity of component j at $r = r_2$, $I_0(r\alpha_m)$ is the zero order Bessel function of type 1, in which α_m is the positive root of the eigenvalue equation. The eigenvalue equation is of the form.

$$I_0(r_2\alpha_m)\ \ Y_0(r_1\alpha_m) - I_0(r_1\alpha_m)\ \ Y_0(r_2\alpha_m) = 0$$

$Y_0(r\alpha_m)$ being the zero order Bessel function of type 2.

We simplify by noting $(r_1/r_2) = k$, $r_1 - r_2(k-1) = l$. For $1 < k < 1.5$, i e for empty cylinders with very thin walls, the Bessel functions can be developed into polynomial series [23] Thus, one can obtain for the nonstationary current density of the substance quantity of component j, J_{jg}, which is permeate in the inside of the cylindrical membrane $(r = r_2)$, the following simplified expression

$$J_{jg} = \frac{D_j C_{j1}}{l}\ \ \frac{(k-1)}{\ln k} \cdot \left[1 + 2 \sum_{m=1}^{\infty} (-1)^m\ \ \exp\left\{-\frac{m^2\pi^2}{l^2} \cdot D_j t\right\}\right] \qquad (7)$$

Solution (7) is satisfactorily rapidly converging for $F_0^* = (D_j t/l^2) > 0\ 03$, so that only a few terms of the series are necessary depending on the accuracy initially imposed.

4. Experimental installation for helium separation and purification through diffusion and/or activated diffusion in capillary membranes. Our team from the Faculty of Mathematics and Physics, Cluj-Napoca University, has accomplished and tested a laboratory installation for noncryogenic helium separation from gazeous mixtures With this installation investigations are made concerning the separation and/or high purification of helium by diffusion and/or activated diffusion through capillary membranes [24—30]

4 1 *Functional conception and systemic structure of the installation* The experimental installation was elaborated and accomplished for research purpose It covers two major functional requirements

(A) Systematic investigation of transport phenomena parameters and their dependence on temperature and pressure for helium-capillary nonporous membrane systems, the membranes being anorganic and/or organic (polymeric) ones, in order to choose the most efficient membranes for helium recovery and purification from natural gases

(B) Technological investigation, at laboratory scale, of the possibilities and efficiency of noncryogenic helium recovery-purification methods from natural gas-mixtures, in view of future semi-arge or even large scale application

To the choice of project parameters were correlated the material possibilities and the optimization of functional requirements.

From a functional point of view the installation was conceived to ensure

(1) Simultaneous operation with 1—19 capillary membrane fascicles, each fascicle being made up of 200—300 membranes, according to the geometric parameters of the capillaries.

(2) Exposure of the capillary membrane to the high pressure of the gas mixtures, both at the internal and external sides. In the first case the gas mixture flows through the capillaries, in the second — between the capillaries In the last case one end of the capillaries is obstructed.

(3) Operation at systematically measurable transmembrane pressures in the domain from 1 bar to 30 bar.

(4) Operation at variable temperatures, rigorously controllable, between room temperature and 400 °C In the case of absolute necessity the operation temperature could be enhanced to 500 °C.

(5) Possibility of obtaining gas mixtures with the desired partial pressures of the components and with helium concentrations varying between a few percents and tenths of percents

(6) Preliminary and high vacuum in the installation, with systematical control possibilities of the obtained vacuum and of operation pressures in order to ensure the accuracy of the permeation processes

(7) Systematic measurement of the absolute values of permeate gas pressures These measurements are necessary for type A investigation purpose

(8) Methodical taking control samples (to analyse them by mass-spectrometry) from permeate gas, in view of calculating the efficiency of the separation process implicitly that of membrane selectivity (separation factor)

(9) Taking control samples from the formed gas-mixture for a methodical pursuit of time evolution of helium concentration and also that of the other components

(10) Taking control samples from the refulated gas in view of calculating the helium recovery factor from the gas-mixtures

(11) Measuring and adjusting the refulated gas flow as a function of the optimum helium recovery factor

(12) Methodical verification of each capillary membrane fascicle before including it in the installation

(13) Watching the functional parameters of the installation from a central command and control panel

(14) Security of these main systems in cases of damage or unexpected events (like cut-offs of electrical power and/or cooling water, etc)

(15) Leading of the permeation process during long or very long operation periods in quasi-continuum operation conditions

To ensure these functional requirements the systemic structure of the installation is the following (1) Permeation column (separation, purification), (2) Vacuum system, (3) Gas supply system under pressure, (4) Heating system, (5) Cooling system, (6) Gases and control samples extraction system, (7) Command, control and safety system, (8) Testing system of the capillary membrane-fascicles

In Figs 1 and 2 two general views of our experimental separation installation are shown A schematic presentation is given in Fig 3 The meanings of symbols used are the following PST — cooling water relay, SMIS — mechanical system (valve) for „close upwards", RAR — cooling water tank, PRAR — cooling water recirculation pump, BR — battery of taps, CC — direct current, CA — alternative current, MR — cooling mantle, PD — diffusion pump, PVP — preliminary vacuum pump, CGP — permeate gas chamber, CGR — refulate gas chamber, RI — heating resistance, JVJ — high vacuum gauge, JI — interchangeable gauge, JVP — preliminary vacuum gauge, RS — flow resistance, M Hg — mercury manometer, T_1, T_2, T_3 — iron — constantan thermocuples, BGA — supply gas bottle, BGR — refulate gas bottle, SLP—GP — extraction system of permeate gas samples, SLP—GA — extracting system of supply gas samples, DI—GA — supply gas introduction system, under pressure, DIF — testing system of the capillary membrane fascicles, MB — bourdon pressure manometer, SLP—GR — system of control sample extraction from the refulated gas

4 2 *Experimentation of the separation installation Functional testing of the separation installation* The functional testing, both sequential and general, of the separation-purification installation, is a very complex operation, needing a lot of time It implies unavoidably, the necessity to remedy some executional or assembling defects, and even small retouches concerning the functional conception of parts of the construction A detailed description of the stages and results of the whole

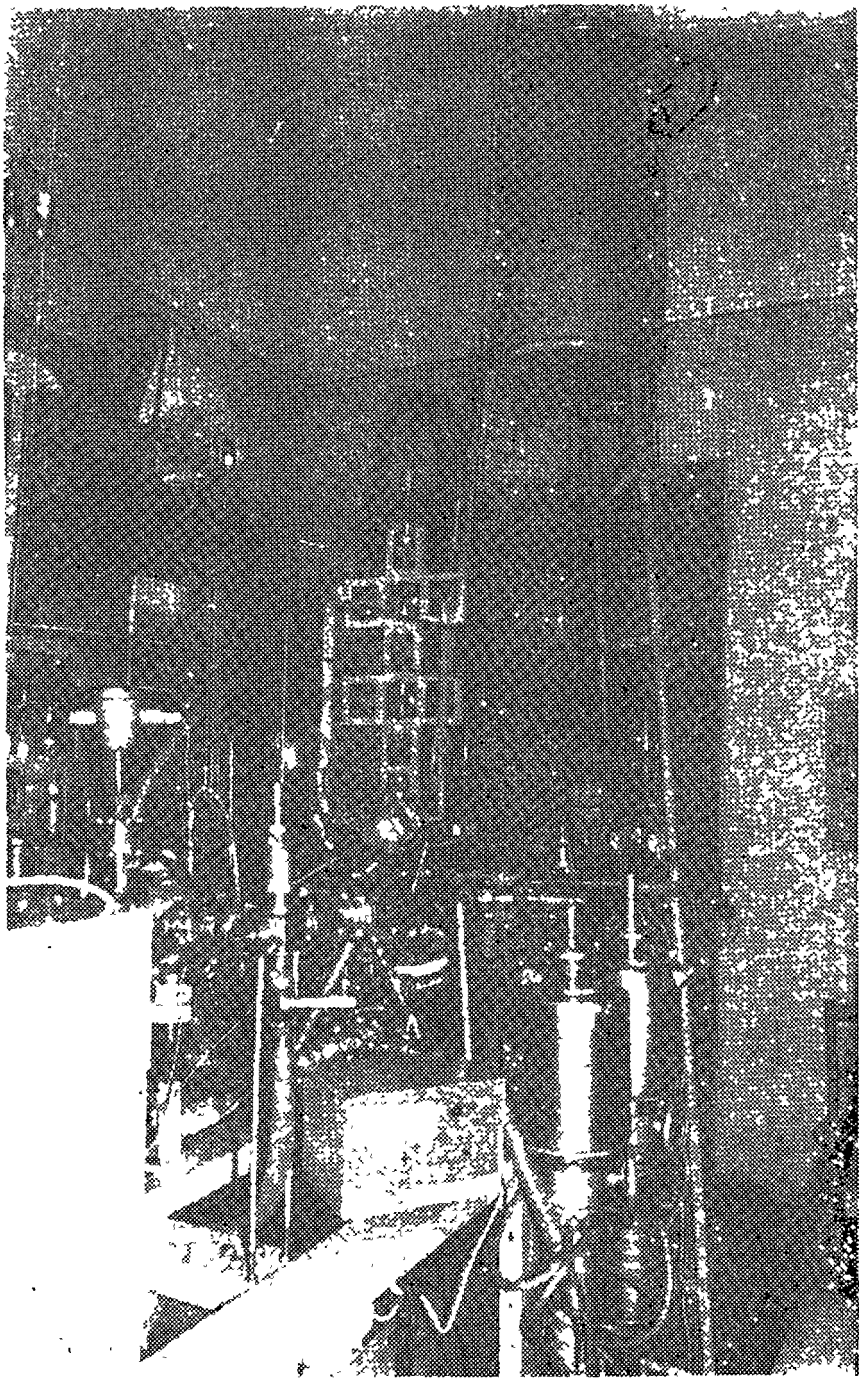

Fig. 1.

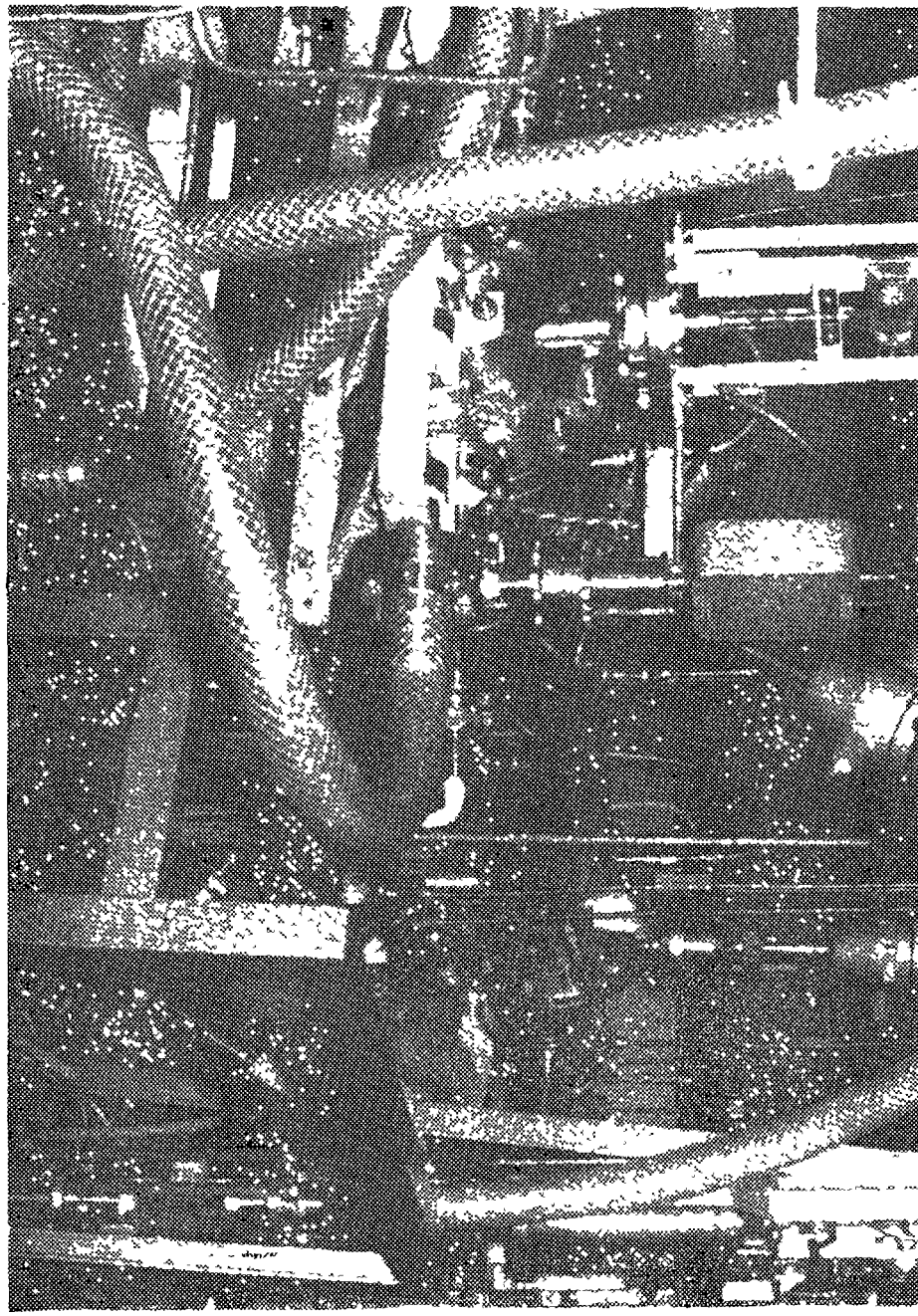

Fig. 2.

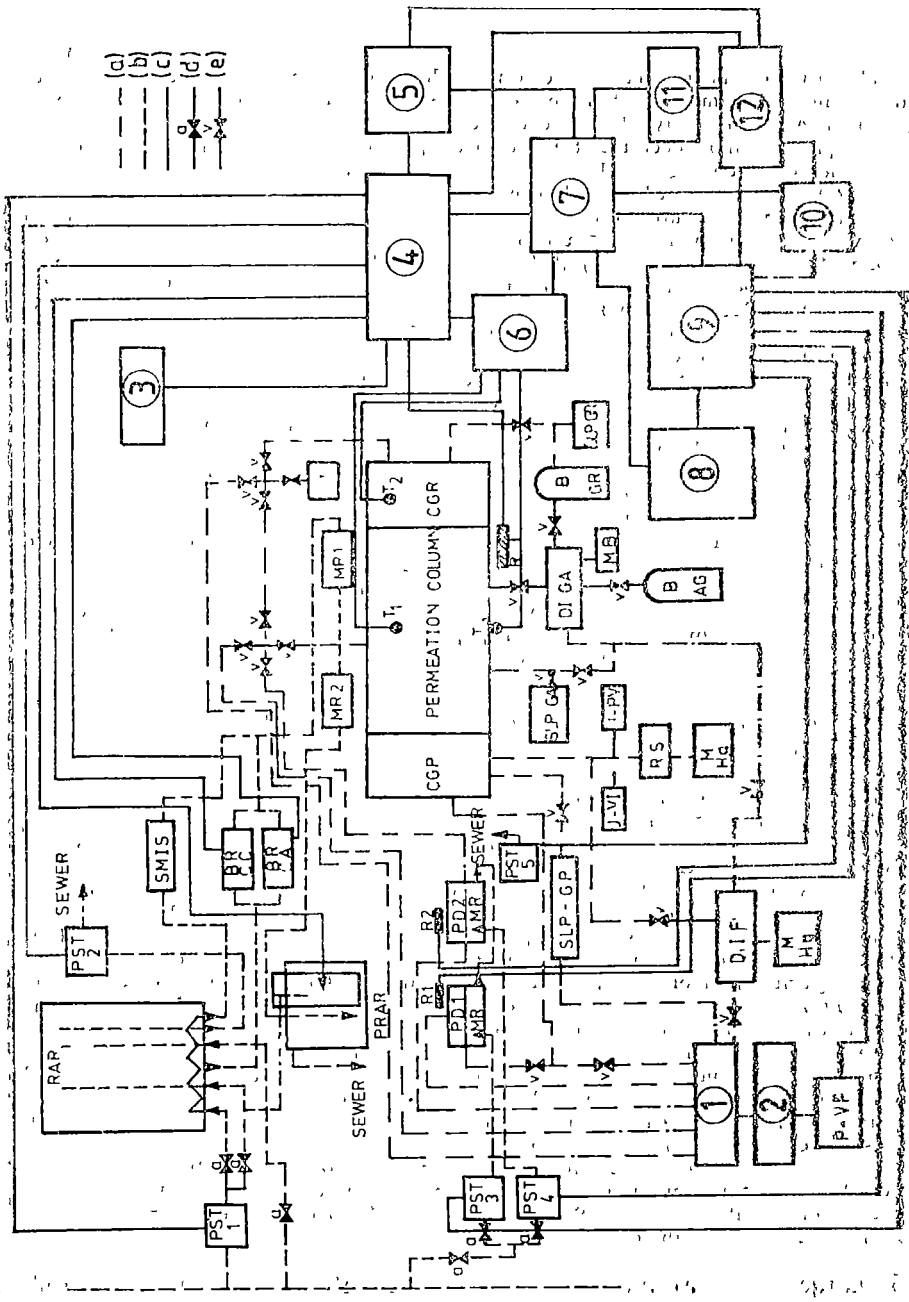

Fig 3 Installation for helium separation and purification through diffusion and/or activated diffusion in capillary membranes Schematic presentation. 1. vacuum distributor. 2. vacuum reservoir, 3 ventilation group, 4 command, control and safety block for separation column, 5. column signalization block, 6 temperature measurement and control block, 7. power supply block, 8. programmed command block for vacuum system, 9 command, control and safety block for vacuum system, 10 vacuum system signalization block, 11 battery programmed loading block, 12. storage battery (24 V — CC), (a) vacuum line, (b) cooling water line, (c) command and power supply line, (d) water tap, (e) vacuum valve

functional testing, of our installation, including both sequential and general testing operation, would exceed the aim and framework of the present paper, but it can be found in paper [29] Therefore we give here a scheme only of the general conception on which the tests were based

(1) Sequential and general testing of each operative system of the installation

(2) Functional testing of the installation as a whole

On the base of ,,at heat'' tests of type (G), (H) [29] that means the operation of installation at temperatures and pressures respectively of 20—200°C and 5—20 bar, the following conclusions were drawn (a) A vacuum of 10^{-4} torr in the permeate gas chamber can be obtained in a relatively short time (2—3 h), (test (G) [29]) (b) After 3 h, from decoupling the vacuum line of the permeate gas collection chamber, the pressure increased from 10^{-1} torr to 0,1 torr (test (H) [29]), because of surface degasation and leakages (c) In the specific conditions of test (G), the 19 fascicles of Pyrex capillary membranes (one fascicle having = 200—250 membranes) can ,,transport'' to the permeate gas collection chamber, a helium flux corresponding to a pressure increase of approximatively 100 torr/h, that is 300 torr during 3 h (d) According to the above conclusions, we can estimate the maximum impurification limit, in the case of operation conditiong (G), (H), for permeate helium, to 3 5 $\times 10^{-2}$ % (0 1 torr/300 torr) Thus the purity limit of helium corresponds to ≈99 96% A high vacuum and a long degasation period, with a more careful choice of the tightness elements to be used, could enhance the upper limit of helium purity to 99 99%

The testing of the capillary membrane fascicles Detailed presentation of the long series of experimentations concerning the capillary membrane fascicles would also exceed the framework of the present paper They are presented in paper [29] Here we mention only the main conclusions The technology of capillary membrane — fascicle building up must be, in itself, the object of systematic laboratory investigations Paper [31] outlines the main results of our investigations concerning the technology of capillary membrane fascicle building up, giving also some of the implications on the purity limit of permeate helium

The experimental results of the tests performed on one of those fascicles, to be included in our separation and high purification installation, are presented in Fig 4 The fascicle in question, F17, was built up by the combined technology "IGFS", being codified as F17 IGFS—200 PF Fig 4 presents, for aims of comparison, the results obtained in the "witness test" Analysing the results of the three experiments performed with the above-named fascicle, the conclusions are similar to those drawn from the experiments performed with the E6—IGED FS fascicle [31], namely (a) The leakage-degasation rate is not sensitive to the great pressure variations in the "pressure chamber" of the testing system (b) The leakage-degasation rate (DSD) is continuously decreasing if the time of previous evacuation (TPV) is increased, even if the pressure in the "pressure chamber" (PCP) does increase 24 times (from 1 bar to 24 bar of CO_2), going from experiment number 2 to experiment number 3 (c) After 26 hours of previous evacuation (TPV = 26 h) the leakage-degasation flow of the fascicle is close to the "witness test" value, i e DSD = 3 8 $\times 10^{-7}$ torr l/s

4 3 *High purification possibilities of helium* The results of the experiments performed with the capillary membrane fascicles, in particular with those of F17 IGFS—200 PF, allow us to estimate the purity limit of obtainable helium, if our installation is equipped with fascicles of the type and characteristics of those discussed above Taking into account that one fascicle contains 200 membranes, the leakage-degasation flow for a single membrane, $(DSD)_{membr}$, will be 1 9 $\times$ $\times 10^{-9}$ torr l/s On the other hand, the results presented in paper [31] show, for a single capillary membrane of the above mentioned type and dimensions, operating at a pressure between 20—24 bar and a temperature of 30°C, a limit value of permeate helium flux of ≃3 5 $\times 10^{-5}$ torr l/s Thus, the impurification of permeate helium, caused by the rate of leakage-degasation of membrane, can be estimated at ≃5 $\times 10^{-3}$% If our separation-purification installation will be equipped with fascicles having similar operating parameters, like those of fascicle F17 IGFS—200 PF, and if the natural gas-mixture supply has an important helium concentration, then we can hope for a permeate helium purity limit of ≃99 995% Papers [24—33] describe a part of our investigation efforts and results in this direction

5 **Large scale applications of nonconventional helium separation-purification methods.** There are some interesting cases of large scale application of diffusion phenomena to the separation and purification of helium and/or hydrogen from gaseous mixtures [11, 14, 34—40]

5 1. Interesting results were obtained with the Permasep Project of the American Du Pont Company [35—38] The main parameters of the permeator

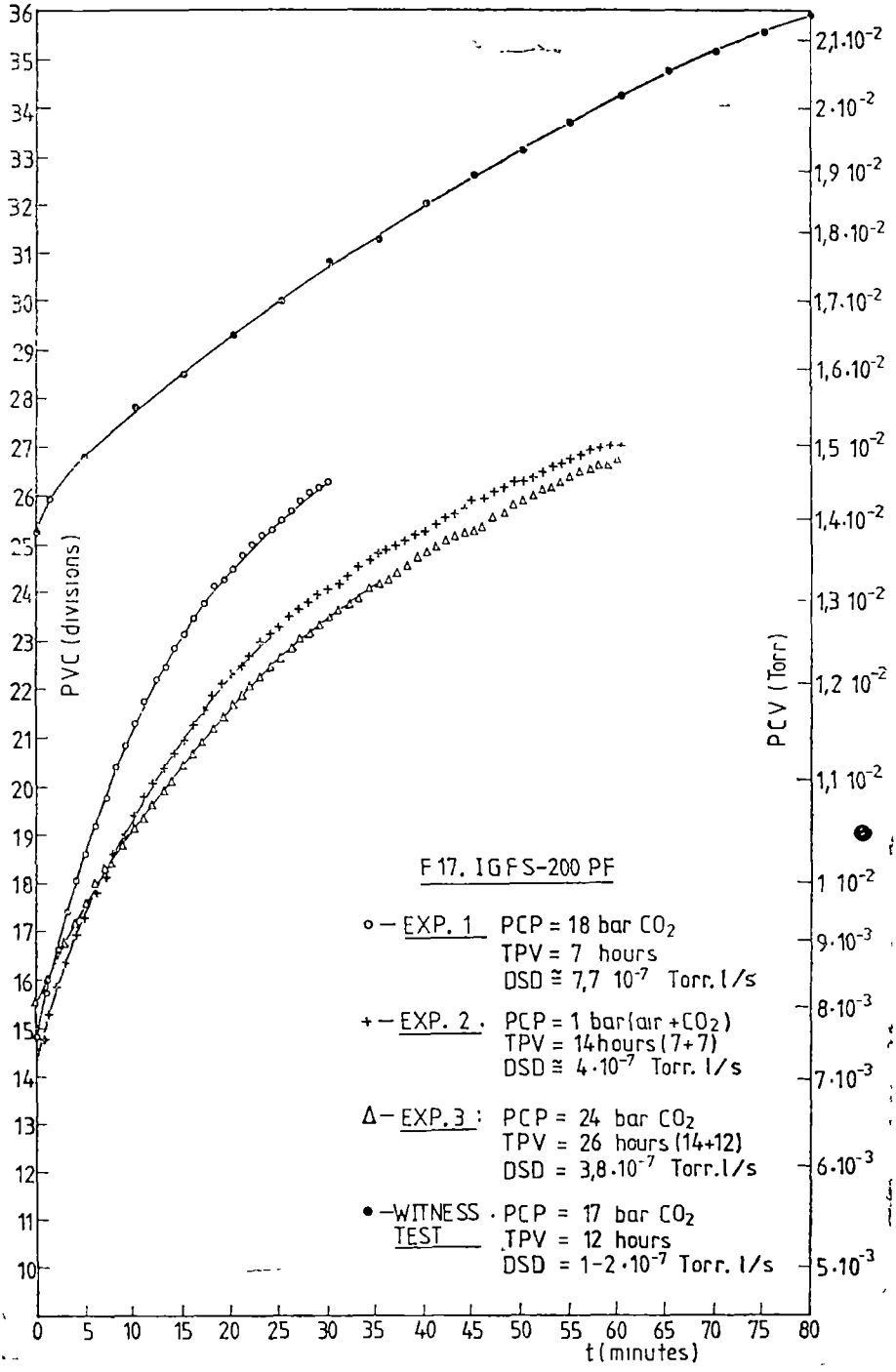
PVC (divisions)
PCV (Torr)
t (minutes)
F 17. IGFS-200 PF
o — EXP. 1 PCP = 18 bar CO2
TPV = 7 hours
DSD ≅ 7,7 10-7 Torr. l/s
+ — EXP. 2. PCP = 1 bar(air +CO2)
TPV = 14hours (7+7)
DSD ≅ 4·10-7 Torr. l/s
Δ — EXP. 3 : PCP = 24 bar CO2
TPV = 26 hours (14+12)
DSD = 3,8·10-7 Torr. l/s
• — WITNESS TEST · PCP = 17 bar CO2
TPV = 12 hours
DSD = 1-2·10-7 Torr. l/s

Fig 4 ..

are length 5 5 m and internal diameter 300 mm The membranes used are hollow-fibres of polyester, having an outside diameter of 50μ, and an inside diameter of 18μ. The permeator includes 50 millions of such membranes, having an active surface area of 2×10^4 m². Permeation is operated at 38°C and at a trans-membrane pressure of 45 bar. The refinery capacity is of 125,000 STP m³/day ($\cong$40 millions STP m³/year). It was destined to hydrogen and/or helium separation from gas mixtures In the case of hydrogen the obtained purity value is of 95% in a single separation stage.

5.2 Paper [40] indicates that a new prototype of helium extraction, under construction in Canada, will open the way to lower cost helium recovery. This plant, representing the unified efforts of the government and the private industry, is designated to process natural gases with a helium content of 0 05 to 0.2%, using diffusion separation techniques

5.3. The Japanese Teijin Ltd Company [38, 39] has developed a noncryogenic method of helium recovery from natural gases This method is based on the selective permeability of some hollow fibres made up of synthetic materials. The separation is operated at room temperature and a pressure of about 29 bar. Compared to the conventional, cryogenic, helium recovery/purification methods, implying removal of other gases by liquefaction and/or absorption at low temperatures, the Teijin process features a 30% saving in operating cost at about the same initial investments.

Acknowledgements. The authors would like to express their sincerest thanks to Professor Ioan Ursu for his permanent interest and help in the development of this research field

REFERENCES

1 I Ursu, *Atomic Energy*, Ed Ştiinţifică, Bucureşti, 1973
2. I. Ursu, *Physics and Technology of Nuclear Materials*, Ed Acad RSR, Bucureşti, 1982
3 I Ursu, I N Mihăilescu, A. M Prokhorov, V I Kononov, *Interaction of Laser Radiation with Metals*, Ed Acad RSR, Bucureşti, 1986
4 F J Norton, *Gen Elec Rev*, September, 1952
5. F J Norton, *J Amer Ceram Soc.*, **36,** 90 (1953)
6 F J Norton, *Trans AIME*, **230,** 595 (1964)
7. K B McAffe, „Diffusion Separation", in *Kirk Othmer Encyclopedia of Chemical Technology*, Ed Wiley Interscience, New York, 1960, p 297
8 K B McAffe, *Bell Lab Record*, **39,** October 1961
9. K B McAffe, *Chem Eng Progr*, **54,** 106 (1958)
10 N Melnyk, H W Habgood, *Can Mining Metall Bulletin*, Oct, **768,** (1961)
11 L M Litz, G E Smith, *Union Carbide Res Inst Rept UCRI-701* (1972)
12 S A Stern, T F Sinclair, J J Gareis, N P Vahldieck, P H Mohr, *Ind. Eng Chem*, **57,** 49 (1965)
13 R B McBride, D. L McKinley, *Chem Eng Progr*, **61,** 81 (1965)
14 K Kammermeyer, „Gas and Vapor Separations by Means of Membranes", *Progress in Separation and Purification*, E S Perry Ed, vol 1, Wiley Interscience, New York, 1968, p. 335
15 D Bender, *Dissertation*, Technischen Universitat, Berlin, 1975
16 Sun-Tak Hwang, K Kammermeyer, *Membranes in Separation*, Wiley Interscience, New York, 1975
17. M. Ohno, T Morisue, O Ozaki, H Heki, T Miyauchi, *Radiochem Radioanal. Letters*, **27,** 299–306 (1976)
18. M. Ohno, T Morisue, O. Ozaki, T Miyauchi, *J Nucl Sci and Technology*, **15,** 376–386 (1978)

19 M Ohno, H Heki, O Ozaki, T Miyauchi, *J Nucl Sci and Technology*, **15**, 668—677 (1978)
20 A Kakuta, O Ozaki, M Ohno, *J. Polymer Sci*, **16**, 3249—52 (1978)
21 T Morisue, O Ozaki, O Ohno, *Toshiba Review*, Nr 123, Sept —oct. 1979
22. H S Carslaw, J C. Jaeger, *Conduction of Heat in Solids*, Clarendon Press, Oxford, 1959.
23 H Abramowitz, A Stegun, *Handbook of Mathematical Functions*, Nat Bur Stand Appl Math Ser, 55 (1965)
24 I Mastan, A Toderean, C Cosma, M Oană, O Cozar, V Znamirovschi, *Proc of 2-nd Nat Symp on Meth, Models and Techn in Physics and Related Fields*, Cluj-Napoca University, October 14—15, 1983, p 51—54
25 I. Mastan, A Toderean, C Cosma, M Oană, O Cozar, V Znamirovschi, „Modern Problems of Physics", vol. IV, Cluj-Napoca University, 1984, p 4—16
26. I. Mastan, C Cosma, A Toderean, V Znamirovschi, O Cozar, „Modern Problems of Physics", vol V, Cluj-Napoca University, 1985, p 76—92
27 I Mastan, A Toderean, C Cosma, O Cozar, V Znamirovschi, „Modern Problems of Physics", vol V, Cluj-Napoca University, 1985, p 94—104
28 I Mastan, C Cosma, A Toderean, O Cozar, V Znamirovschi, *Report to Contract* 91/1984, Cluj-Napoca University, December 1984, 179 pp
29 I Mastan, C Cosma, A. Toderean, V Znamirovschi, O Cozar, *Proc of 3-td Nat Symp on Meth; Models and Techn in Phys and Related Fields*, Cluj-Napoca University, September 26—27, 1986, p 33—38
30. I. Mastan, *Dissertation*, Cluj-Napoca University, 1987
31 I Mastan, A Toderean, M Oană, C Cosma, V Znamirovschi, *Report to Contract* 91/1981, Cluj-Napoca University, December 1981
32 I Mastan, A Toderean, M Oană, C. Cosma, V Znamirovschi, *Report to Contract* 91/1982, Cluj-Napoca University, December 1982
33 I Mastan, C Cosma, A Toderean, O Cozar, V Znamirovschi, M Oană, *Report to Contract* 91/1983, Cluj-Napoca University, December 1983
34. S A Stern, „Industrial Applications of Membrane Processes The Separation of gas Mixtures", *Proc of Symp, May* 19—20, 1968, Birmingham, Alabama, USA
35 J E Jolley, *U S Patent* 3, 172, 741 (1965)
36 W. D Lewis, S A Rogers, *U S Patent* 3, 198, 335 (1965)
37 Du Pont Co 's *Permasep Technical Bulletins 105* and *110* (1972)
38 *News item C* and *EN*, **50,** 11 (1972)
39 *Chem Eng*, **79,** 40 (1972)
40 T. B Rhinehammer, L Wittenberg, „An Evaluation of Fuel Resources and Requirements for the Magnetic Fusion energy Pogram", *Report to Contract EY-76-C-04-0053*, Monsanto Res. Corp, USA, October 1978, p. 57

STUDIA UNIV BABEŞ-BOLYAI, PHYSICA, XXXIII, 1, 1988

ON THE INTERNAL THIRRING EFFECT

Z. GÁBOS*

Dedicated to Professor IOAN URSU on his 60 th anniversary

Received. March 7, 1988

ABSTRACT. — We study the gravitational effects given by a mass distributed on a rotating spheric surface, near the center of the sphere The rest mass M_0 is uniformly distributed on the spherical surface of radius A, and the angular velocity $\vec{\Omega}$ is time dependent

1. **The case** $\dot{\vec{\Omega}} = 0$ The studies concerning the gravitational effects which appear inside a uniformly rotating sphere surface have been initiated by H Thirring [1]. Starting with the Einstein equation, and applying the method of the weak field, using as a test body a material point, for translational motion H. Thirring obtained the equation

$$\ddot{\vec{x}} = -\operatorname{grad}\varphi + \frac{8\lambda}{3A}(\vec{\Omega}\, x\, \dot{\vec{x}}), \tag{1}$$

where

$$\varphi = -\frac{2\lambda\Omega^2}{15A}(x_1^2 + x_2^2 - 2x_3^2), \qquad \lambda = \frac{kM_0}{c^2} \tag{2}$$

(λ is the gravitational radius of the source, the third axis was considered in the direction of $\vec{\Omega}$ which had the components 0, 0, Ω)

Lately, this problem has been reconsidered, using another method namely the post-Newtonian approximation [5] The test body has been considered a spinning particle with the rest mass m_0, the study being also generalized on the rotation effects If we accept a second order approximation the fundamental quantities are the scalar potentials Φ, Ψ, and the vector potential $\vec{\xi}$ Using the general expressions of the potentials, for the studied case we obtain the functions .

$$\Phi = -\frac{\lambda c^2}{A}, \qquad \Psi = -\frac{\lambda A\Omega^2}{c^2} - \frac{\lambda\Omega^2}{10c^2A}(x_1^2 + x_2^2 - 2x_3^2), \tag{3}$$

$$\vec{\xi} = -\frac{4\lambda}{3cA}(\vec{\Omega}\, x\, \vec{x}) \tag{4}$$

The motion of translation can be described using the Lagrangian [5]

$$L_1 = \frac{m_0}{2}v^2 + \frac{m_0}{8c^2}v^4 - m_0\Phi - \frac{m_0}{2c^2}\Phi^2 - m_0c^2\Psi - \frac{3m_0}{2c^2}\Phi v^2 + m_0c(\vec{\xi}, \vec{v}). \tag{5}$$

* *University of Cluj-Napoca, Faculty of Mathematics and Physics, 3400 Cluj-Napoca, Romania*

Due to the translation effect we obtain from (5), using the Euler-Lagrange equation, the equation (1) which is valid for $\dot{\vec{\Omega}} = 0$. The function φ is replaced by the function φ' which contains another numerical factor

$$\varphi' = -\frac{\lambda\Omega^2}{10A}(x_1^2 + x_2^2 - 2x_3^2) \tag{6}$$

Concerning the rotation effect we get a precession described by the equation

$$\frac{d\vec{\omega}_0}{dt} = (\vec{K} \times \vec{\omega}_0), \tag{7}$$

where

$$\vec{K} = \frac{4\lambda}{3A}\vec{\Omega}, \tag{8}$$

and $\vec{\omega}_0$ is the angular velocity of the test body in the rest frame

In the following we will study this problem in a more general case, namely for $\dot{\vec{\Omega}} \neq 0$ We will try to show which from the functions (1) or (6) is the most exact one

2 **The case** $\dot{\vec{\Omega}} \neq 0$ We will study this more general case using a method given by the author [3], which is in fact a version of the post-Newtonian approximation We will take the Lagrangian given by I G Fichtenholtz [2] valid (in the second order approximation) for a system of material points

$$\begin{aligned} L = {} & \frac{1}{2}\sum_a m_{0a} v_a^2 + \frac{1}{8c^2}\sum_a m_{0a} v_a^4 + \frac{k}{2}\sum_{a,b}{}' \frac{m_{0a}m_{0b}}{r_{ab}} - \\ & - \frac{k^2}{6c^2}\sum_{a,b,c}{}' m_{0a} m_{0b} m_{0c}\left(\frac{1}{r_{ab}^2 r_{ac}} + \frac{1}{r_{ba} r_{bc}} + \frac{1}{r_{ca} r_{cb}}\right) + \\ & + \frac{k}{4c^2}\sum_{a,b}{}' \frac{m_{0a}m_{0b}}{r_{ab}}\left[3v_a^2 + 3v_b^2 - 7(\vec{v}_a, \vec{v}_b) - \frac{1}{r_{ab}^2}(\vec{v}_a, \vec{x}_b - \vec{x}_a)(\vec{v}_b, \vec{x}_b - \vec{x}_a)\right], \end{aligned} \tag{9}$$

where by comma in the notation we indicated that from the sum the selfaction terms are avoided

As test body will be chosen a spheric gyroscope which is in fact a classical spherical, homogeneous body with the rest mass m_0 and the small radius a. We considered that the material points from the studied system are contained in the source body or in the gyroscope, and these material points are subjected to some constrains After a simple algebra one obtains a new Lagrangian which contains the expression of L_1 given by (5) and the supplementary contribution

$$L_2 = \frac{m_0}{5} a^2\omega_0^2 - \frac{8m_0\lambda a^2}{15A}(\vec{\Omega}, \vec{\omega}_0), \tag{10}$$

which gives information on the rotation of the gyroscope (The radius being small the translation-rotation interference terms can be neglected in the kinetic energy of the gyroscope) Using the function

$$L = L_1 + L_2, \tag{11}$$

and the standard procedure, we get the equation

$$\ddot{\vec{x}} = -\text{grad}\,\varphi' + \frac{8\lambda}{3A}(\vec{\Omega} x \dot{\vec{x}}) + \frac{4\lambda}{3A}(\dot{\vec{\Omega}} x \vec{x}), \tag{12}$$

valid for the translation motion, where $\vec{x}$ is the position vector of the center of gyroscope.

The function L given by (11) and the Euler-Lagrange equation

$$\frac{d}{dt}\left(\frac{\partial L}{\partial \vec{\omega}_0}\right) = \left(\vec{\omega}_0 x \frac{\partial L}{\partial \vec{\omega}_0}\right) \tag{13}$$

will give the equation concerning the rotation effect as

$$\dot{\vec{\omega}}_0 = \frac{4\lambda}{3A}(\vec{\Omega} x \vec{\omega}_0) + \frac{4\lambda}{3A}\dot{\vec{\Omega}}. \tag{14}$$

3. **Conclusions.** Because the method from the previous section also leads at the function φ', we can say that function (6) is more exact.

For the Newtonian energy of the gyroscope, from (12) and (14) we obtain:

$$\frac{d}{dt}\left(\frac{m_0}{2}v^2 + m_0\varphi'\right) = \frac{4\lambda}{3A}(\dot{\vec{\Omega}}, \vec{N}), \tag{15}$$

where

$$\vec{N} = m_0(\vec{x} x \dot{\vec{x}}), \tag{16}$$

respectively

$$\frac{d}{dt}\left(\frac{\Theta}{2}\omega_0^2\right) = \frac{4\lambda\Theta}{3A}(\dot{\vec{\Omega}}, \vec{\omega}_0), \tag{17}$$

where

$$\Theta = \frac{2}{5}m_0 a^2. \tag{18}$$

The time evolution of the orbital angular momentum can be obtained from (12) and given by the equation

$$\frac{\overrightarrow{dN}}{dt} = \vec{M} + \frac{8\lambda m_0}{3A}[(\vec{x}, \dot{\vec{x}})\vec{\Omega} - (\vec{\Omega}, \vec{x})\dot{\vec{x}}] + \frac{4\lambda m_0}{3A}[\dot{\vec{\Omega}}\vec{x}^2 - (\dot{\vec{\Omega}}, \vec{x})\vec{x}], \tag{19}$$

which contains the vector $\vec{M}$ of components

$$\vec{M}\left(-\frac{3\lambda m_0\Omega^2}{5A}x_2x_3, \frac{3\lambda m_0\Omega^2}{5A}x_1x_3, 0\right). \tag{20}$$

From (19) we obtain for N_3 the equation

$$\frac{dN_3}{dt} = \frac{4\lambda m_0\Omega}{3A}\frac{d}{dt}(x_1^2 + x_2^2) + \frac{4\lambda m_0}{3A}(x_1^2 + x_2^2)\frac{d\Omega}{dt}. \tag{21}$$

The above equations offer us the possibility to draw the following conclusions concerning the energy and the angular momentum:

In the case of $\dot{\vec{\Omega}} = 0$, the mechanic energy of gyroscope is conserved. If $\dot{\vec{\Omega}} \neq 0$, due to a coupling between the rotation angular momentum of the source and the orbital and rotational angular momentum of the gyroscope the energy of the gyroscope is variable;

Because the coefficients of $\dot{\Omega}$ from the equations (14) and (21) are positive, as compared to the third component of the orbital angular momentum and the rotational momentum, we can conclude that an engagement effect appears;

The modulus of the angular velocity $\vec{\omega}_0$ for the $\dot{\vec{\Omega}} = 0$ case is conserved. In the case $\dot{\vec{\Omega}} \neq 0$ this conservation is not perserved;

The effects are very small, being determined by quantities λ/A, Ω and $\dot{\Omega}$.

REFERENCES

1. H. Thirring, *Phys Z*, **19,** 33 (1918), **22,** 29 (1921).
2. I. G. Fichtenholtz, *JETF*, **20,** 233 (1950)
3. Z. Gábos, *An. Şt Univ „Al. I Cuza" Iaşi*, **5,** 101 (1959)
4 L. I. Schiff, *Phys Rev Lett*, **4,** 215 (1960)
5 S. Weinberg, *Gravitatia i kosmologia*, Moskva, 1975, p 229–259
6 B. Mashhoon, F W Hehl, D S Theiss, *Gen Rel and Grav*, **16,** 711 (1984).

STUDIA UNIV BABEŞ-BOLYAI, PHYSICA, XXXIII, 1, 1988

EXPERIMENTS IN CW NMR IMAGING

AL. NICULA*, M. TODICA* and S. AŞTILEAN*

Dedicated to Professor IOAN URSU on his 60 th anniversary

Received March 14, 1988

ABSTRACT. — The paper demonstrates the obtainment of one-dimensional projection spin density by CW NMR Imaging experiments The test were performed by water-filled phantoms

Introduction. In the past ten years, a variety of techniques have been proposed and demonstrated, which allow of spatial discrimination and mapping of the magnetic resonance transitions in heterogeneous objects

The elementary principles of NMR Imaging are now well established [1] Recently, the EPR experiment in magnetic field gradients brings about new opportunities in magnetic resonance imaging [2, 3]

Reconstruction from projections offers several advantages when compared to those techniques that depend upon transient perturbations of the NMR response [4] Currently, in order to obtain the one dimensional projection in frequency space, the free induction decay following a single r f pulse was digitized and Fourier-transformed

The aim of this paper is to present the preliminary imaging experiment carried out on C W NMR spectrometer JEOL HNM 3H—60 If the static magnetic field $\vec{B}_0$ and the radiofrequency magnetic field B are uniform over the object, the NMR spectrum in the presence of the linear gradient will correspond to a one-dimensional projection, such as that EPR Imaging convoluted spectrum.

For testing our device imaging, these studies were performed by using water-filled phantoms In this experiment, both thin-walled glass capillaries contained pure water The recorded spectrum in the presence of a field gradient represents a one-dimensional projection of the H_2O content of the capillaries, integrated over planes perpendicular to the gradient direction, as a function of the gradient coordinate The experiments demonstrate the capacity of this technique to generate one dimensional distributions of spins within objects

Field gradient coils. A linar G_x field gradient, parallel to the homogeneous $H(t)$ field, was used The gradient was obtained by means of an anti Helmholtz pair of coils, supplied by a variable stabilised power source, ranging from zero to 100 volts Each coil is made of Cu 0 1 mm turns wire The interior diameter is $d = 98$ mm, the exterior diameter is $D = 130$ mm, and the thickness of each coil, is $e = 1{,}8$ mm The distance between the coils is $2b = 45$ mm

For the median region, of about 10 mm width, situated on the symmetrical axis of the coils, the gradient is practically linear [5]

A gradient of about 0,30 G/cm, can be obtained by these coils

The arrangement of the coils is shown in Fig 1

* *University of Cluj-Napoca, Faculty of Mathematics and Physics, 3100 Cluj-Napoca, Romania*

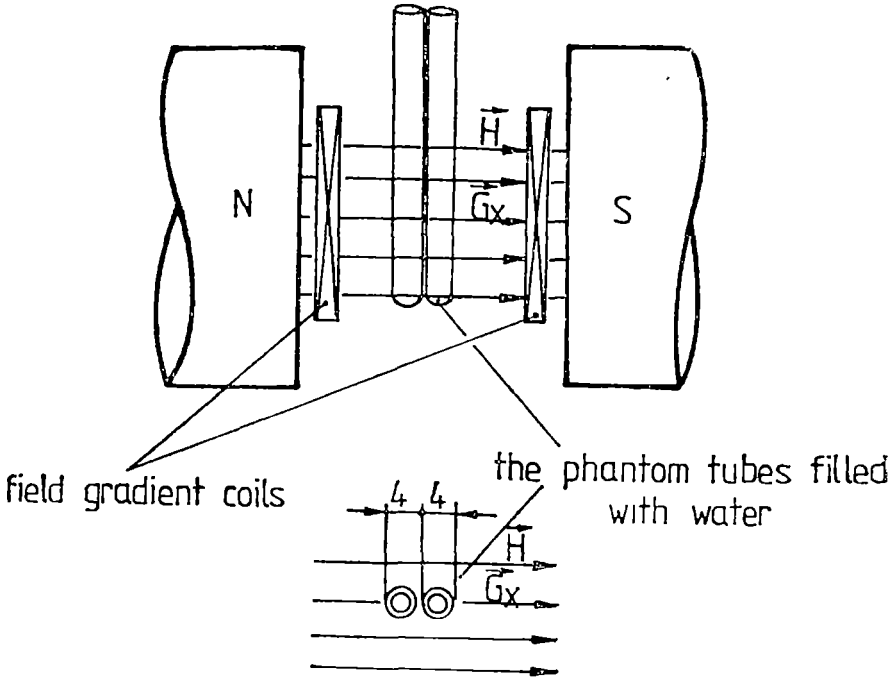

Fig 1 The arrangement of the phantom tubes in the magnetic field The tubes are set parallel to the magnetic field

Experimental arrangement and results.

Two glass tubes filled with water, with an exterior diameter of 4 mm, and the thickness of the walls of 0 7 mm set side by side, were employed. Thus the distance between its centers is 4 mm, and the space between the probes is 1 4 mm The tubes are set perpendicularly on the magnetic field (Fig 1).

Initially, the tubes were placed as shown in Fig 2 The absorbtion spectrum was recorded both with and without the magnetic field gradient A single resonance signal was recorded in both cases, Fig 3

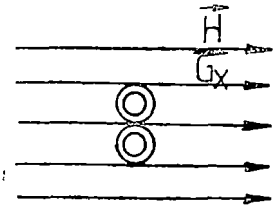

Fig 2 The tubes are set perpendicularly to the magnetic field

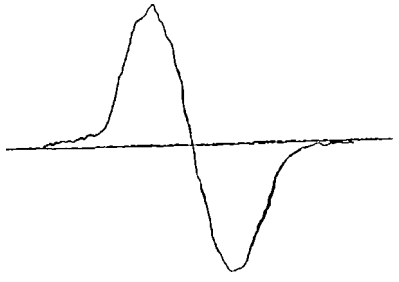

Fig 3 The recorded absorbtion spectrum, both in the presence and in the absence of the magnetic field gradient, when the tubes are placed perpendicularly to the magnetic field.

Then, the tubes were placed as shown in Fig. 1. If the magnetic field gradient is absent, the recorded signal is the same as in the previous case. No modification is observed if the tube system is rotated.

But if the field gradient is superimposed to a homogeneous field, the resonance line is broadened and it starts to separate into two components (Fig. 4). The two lines corresponding to the two phantoms tubes are completely separated for a field gradient of about 0,30 G/cm.

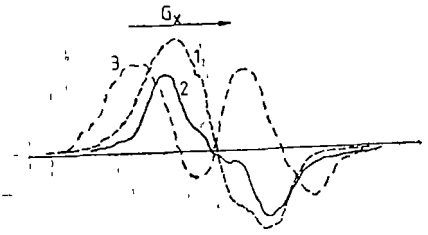

Fig 4 The absorbtion spectrum in the presence of the magnetic field gradient when the tubes are placed parallel to the magnetic field 1 $G_x = 0{,}10$ G/cm; 2. $G_x = 0{,}15$ G/cm, 3 $G_x = 0{,}30$ G/cm.

The amplitude of the signals is smaller as the spin quantity yielding a signal is half of the quantity of the spins which yielded the signal shown in Fig. 3. Only one of the signal components remains if one of the tubes is eliminated This experiment demonstrates that resonance condition $\omega_0 = \gamma[H(t) + G_x \quad x]$ was fulfilled separately for each of the phantom tubes and that the absorbtion signals are each yielded by a different tube. Thus, a „spin imaging resonance" was achieved.

Conclusions. If a magnetic field gradient is superimposed to a homogeneous field, the local resonance condition is modified and that results in the altering of the absorbtion spectrum For a certain value of the gradient, completely separate signals corresponding to the different regions of the sample are recorded. Conclusions referring to the spatial distribution of the spins can be drawn from the analysis of the absorbtion spectrum. The phenomenon was practically put in evidence by the JEOL, JNM 3H—60 spectrometer which had been modified as shown above.

BIBLIOGRAPHY

1. R R Ernst, *Quaterly Rev. Biophysics*, **19**, 3/4, p 183—220 (1987)
2 S S. Eaton, G R. Eaton, *Spectroscopy*, **32** (1) 1986
3 Al Nicula, S Nicula, L. Giurgiu, I Ursu, *Studia Univ Babeş-Bolyai, Physica*, **31** (2), 1986, pp 3—8
4. P. C Lauterbur, C M Lai, *IEFE Trans Nucl Sci*, vol NS—27, No 3 (1980)
5 Al. Nicula, S Aştilean, M Todică, S Nicula, *Studia Univ. Babeş-Bolyai, Physica*, **32** (2) (1987)

STUDIA UNIV BABEŞ-BOLYAI, PHYSICA, XXXIII, 1, 1988

MAGNETIC BEHAVIOUR OF THE α-(Al_2O_3—Fe_2O_3) OXIDIC SYSTEM

LILIANA POP*, LIVIU STĂNESCU*, OLIVIA POP* and IULIU POP*

Dedicated to Professor IOAN URSU on his 60 th anniversary

Received March 15, 1988

ABSTRACT. — The temperature dependence of the reciprocal magnetic susceptibility between 100 and 1,250 K in the magnetic field strenght of 9 500 Gs for the set of four samples of α-(Al_2O_3—Fe_2O_3) biphasic system was investsgated The reciprocal magnetic susceptibility has no linear but step variation with the temperature increase, determined by the superposition of the antiferromagnetic phase on the paramagnetic phase

1. **Introduction.** The oxidic system α-(Al_2O_3—Fe_2O_3) crystallizes in the conrundum type of structure, and gives rise to the solid solutions only in a narrow range of concentration, up to 5 mol % α-Fe_2O_3. In the previous paper [1] we have reported the magnetic behaviour of the α-(Fe_2O_3—Al_2O_3) oxidic system for the samples with the concentration 1; 3, 5, 7; 10, 20; 40; 60 and 80 mol % of α-Al_2O_3 The system is antiferromagnetic and has a magnetic spin structure of α-Fe_2O_3 type in the solid solutions regions, i.e. up to 20 mol % α-Al_2O_3 The Néel temperature for the monophasic system decreases monotonously with the α-Al_2O_3 concentration increase, while for the biphasic system is concentration independent The temperature of the spin reorientation for the solid solutions monotonously decreases with the α-Al_2O_3 concentration increase The magnetic susceptibility of the α-(Fe_2O_3—Al_2O_3) system in the paramagnetic region is practically temperature independent in a temperature range of about 100—200 degrees where the magnetic order is not destroyed yet. So, it was interesting to study the magnetic behaviour for the samples rich in Al_2O_3, even in the biphasic region.

2 **Samples preparation and experimental.** From the α-(Al_2O_3—Fe_2O_3) system was prepared a set of samples with the concentration 4, 7, 10 and 15 mol% α-Fe_2O_3 For the preparation of the system we used $Al_2(SO_4)_3$ and $Fe(NH_4)(SO_4)_2$ treated with NH_4OH in order to obtain $Al(OH)_3$ and $Fe(NH_4)(OH_2)$, respectively After filtration, the two hydroxides were treated with HNO_3 resulting $Al(NO_3)_3 \cdot 6H_2O$ and $Fe(NO_3)_3 \cdot 6H_2O$ The obtained salts were dried in the temperature range of 333—343 K in order to avoid the crystallization water loosing From the aluminium and iron nitrates the proportions for the corresponding concentrations were established, and mixed together and precipitated at warm with NH_4 in a weak excess After the precipitation the resulted oxidic compounds were filtred, washed with distilled water, and dried In order to stabilize the structure, the samples were calcined at the temperature of 873 K, and for the elimination of the crystallization water the samples were dried at 533 K for 5—6 hours Finally, the samples were pressed in pellets, sintered at the temperature of 1,123 K for 7 hours and slowly cooled down.

The temperature dependence of the magnetic susceptibility for the investigated samples in the temperature range 100—1,100 K and in the magnetic field of 9,500 G intensity was carried out using a Weiss—Forrer equipment with 10^{-8} cm³/g sensitivity [2].

* *University of Cluj-Napoca, Faculty of Mathematics and Physics, 3100 Cluj-Napoca, Romania*

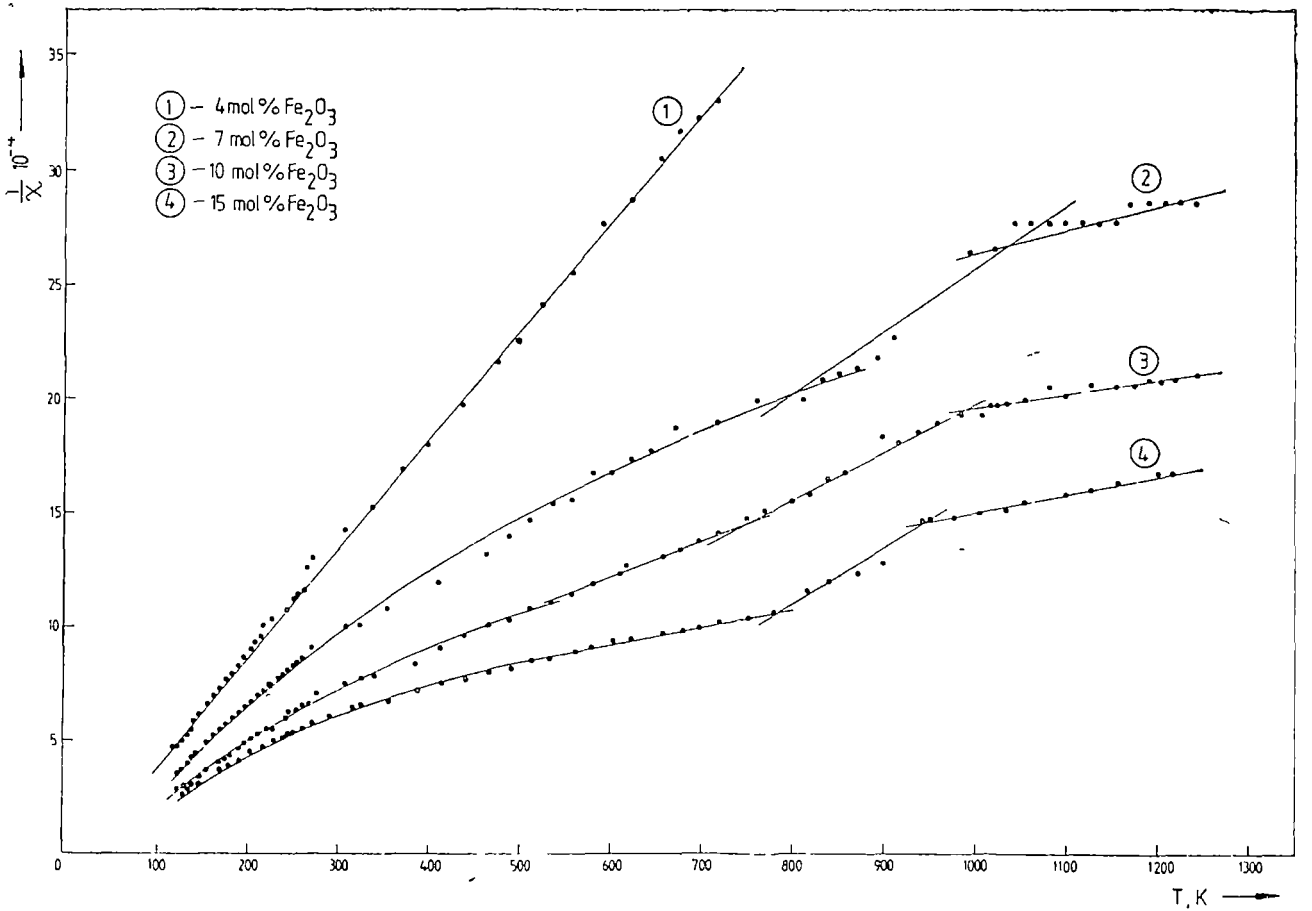

Fig 1 Temperature dependence of the reciprocal magnetic susceptibility

3 Experimental results and discussion. The temperature dependence of the reciprocal magnetic susceptibility for the α-(Al_2O_3—Fe_2O_3) samples with the concentration of 4, 7, 10 and 15 mol % of α-Fe_2O_3 is given in Fig 1.

As one can see from this figure the reciprocal magnetic susceptibility versus temperature changes very unusually, except the case for the sample with the concentration of 4 mol % α-Fe_2O_3 which is linear At lower temperatures the reciprocal magnetic susceptibility increases nonlinear with the temperature increase up to 450 K and then linear up to 780 K, when the slope of the lines changes, and at 960 K changes again The region with the step dependence of the reciprocal magnetic susceptibility versus temperature represents the transition region from the ordered magnetic state to paramagnetic state Actually, the temperature dependence of the reciprocal magnetic susceptibility curves consists in the superposition of the temperature dependence of the reciprocal magnetic susceptibility corresponding to the α-(Fe_2O_3—Al_2O_3) antiferromagnetic phase and α-(Al_2O_3—Fe_2O_3) paramagnetic phase, the system being biphasic This fact explains the nonlinear dependence of the reciprocal magnetic susceptibility at low temperature and of course the step dependence at higher temperatures

For the solid solution with 4 mol % α-Fe_2O_3 the temperature dependence of the reciprocal magnetic susceptibility is linear obeing the Curie—Weiss law.

These results are filling the existent knowledge about the magnetic behaviour of the α-(Fe_2O_3—Al_2O_3) oxidic system, especially on the biphasic part of the equilibrium diagram [1], and allow to better understand the magnetic behaviour of the thernary system α-(Fe_2O_3—Al_2O_3—Cr_2O_3) investigated before [3]

REFERENCES

1. Liliana Pop, Camelia Maraloiu, Liviu Stănescu, Iuliu Pop, *Studia Universitatis Babeş-Bolyai, Physica*, **32** (1) (1987)
2 Iuliu Pop, V J Tchetchernikov *Priborî i Tchnika Experimenta*, **5**, 180 (1984)
3 Liliana Pop, Minerva Cristea, Olivia Pop, Iuliu Pop, *Lucrările Conferinţei anuale de semiconductoare*, Sinaia, 7—10 October, 1987, p 531.

STUDIA UNIV BABEŞ-BOLYAI, PHYSICA, XXXIII, 1, 1988

MPARAETRIC INSTABILITIES IN A TWO-COMPONENT HOMOGENEOUS COLD MAGNETIZED PLASMA

S. COLDEA* and J. KARÁCSONY*

Dedicated to Professor IOAN URSU on his 60 th anniversary

Received. March 23, 1988

ABSTRACT. — The parametric instabilities of a magnetized two-component cold plasma are studied in a left-hand polarized electric field and in a hybrid pump field by applying a multitime scale perturbation-based method The growth rates of instabilities are obtained for the dipole approximation

Introduction. The parametric instabilities were intensively studied [1—2] because of their applications in devices proposed for thermonuclear fusion, astrophysics and electronics. In this paper we will investigate parametric instabilities of a magnetized two-component plasma in an applied left-hand circularly polarized electric field and in a hybrid field, by using a method based on multitime scale perturbation previously used in the study of parametric instabilities of a magnetized plasma in a right-hand polarized electric field, with ions dynamics [3]

The plasma in a left-hand polarized electric field. For the externally applied fields of the form

$$\vec{E}^{(0)}_{\text{ext}} = \text{Re}\,\{E_0(\hat{e}_2 - i\hat{e}_3) \quad \exp\,(i(k_0x - w_0t))\} \tag{1.a}$$

$$\vec{B}_{\text{ext}} = B_0 \quad \hat{e}_1 \tag{1 b}$$

where $\hat{e}_1$, $\hat{e}_2$ and $\hat{e}_3$ are the unit vectors along the rectangular Cartesian axes, and where w_0 and k_0 satisfy the following dispersion relation [3]:

$$c^2k_0^2 - w_0^2 + \sum_{n=1}^{2} \frac{w_0 w_{pn}^2}{w_0 - \Omega_{nc}} \tag{2}$$

where w_{pn} are the characteristic plasma frequencies

$$w_{pn}^2 = 4\pi n_0 e_n^2/m_n \tag{3}$$

and

$$\Omega_{nc} = e_n B_0/cm_n \tag{4}$$

are the corresponding cyclotron frequencies.

* *University of Cluj-Napoca, Faculty of Mathematics and Physics, 3100 Cluj-Napoca, Romania*

The velocities due to the external fields and the zero order external current are different from those given for a right hand polarized pump field [3]:

$$\vec{v}_n^{(0)} = a_n(\hat{e}_2 \sin(w_0 t) + \hat{e}_3 \cdot \cos(w_0 t)) + a_n(\hat{e}_2 \sin \Omega_{nc} t + \hat{e}_3 \cdot \cos \Omega_{nc} t) = \vec{v}_n^{(0)w_0} + \vec{v}_n^{(0)\Omega_{nc}} \tag{5}$$

where

$$a_n = \frac{e_n}{m_n c}\left(\frac{E_0}{w_0 - \Omega_{nc}}\right) \tag{6}$$

and

$$-4\pi \vec{j}_{\text{ext}}^{(0)} = E_0\left(-w_0 + \sum_n \frac{w_{pn}^2}{w_0 - \Omega_{nc}}\right) \times (\hat{e}_2 \cdot \sin w_0 t + \hat{e}_3 \cos w_0 t) +$$

$$+ E_0 \sum_n \frac{w_{pn}^2}{w_0 - \Omega_{nc}} (\hat{e}_2 \cdot \sin \Omega_{nc} t + \hat{e}_3 \cos \Omega_{nc} t) = \tag{6'}$$

$$= -4\pi \vec{j}_{\text{ext}}^{(0)w_0} - 4\pi \sum_n \vec{j}_{\text{ext}}^{(0)\Omega_{nc}} \tag{6''}$$

The assumption that a_n are small quantities was made throughout our investigation. Due to this fact, when the method of many-time scale perturbation is applied to cold plasma equations of motion and Maxwell equations, only the first order equations are different from those obtained in [3].

After a perturbation expansion of the longitudinal and transverse equations, because we are interested in the propagation of the response parallel to the external magnetic field, we arrived at the following relations:

$$\left(\frac{\partial^2}{\partial t^2} + w_p^2\right)(E_L)_1 = -\frac{i}{2}\sum_n w_{pn}^2 \, k a_n \left\{ [e^{-iw_0 t} + e^{-i\Omega_{nc} t}] \cdot \left(\xi_-^- \frac{e^{-iw_k^- t}}{w_k^-} - \xi_-^+ \frac{e^{iw_k^+ t}}{w_k^+}\right) - \right.$$

$$\left. - (e^{iw_0 t} + e^{i\Omega_{nc} t}) \left[\xi_+^- \frac{e^{-iw_k^+}}{w_k^+} - \xi_+^+ \frac{e^{iw_k^- t}}{w_k^-}\right]\right\} - 2iw_p \left[\frac{\partial \xi_L^+}{\partial(\varepsilon t)} e^{iw_p t} - \frac{\partial \xi_L^-}{\partial(\varepsilon t)} \cdot e^{-iw_p t}\right] \tag{7}$$

$$\left\{\left(\frac{\partial}{\partial t} \pm i\Omega_{1c}\right)\left(\frac{\partial}{\partial t} + i\Omega_{2c}\right)\left(\frac{\partial^2}{\partial t^2} + w_k^2\right) \mp i\left[w_{p1}^2 \, \Omega_{1c}\left(\frac{\partial}{\partial t} \pm i\Omega_{2c}\right) + \right.\right.$$

$$\left.\left. + w_{p2}^2 \, \Omega_{2c}\left(\frac{\partial}{\partial t} \pm i\Omega_{1c}\right)\right]\right\}(E^{\pm}) =$$

$$= \pm\left(\frac{\partial}{\partial t} \pm i\Omega_{2c}\right) w_{p1}^2 \, \Omega_{1c} \frac{\partial}{\partial(\varepsilon t)}\left[\frac{\xi_{\pm}^- e^{-iw_k^{\pm} t}}{w_k^{\pm} \mp \Omega_{1c}} + \frac{\xi_{\pm}^+ e^{iw_k^{\pm} t}}{-w_k^{\mp} \mp \Omega_1}\right] \pm$$

$$\pm\left(\frac{\partial}{\partial t} \pm i\Omega_{1c}\right) w_{p2}^2 \, \Omega_{2c} \frac{\partial}{\partial(\varepsilon t)}\left[\frac{\xi_{\pm}^- e^{-iw_k^{\pm} t}}{w_k^{\pm} \pm \Omega_{2c}} + \frac{\xi_{\pm}^+ e^{iw_k^{\pm} t}}{-w_k^{\mp} \mp \Omega_2}\right] - \tag{8}-(9)$$

$$- 2\frac{\partial}{\partial t}\left(\frac{\partial}{\partial t} \pm i\Omega_{1c}\right)\left(\frac{\partial}{\partial t} \pm i\Omega_{2c}\right)\frac{\partial}{\partial(\varepsilon t)}\left[\xi_+^- e^{-iw_k^{\pm} t} + \xi_{\pm}^+ e^{iw_k^{\pm} t}\right] \pm$$

$$\pm \frac{\partial}{\partial t}\left(\frac{\partial}{\partial t} \pm i\Omega_{1c}\right)\left(\frac{\partial}{\partial t} \pm i\Omega_{2c}\right) \sum_n \frac{k w_{pn}^2}{w_p^2} \left[\xi_L^+ e^{iw_p t} + \xi_L^- e^{-iw_p t}\right] a_i (e^{\mp iw_0 t} + e^{\mp i\Omega_{nc} t})$$

where the spatial dependece $\exp(ik_z)$ was assumed and

$$E^{\pm} = E_{Tv} \pm iE_{TZ} \tag{10}$$

$$(E_L)_0 = \xi_L^+ \exp(iw_p t) + \xi_L^- \exp(-iw_p t) \tag{11}$$

$$w_p^2 = w_{p1}^2 + w_{p2}^2 \tag{12}$$

$$w_k^2 = c^2 k^2 + w_p^2 \tag{13}$$

$$(E^{\pm})_0 = \xi_{\pm}^- \exp(-iw_k^{\pm} t) + \xi_{\pm}^+ \exp(iw_k^{\mp} t) \tag{14}-(15)$$

and

$$w_k^{\pm 2} = w_k^2 + \sum_n \frac{w_{pn}^2 \Omega_{nc}}{\pm w_k^{\pm} - \Omega_{nc}} \tag{16}-(17)$$

After secularities eliminations, the autonomous pairs of differential equations give us the following results

2.1. When $w_k^+ + w_p = w_0$, the elliptically polarized right-hand response may be excited with a maximum growth rate given by

$$\lambda_{\max} = \frac{k}{2} \frac{\left| \sum_n w_{pn}^2 a_n \right|}{w_p^{3/2} \left[2w_k^+ + \sum_n \frac{w_{pn}^2 \Omega_{nc}}{w_k^+ - \Omega_{nc}} \right]^{1/2}} = \tag{18a}$$

$$= \frac{ekE_0}{2m_1 |w_0 + \Omega|} \left\{ \frac{w_{p1}}{2w_k^+ - \frac{w_{p1}^2 \Omega}{(w_k^+ - \Omega)^2}} \right\}^{1/2} \tag{18b}$$

where the assumption that electrons dominate in $\sum_n$ was made On the other hand in writting Eqs. (18) was introduced the notation

$$\Omega_{1c} = -\Omega \qquad (\Omega > 0) \tag{19}$$

2.2. For $w_k^- + \Omega_{1c} = -w_p$, the elliptically left-hand polarized response becomes unstable, having the maximum growth rate of the following form

$$\lambda_{\max} = \frac{k}{2} \frac{w_{p1}^2 |a_1|}{w_p^{3/2} \left[2w_k^- - \sum_n \frac{w_{pn}^2 \Omega_{nc}}{(w_k^- - \Omega)^2} \right]^{1/2}} = \tag{20a}$$

$$= \frac{ekE_0}{2m_1 |w_0 + \Omega|} \left\{ \frac{w_{p1}}{2w_k^- + \frac{w_{p1}^2 \Omega}{(w_k^- - \Omega)^2}} \right\}^{1/2} \tag{20b}$$

2.3 When $w_k^+ - \Omega_{2c} = -w_p$, the growth rate of the elliptically right-hand response is obtained as:

$$\lambda_{\max} = \frac{k}{2} \frac{w_{p2}^2 |a_2|}{w_p^{3/2} \left[2w_k^+ - \sum_n \frac{w_{pn}^2 \Omega_{nc}}{w_k^+ - \Omega_{nc})^2} \right]^{1/2}} = \tag{21a}$$

$$= \frac{ekE_0}{m_2 \left| w_0 - \frac{m_1}{m_2} \Omega \right|} \left\{ \frac{w_0}{2w_k^+ - \frac{w_0 \Omega}{(w_k^+ + \Omega)^2}} \right\}^{1/2} \tag{21b}$$

The plasma in a hybrid pump field. For an electric field of the form

$$\vec{E}_{\text{ext}}^{(0)} = \text{Re}\{E_0 \cdot \exp(i(\vec{k}_0 \cdot \vec{x} - w_0 t)\hat{e}_3\} \tag{22a}$$

with

$$\vec{k}_0 = \hat{e}_2 k_{0y} + \hat{e}_3 k_{0z} \tag{22b}$$

and a magnetic field of the form

$$\vec{B}_{\text{ext}} = B_0 \cdot \hat{e}_1 \tag{22c}$$

w_0 and k_0 are related through the dispersion equation of the form:

$$\left[w_0^2 - c^2 k_0^2 - \sum_n \frac{w_{pn}^2 w_0^2}{w_0^2 - \Omega_{nc}^2} \right] \left[w_0^2 - \sum_n \frac{w_{pn}^2 w_0^2}{w_0^2 - \Omega_{nc}^2} \right] - w_0^2 \left[\sum_n \frac{w_{pn}^2 \Omega_{nc}}{w_0^2 - \Omega_{nc}^2} \right]^2 = 0 \tag{23}$$

In an analogous manner with the previous case of the plasma in a left-hand polarized circularly pump field, in this case we arrived at the following results:

3.1. When $w_k^+ + w_p = w_0$, the right-hand elliptically polarized response becomes unstable, with maximum growth rate.

$$\lambda_{\max} = \frac{k}{2} \sum_n w_{pn}^2 |b_n| \left\{ \frac{\Omega_{nc}}{2w_0} + \frac{1}{2} \right\} \frac{1}{w_p^{3/2} \left[2w_k^+ + \sum_n \frac{w_{pn}^2 \Omega_{nc}}{(w_k^- - \Omega_{nc})^2} \right]^{1/2}} =$$

$$= \frac{ekE_0 w_0}{2m_1 |w_0^2 - \Omega^2|} \left(\frac{1}{2} - \frac{\Omega}{2w_0} \right) \left\{ \frac{w_c}{2w_k^+ - \frac{w_c^2 \Omega}{(w_k^+ + \Omega)^2}} \right\}^{1/2} \tag{24}$$

where

$$b_n = \frac{e_n}{m_n} w_0 \left[\frac{E_0}{w_0^2 - \Omega_{nc}^2} \right] \tag{25}$$

3.2. When the frequency matching $w_k^- + w_p = w_0$ is fulfilled, the maximum growth rate of the left-hand response is obtained as:

$$\lambda_{\max} = \frac{k}{2} \sum_n \frac{w_{pn}^2 |b_n| \left[-\frac{\Omega_{nc}}{2w_0} + \frac{1}{2} \right]}{w_p^{3/2} \left[2w_k^- - \sum_n \frac{w_{pn}^2 \Omega_{nc}}{(w_k^- + \Omega_{nc})^2} \right]^{1/2}} = \tag{26a}$$

$$= \frac{k}{2} \frac{e}{m} \left[\frac{w_0 E_0}{w_0^2 - \Omega^2} \right] \left(\frac{1}{2} + \frac{\Omega}{2w_0} \right) \left\{ \frac{w_c}{2w_k^- + w_c^2 \Omega/(w_k^- - \Omega)^2} \right\}^{1/2} \tag{26b}$$

3 3. When $w_k^- + \Omega_k = -w_p$, the left-hand polarized response becomes unstable with the maximum growth rate obtained, of the form

$$\lambda_{\max} = \frac{k}{2} \frac{|b_1| w_c^{1/2}}{\left[2w_k^- + \frac{w_c^2 \Omega}{(w_k^- - \Omega)^2} \right]^{1/2}} \tag{27}$$

3.4. Finally, for the condition $w_k^+ - \Omega_{2c} = -w_p$, the maximum growth rate of the right-hand elliptically polarized response is the following

$$\lambda_{\max} = \frac{ekE_0 w_0}{m_2 \left| w_0^2 - \left(\frac{m_1}{m_2} \right)^2 \Omega^2 \right|} \left[\frac{w_1}{2w_k^+ - \frac{w_1^2 \Omega}{(w_k^+ + \Omega)^2}} \right]^{1/2} \tag{28}$$

Conclusions. Our analysis is acceptable only if the spatial variation of the pump fields can be neglected with respect to the response fields, i e. for the following conditions of the so-called dipole approximation:

$$k_0^2, \; K^2 > 0 \tag{29}$$

$$k_0^2/k^2 \ll 1 \tag{30}$$

The condition (29) is fulfilled for the case of a left-hand polarized field when we have

$$w_k^+ > w_p, \; \left(\frac{m_1}{m_2} \right) \Omega < w_k^+, \; \Omega > w_k^+ + w_p \tag{31}$$

$$w_k^+ < w_p; \; \left(\frac{m_1}{m_2} \right) \Omega < w_k^+; \; \Omega > \max \left\{ w_{k_i}^+ + w_p, \; \frac{w_{p1}^2 - w_k^{+2}}{w_k^+} \right\} \tag{32}$$

A comparison of k_0^2 from the equation (2) with k^2 from equation (16) gives us the following condition for (30)

$$\sum_n \frac{w_{pn}^2}{w_0(w_0 - \Omega_{nc})} \gg 2 \frac{w_p}{w_0} + \sum_n \frac{w_{pn}^2 \Omega_{nc}}{w_0^2 (w_0 - w_p - \Omega_{nc})} \tag{33}$$

For the case $w_0 > w_{pi}$ the inequality (33) is not fulfilled, result which is in accordance with the previously obtained results from the condition (2) [4].

In the case of a left-hand elliptically polarized field, instead of (31) and (32), the conditions

$$w_0 > \frac{1}{2}\{-\Omega + \sqrt{\Omega^2 + 4w_{p1}^2}\} \tag{34a}$$

$$\Omega > 3w_{p1} \tag{34b}$$

ensure the validity of equation (29)

The approximation done by the inequalities (30) is satisfied when we have

$$\frac{w_0^2}{\Omega^2} - \frac{w_1^2}{\Omega(w_0 + \Omega)} \ll 1 - \frac{w_1}{\Omega} \tag{35}$$

As results by comparing our equation (20) with the relation (31) from [3], the growth rate of the left-hand elliptically polarized response arround the frequency $(\Omega - w_p)$ is, in the left-hand polarized pump field, smaller than in the right-hand polarized pump field. Our result is in accordance with those obtained in [4], [5] and [6]

Finally, in the case when $w_k^- + \Omega_{1c} = -w_p$, the conditions for dipole approximation are the following

$$w_0 > \max\left\{\frac{m_1}{m_2}\Omega\,,\ \frac{1}{2}\left[-\Omega + \sqrt{\Omega^2 + 4w_p^2}\right]\right\} \tag{36}$$

or

$$w_0 < \min\left\{\frac{m_1}{m_2}\Omega\,,\ \frac{1}{2}\left[-\Omega + \sqrt{\Omega^2 + 4w_p^2}\right]\right\} \tag{37}$$

and

$$\frac{w_0}{\Omega}\left[\frac{w_0}{\Omega} - \frac{w_1^2}{\Omega(w_0 + \Omega)}\right] \ll \frac{w_1^2\,\Omega}{\Omega^2(\Omega - w_1)} - 2w_1\frac{m_1}{m_2}\Omega^{-1} \tag{38}$$

As results by comparing our equation (21) with equation (34) from [3], the growth rate of the right-hand elliptically polarized response around the frequency $((m_1/m_2)\cdot\Omega - w_p)$ is greater in the left-hand ploarized pump field than in the right-hand polarized field, in accordance with the previous result obtained in [5] and [4].

In a similar manner the conditions for dipole approximation can be deduced for the case of a hybrid pump field These conditions have the following form for the case under discussion:

$$\Omega < \min\left\{\frac{w_0^2 - w_p^2}{w_0}\,,\ \sqrt{w_0^2 - w_p^2}\,,\ w_0\right\} \tag{39}$$

or

$$\max\left\{\frac{w_0^2 - w_p^2}{w_0}\,,\ \sqrt{w_0^2 - w_p^2}\right\} < \Omega < w_0 \tag{40}$$

and

$$-\frac{\left(\frac{w_1\Omega}{w_0^2-\Omega^2}\right)^2}{w_0^2-\frac{w_1^2 w_0^2}{w_0^2-\Omega^2}}-\frac{w_1^2}{w_0^2-\Omega^2}\ll -2\frac{w_1}{w_0}+\frac{w_1^2\Omega}{w_0^2(w_0-w_1+\Omega)} \tag{41}$$

$$-\frac{\left(\frac{w_1^2\Omega}{w_0^2-\Omega^2}\right)^2}{w_0^2-\frac{w_1^2 w_0^2}{w_0^2-\Omega^2}}-\frac{w_1^2}{w_0^2-\Omega^2}-2\frac{w_1}{w_0}-\frac{w_1^2\Omega}{w_0^2(w_0-w_1-\Omega)} \tag{42}$$

$$\frac{w_0^2}{\Omega^2}\left[1-\frac{w_p^4\Omega^2}{(w_0^2-\Omega^2)(w_0^4-w_0^2\Omega^2-w_1^2w_0^2)}\right]\frac{w_1^2}{w_0^2-\Omega^2}\ll 1-\frac{w_0}{\Omega} \tag{43}$$

$$\frac{w_0^2}{\Omega^2}\left[1-\frac{w_1^4\Omega^2}{(w_0^2-\Omega^2)(w_0^4-w_0^2\Omega^2-w_1^2w_0^2)}-\frac{w_1^2}{w_0^2-\Omega^2}\right]\ll\frac{w_1^2}{\Omega(\Omega-w_1)}-2\frac{m_1}{m_2}\frac{w_1}{\Omega} \tag{44}$$

Eqs. (39) and (40) assure that $k_0^2>0$ The conditions for $k^2>0$ are the same with those given in the case of left-hand polarized pump field.

In each case parametric instabilities appear due to coupling of different modes The coupling appears between longitudinal mode and the right- or left-hand polarized responses For the left-hand polarized pump field there is a coupling only between the longitudinal mode and the left-hand polarized response, as well in weak as in strong external magnetic fields. For the hybrid pump field there are couplings between all modes, for all values of externally applied magnetic field.

REFERENCES

1 C. S Liu, Y. K Tripathi, *Phys. Reports*, **143** (1986).
2. M. Porkolab, *Nuclear Fusion*, **18**, 367 (1978)
3. R. Prasad, *J. Plasma Phys.*, **5**, 291 (1971).
4 R Prasad, *Phys Fluids*, **14**, 1310 (1970)
5 C. Băleanu, *Bull Math Soc Sci Math R S R Roumanie*, **22**, 245 (1970); 339 (1978).
6. C Băleanu, „Probleme actuale de fizică", Ed Universitatea din Cluj-Napoca, Vol. II, 90 (1982)
7. C. Băleanu, „Probleme actuale de fizică", Ed Universitatea din Cluj-Napoca, vol III, 81 (1983).

STUDIA UNIV BABEŞ-BOLYAI, PHYSICA, XXXIII, 1, 1988

MAGNETIC BEHAVIOUR OF SOME MOLIBDENUM — SODA — PHOSPHATE OXIDE GLASSES

I. ARDELEAN*, GH. ILONCA*, O. COZAR* and S. FILIMON*

Dedicated to Professor IOAN URSU on his 60 th anniversary

Received: February 16, 1988

ABSTRACT. — The magnetic susceptibility measurements have been performed on $xMoO_2 \cdot (1-x)[2P_2O_5 \cdot Na_2O]$ glasses with $5 \leqslant x \leqslant 50$ mol % These data suggest that all along the concentration range the molibdenum ions are in majority as magnetic isolated species From Curie constant and atomic magnetic moment values we have assumed that in these glasses the molibdenum ions are predominant as Mo^{6+}, Mo^{5+} and Mo^{4+} valence states.

Introduction. In the past few years there have been many reports on investigations of the valence states and distribution mode of the transition metal ions in the network of the oxide glasses [1—7] Up to now, the EPR [7—10] studies of the oxide glasses with molibdenum ions suggest the presence of Mo^{5+} ions, which may be magnetically isolated or coupled with mixed exchange pairs formation.

In order to obtain further information on the molibdenum ions in oxide glasses, this paper will report results of magnetic susceptibility investigations of molibdenum—soda—phosphate oxide glasses.

Experimental. We have studied the $xMoO_2$ $(1-x)[2P_2O_5$ $Na_2O]$ glasses with $5 \leqslant x \leqslant 50$ mol%, maintaining the P_2O_5/Na_2O ratio constant, that is keeping the matrix structure unmodified In this way, initially the glass matrix $2P_2O_5—Na_2O$ was prepared by mixing $NH_4H_2PO_4$ and Na_2CO_3 and melting this admixture in a sintered corundum crucible We used the technique previously reported [11] After cooling, the host glass was crushed and the resulting powder was mixed with appropriate amounts of MoO_2, before final melting at $T_M = 850°C$ for 0 5 h. The molten glass was poured onto a stainless-steel plate The structure of these glasses has been studied by X-ray diffraction analysis and did not reveal any crystalline phase up to 50 mol% MoO_2.

The magnetic susceptibility data were performed using a Faraday type balance in the temperature range 80 to 300 K

Results and discussion. The temperature dependence of the reciprocal magnetic susceptibility of the various glasses from this system is presented in Fig. 1. For these glasses, in all concentration range of molibdenum ions, a Curie law is observed This suggests that the predominant part of molibdenum ions are isolated and that no magnetic order is present This behaviour agrees with the EPR study conclusions [12].

The concentration dependence, of the magnetic susceptibility at $T = 200$ K is presented in Fig 2. This dependence shows a maximum at $x \simeq 40$ mol % MoO_2.

* University of Cluj-Napoca, Faculty of Mathematics and Physics, 3100 Cluj-Napoca, Romania

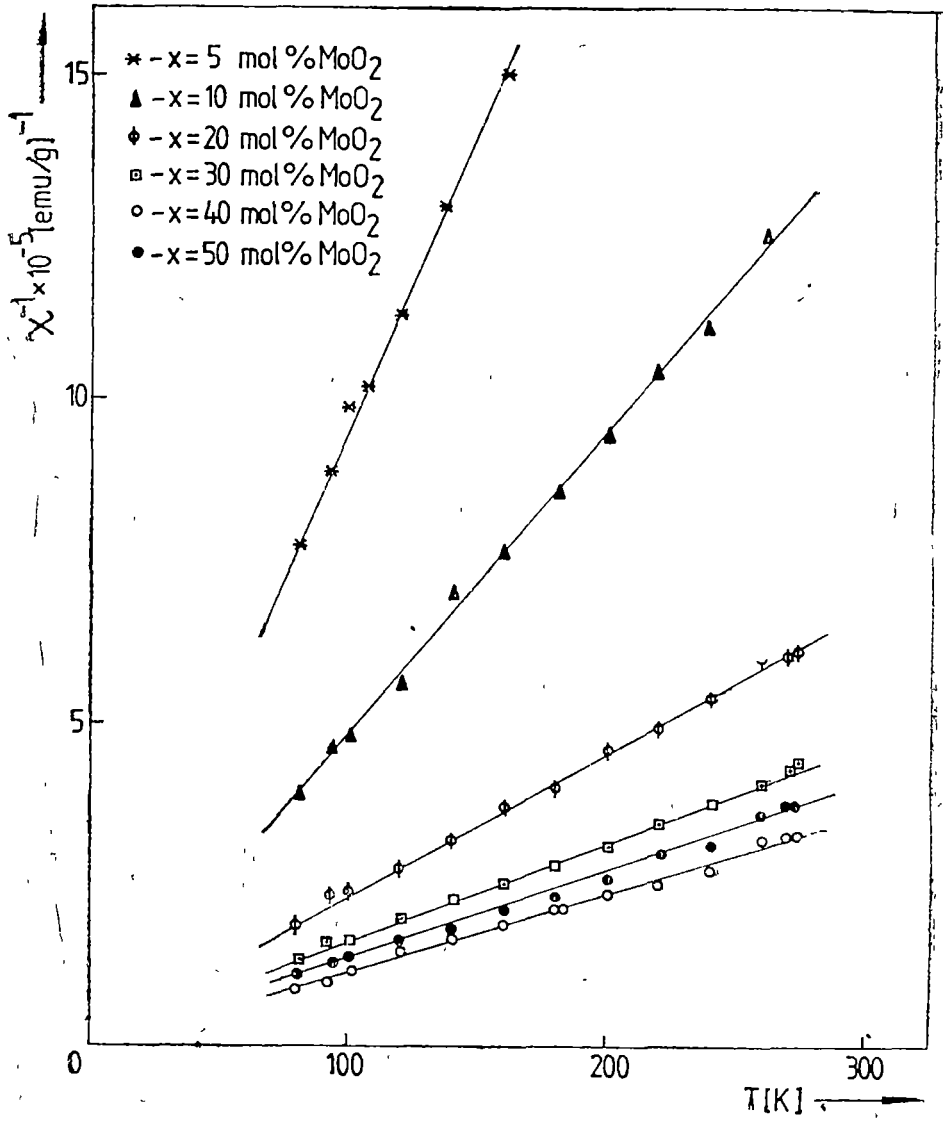

Fig 1. The temperature dependence of the reciprocal magnetic susceptibility.

To determine accurately the values of the Curie constants, C_M, and atomic magnetic moments, μ_{at}, a correction due to the diamagnetism of the glass matrix and MoO_2 was taken into account. The composition dependence of the Curie constants, C_M, is presented in Fig 3 The values of the Curie constant, which is proportional to the paramagnetic ions concentration, increase with

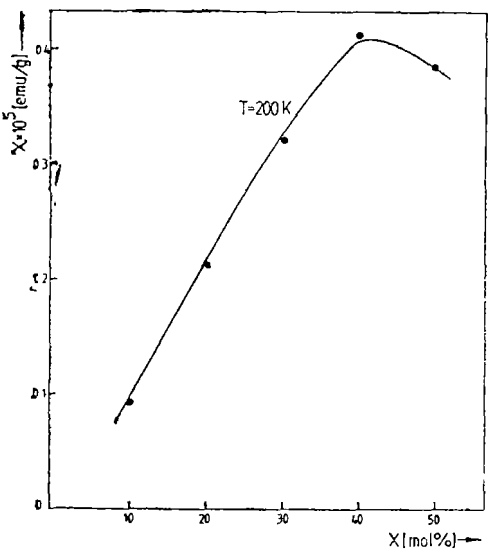

Fig 2 The composition dependence of the magnetic susceptibility at $T = 200$ K

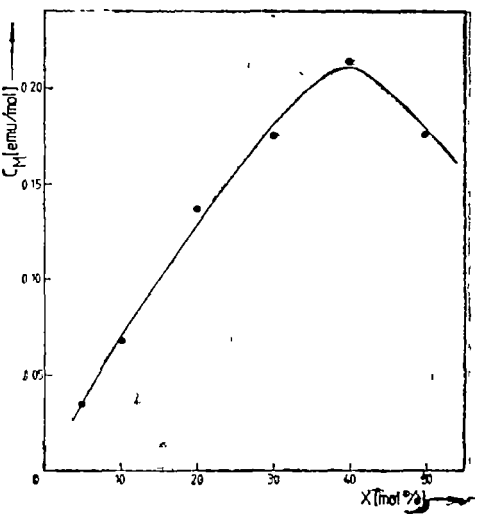

Fig 3 The composition dependence of the Curie constant

molibdenum ions concentration up to $\simeq$ 40 mol % MoO_2 About this concentration the Curie constant decreases Having in view that the Curie constant is

$$C = \frac{N \mu_{ef}^2}{3K} \tag{1}$$

it results that this depends on the square of the effective magnetic moment. In relation (1), N is the number of transition metal ions in unit volume, K — the Boltzmann constant and μ_{ef} — effective magnetic moment. The experimental values of Curie constants and of the atomic magnetic moments obtained for these glasses are smaller than those which correspond to MoO_2 content, considering that all molibdenum ions are in Mo^{4+} valence states ($\mu_{Mo^{4+}} = 2.83\ \mu_B$) In this way, we consider that Mo^{6+}, Mo^{5+}, Mo^{4+} and Mo^{3+} ions are present in the studied glasses The presence of the Mo^{5+} ions ($\mu_{Mo^{5+}} = 1.73\ \mu_B$) have been evidenced by EPR measurements [12] From optical absorption spectra, it results that the Mo^{3+} ions ($\mu_{Mo^{3+}} = 3.87\ \mu_B$) are present in small proportion in these glasses. Thus their contribution to the Curie constant values is also small Because the Mo^{6+} ions are diamagnetic, it follows that the presence of these ions may lead to the decreasing of the Curie constant value, in the studied glasses This is true since the Curie constant is proportional to the paramagnetic ions concentration From the Curie constant experimental values, it results that in the case of the sample with x = 50 mol % MoO_2, the molibdenum ions are present as Mo^{6+} and Mo^{5+} valence states.

Conclusions. By means of the magnetic susceptibility investigations of $xMoO_2$ $(1-x)[2P_2O_5 \cdot Na_2O]$ glasses with $5 \leqslant x \leqslant 50$ mol % we have obtained information concerning the molibdenum ions distribution in the soda-phosphate glass matrix which explains their magnetic behaviour.

Magnetic properties of $xMoO_2 \cdot (1-x)[2P_2O_5\ Na_2O]$ glasses depend on the MoO_2 content These data also suggest that all along the concentration range the molibdenum ions are present as magnetic isolated species.

From Curie constant and atomic magnetic moment values, it results that in these glasses the molibdenum ions are prevailing as Mo^{6+}, Mo^{5+} and Mo^{4+} valence states.

REFERENCES

1. E Burzo, I Ardelean and I Ursu, *J Mater Sci*, **15**, 581 (1980)
2. I Ursu, E Burzo, D Ungur and I Ardelean, *Rev. Roum Phys*, **26**, 801 (1981).
3. E Burzo, I Ursu, D Ungur, I Ardelean and V M Nazarov, *J Appl. Phys*, **58**, 3628 (1985).
4. O. Cozar, I Ardelean and Gh Ilonca, *Solid State Commun*, **44**, 809 (1982).
5. S Simon and Al Nicula, *J Non-Crystal Solids*, **57**, 23 (1983).
6. I. Ardelean, O Cozar and Gh Ilonca, *J Non-Crystal Solids*, **68**, 33 (1984)
7. Gh Ilonca, I Ardelean and O Cozar, *J Magnetism and Magnetic Mat*, **54–57**, 223 (1986)
8. G F Lynch and M Sayer, *J Phys C Solid State Phys*, **6**, 3661 (1973)
9. O. Cozar, A Goldstein, I Ardelean, in. „Progrese în fizică", ICEFIZ, Iaşi, 3–5 oct. 1985, p 418
10. O. Cozar, I Ardelean, Gh Ilonca and A Goldstein, *Proceedings of the Symposium* on „Methods, Models and Techniques in Physics and Related Fields", Cluj-Napoca, sept. 26–27, 1986, p. 71
11. O Cozar, I Ardelean, Gh Ilonca, *Proceedings of the XXIII Congress AMPERE on Magnetic Resonance* (B Maraviglia, F De Luca and R Compenella eds), Instituto Superiore di Sanita, Roma, September 15–19, 1986, p 248
12. O. Cozar, I Ardelean and Gh Ilonca, to be published.

STUDIA UNIV BABEŞ-BOLYAI, PHYSICA, XXXIII, 1, 1988

ROTATIONAL EXCITATION OF NH_3 IN COLLISIONS WITH He

T. A. BEU* and M. VASIU*

Dedicated to Professor IOAN URSU on his 60th anniversary

Received, March 7, 1988

ABSTRACT. — Integral cross sections for the rotational excitation of NH_3 in collisions with He are computed NH_3 is treated as a rigid rotor and a recent potential energy surface for the NH_3—He interaction [5] is employed The cross section calculations have been carried out within the framework of the quantal coupled states approximation, and the results obtained at the relative kinetic energy $E = 97{,}7$ meV are in fair agreement with those available in the literature

1. **Introduction.** Rotational energy transfer of ammonia molecules in collisions with He have attracted great interest in the last decade, because of the importance of the radio frequency observations of interstellar ammonia [1]. Quantitative collisional rates for the rotational excitation of NH_3 in collisions with H_2 and He are needed for the interpretation of the line intensities. Extensive calculations for NH_3—He have been performed employing several calculated interaction potentials [2]—[5].

In the present work we use the potential energy surface (PES) presented in [5] and develop an original numerical strategy for the solution of the scattering problem. The construction of the above mentioned PES is described in Sec. 2. Details of the scattering calculations are presented in Sec. 3 Results and comparison with the results of [5] are given in Sec *4*.

2 **Potential Surface.** As already pointed out, our calculations are based on the PES derived in [5]

In order to describe the potential energy surface of the NH_3—He system, it is convenient to use a fixed axes coordinate system with the origin located at the center-of-mass of the ammonia molecule The z-axis coincides with the symmetry axis of the NH_3 molecule. The three H atoms are located in a plane perpendicular to the z axis. The triangle formed by the H atoms is rotated such that one hydrogen atom lies in the x-z plane. The position vector of the He atom is described relative to these body fixed axes (R is the distance from the origin, θ and Φ measure the angle from the z axis and the x—z plane, respectively)

The potential surface can now be expanded in terms of spherical harmonics, with the restriction that the potential has to be invariant under operations of the symmetry group C_{3v}, to which the ammonia molecule belongs:

$$V(R, \theta, \Phi) = \sum_{\substack{\lambda \geq \mu \geq 0 \\ \mu = 3n}} V_{\lambda\mu}(R)(1 + \delta_{\mu 0})^{-1}[Y_{\lambda\mu}(\theta, \Phi) + (-1)^{\mu} Y_{\lambda,-\mu}(\theta, \Phi)] \qquad (1)$$

* *University of Cluj-Napoca, Faculty of Mathematics and Physics, 3400 Cluj Napoca, Romania*

with

$$Y_{\lambda\mu}(\theta, \Phi) = (-1)^{\mu}\left[\frac{2\lambda+1}{4\pi}\frac{(\lambda-\mu)!}{(\lambda+\mu)!}\right]^{1/2} P_{\lambda}^{\mu}(\cos\theta)\exp(i\mu\Phi) \tag{2}$$

where P_{λ}^{μ} are unnormalized associated Legendre functions.

The interaction potential is partitioned into a Hartree—Fock energy contribution, which is obtained from large basis self-consistent-field (SCF) calculations, and a correlation energy contribution, which is approximated by a damped multipolar dispersion expansion [6]—[8]. Accordingly, the expansion coefficients $V_{\mu\lambda}(R)$ can be expressed as.

$$V_{\lambda\mu}(R) = V_{\lambda\mu}^{\mathrm{SCF}}(R) + f(R)V_{\lambda\mu}^{\mathrm{disp}}(R) \tag{3}$$

where the damping function has the form:

$$f(R) = \begin{cases} \exp\left[-\gamma(D/R-1)^2\right], & R \leqslant D \\ 1, & R > D \end{cases} \tag{4}$$

with $\gamma = 0.5$ and $D = 5\,3$ Å. Using the SCF potential energy values $V^{\mathrm{SCF}}(R_k, \theta_j, \Phi_i)$ tabulated in [5] for $R_k = (3, 4, \ldots, 8)\,a_0$, $\theta_j = 0, \pi/8, \ldots, \pi$, and $\Phi_i = 0, \pi/9, \ldots, \pi/3$, the coefficients $V_{\lambda\mu}^{\mathrm{SCF}}(R_k)$ may be obtained by solving for each R the system

$$V^{\mathrm{SCF}}(R_k, \theta_j, \Phi_i) = \sum_{\substack{\lambda \geqslant \mu \geqslant 0 \\ \mu = 3n}} V_{\lambda\mu}^{\mathrm{SCF}}(R_k)(1+\delta_{\mu 0})^{-1}\left[Y_{\lambda\mu}(\theta_j, \Phi_i) + (-1)^{\mu} Y_{\lambda,-\mu}(\theta_j, \Phi_i)\right] \tag{5}$$

In order to obtain the coefficients $V_{\lambda\mu}^{\mathrm{SCF}}(R)$ for distances greater than $8a_0$, we first extrapolated the pure SCF energies in the form

$$V^{\mathrm{SCF}}(R, \theta_j, \Phi_i) = -\left(\frac{A_{ij}}{R^6} + \frac{B_{ij}}{R^8}\right) \tag{6}$$

with A_{ij} and B_{ij} determined from the SCF values at 7 and $8a_0$.

The multipole expansion coefficients of the dispersion energy are explicitly given in [5] as

$$V_{\lambda\mu}^{\mathrm{disp}}(R) = -\sum_{n \geqslant 6} \frac{C_n^{\lambda\mu}}{R^n} \tag{7}$$

where the coefficients $C_n^{\lambda\mu}$ are related to the dipole polarizability and to the components of the dipole-quadrupole polarizability tensor

3. **Scattering Formalism.** The total Hamiltonian for the collision of a rigid rotor and an atom, in space-fixed coordinates located at the center-of-mass of the system can be written as follows

$$H = -\frac{\hbar^2}{2\mu_0}\nabla_R^2 + H_{\mathrm{rot}}(\hat{\Omega}) + V(R, \hat{\Omega}) \tag{8}$$

where μ_0 is the atom-molecule reduced mass, R is the collision coordinate from rotor center of mass to the atom. The rotor orientation is specified by $\hat{\Omega} = (\alpha\beta\gamma)$, the Euler angles that rotate the space-fixed axes into the body fixed, principal momentum of inertia axes of the molecule (used to expand the potential)

The rotor eigenfunctions are assumed known, and

$$H_{\text{rot}}(\Omega)|jkm\rangle = E_{jk}|jkm\rangle \tag{9}$$

where j, k and m are the total rotor momentum, and ist projection on the body fixed z′ axis and on the space-fixed z axis, respectively [9]

The ammonia molecule is a typical symmetric top, having a threefold axis of symmetry through the nitrogen. It is not, however, an ideal example of a rigid rotor, because it undergoes rapid inversions — large amplitude vibrations of the nitrogen through the plane of the hydrogen atoms. Since the vibrational period is about 50 ns and the duration of a thermal energy NH_3—He collision is less than 1 ns, the rigid rotor approximation may not be unreasonable [2].

The symmetric top eigenfunctions can be identified with matrix elements of the rotation operator

$$|jkm\rangle = \sqrt{\frac{2j+1}{8\pi^2}}\,\mathfrak{D}^j_{km}(\alpha\,\beta\,\gamma) \tag{10}$$

where $\mathfrak{D}^j_{km}(\alpha\gamma\beta)$ are matrix elements of the rotation operator [9]. The corresponding eigenvalues have the form

$$E_{jk} = B_j j(j+1) - B_k k^2 \tag{11}$$

It can be seen that $|jkm\rangle$ and $|j-km\rangle$ are eigenfunctions of H_{rot} corresponding to the same eigenvalue E_{jk}, so that any linear combination will also be a valid eigenfunction Proper symmetric top wavefunctions must also be eigenfunctions of the inversion operator, and the correct linear combinations are

$$|jk \in m\rangle = \frac{1}{\sqrt{2(1+\delta_{k0})}}\,(|jkm\rangle + \in |j-km\rangle) \tag{12}$$

where now $k \geqslant 0$, and $\in = \pm 1$, except for $k = 0$, when only $\in = +1$ is allowed.

Within the framework of the close coupling (CC) formulation one can form total angular momentum eigenfunctions

$$|JMjk \in l\rangle = \sum_{m_l} \langle jml m_l | JM\rangle\, |jk \in m\rangle\, |lm_l\rangle \tag{13}$$

where $|lm_l\rangle$ are spherical harmonics $Y_{lm_l}(\theta, \Phi)$ and $\langle j_1 m_1 j_2 m_2 | lm_l\rangle$ are Clebsch—Gordan vector coupling coefficients. The scattering wavefunction with total momentum J and projection M on the space-fixed z axis and appropriate to

the entrance channel $j k \in l$ can be expanded as

$$\psi^{JMjk\in l} = \sum_{j'k'\in'l'} \frac{1}{R} u^{JMjk\in l}_{j'k'\in'l'}(R) \,|\, JMj'k'\in'l'\rangle \tag{14}$$

Substituting this wavefunction into the time-independent Schrödinger equation for the scattering

$$[H - (E + E_{jk})]\psi^{JMjk\in l} = 0 \tag{15}$$

where E is the relative kinetic energy, gives the usual coupled equations for the radial functions

$$\left[\frac{d^2}{dR^2} - \frac{l(l+1)}{R^2} + K^2_{j'k'jk}\right] u^{JMjk\in l}_{j'k'\in'l'}(R) =$$

$$= \frac{2\mu_0}{\hbar^2} \sum_{j''k''\in''l''} \langle JMj''k''\in''l'' \,|V|\, JMj'k'\in'l'\rangle u^{JMjk\in l}_{j'k'\in'l'}(R) \tag{16}$$

with the wavenumber given by

$$K^2_{j'k'jk} = \frac{2\mu_0}{\hbar^2}(E + E_{jk} - E_{j'k'}) \tag{17}$$

The choice of the expansion set in (14) as total angular momentum eigenfunctions leads to a block diagonal potential matrix $\langle JMj''k''\in''l'' \,|V|\, JMj'k'\in'l'\rangle$. Consequently, each block of equation (16) may be solved independently for each J and M. This expresses the fact that the collision cannot induce transitions among total angular momentum states.

Further simplifications of the system (16) may be achieved within the framework of the coupled states (CS) approximation, which may be easily introduced using the CC formulation in a body-fixed coordinate system. Here, the operator of the orbital angular momentum, $\vec{l} = \vec{J} - \vec{j}$, is approximated by the operator of the total angular momentum $\vec{J}$. In other words, the CS approximation consists of neglecting the off-diagonal matrix elements of l^2 in the body-fixed frame, and further approximating the diagonal ones by $\hbar^2 J(J+1)$ The scattering wavefunction may be written.

$$\psi^{Jjk\in m} = \sum_{j'k'\in'} \frac{1}{R} u^{Jjk\in m}_{j'k'\in'm}(R) \,|\, j'k'\in'm\rangle \tag{18}$$

and the set of coupled equations for the radial functions takes the form.

$$\left[\frac{d^2}{dR^2} - \frac{J(J+1)}{R^2} + K^2_{j'k'jk}\right] u^{Jjk\in m}_{j'k'\in'}(R) = \tag{19}$$

$$= \frac{2\mu_0}{\hbar^2} \sum_{j''k''\in''} \langle j''k''\in''m \,|\, V \,|\, j'k'\in'm\rangle \, u^{Jjk\in m}_{j''k''\in''}(R)$$

As shown in [9], the potential matrix elements on the right-hand side of Eq. (19) have the form

$$\langle j'k'\in'm \,|V|\, jk\in m\rangle = \sum_{\lambda\mu} a^{j'k'\in'm}_{jk\in\lambda\mu} V_{\lambda\mu}(R) \tag{20}$$

The coefficients $a^{j'k'\in'm}_{jk\in\lambda\mu}$ are calculated taking into account Eqs. (3) — (7) and (12)

$$a^{j'k'\in'm}_{jk\in\lambda\mu} = \frac{(-1)^{m-k}[1+\in'\in(-1)^{j'+\lambda+j+\mu}]}{2(1+\delta_{\mu 0})}\sqrt{\frac{(2j'+1)(2\lambda+1)(2j+1)}{4\pi(1+\delta_{k'0})(1+\delta_{k0})}}\times$$

$$\times\begin{pmatrix} j' & \lambda & j \\ -m & 0 & m\end{pmatrix}\left\{\begin{pmatrix} j' & \lambda & j \\ -k' & \mu & k\end{pmatrix}+(-1)^{\mu}\begin{pmatrix} j' & \lambda & j \\ -k' & \mu & k\end{pmatrix}+\in\left[\begin{pmatrix} j' & \lambda & j \\ -k' & \mu & -k\end{pmatrix}+\right.\right. \quad (21)$$

$$\left.\left.+(-1)^{\mu}\begin{pmatrix} j' & \lambda & j \\ -k' & -\mu & -k\end{pmatrix}\right]\right\}$$

Equations (19) are solved subject to the following asymptotic conditions:

$$u^{Jjk\in m}_{j'k'\in'}(R) \sim \delta_{jj'}\,\delta_{kk'}\,\delta_{\in\in'}\exp[-i(K_{jkjk}\,R - J\pi/2)] -$$

$$-\left(\frac{K_{jkjk}}{K_{j'k'jk}}\right)^{1/2}\langle jk\in m\,|\,S^J\,|\,j'k'\in'm\rangle\exp\,[i(K_{j'k'jk}\,R - J\pi/2)] \quad (22)$$

State-to-state integral cross sections, summed over final and averaged over initial degeneracies, can be obtained from the S matrix as

$$\sigma(jk\in\to j'k'\in') = \sum_J (2J+1)\sigma^J(jk\in\to j'k'\in') \quad (23)$$

with

$$\sigma^J(jk\in\to j'k'\in') = \frac{\pi}{K^2_{jkjk}(2j+1)}\,|\delta_{jj'}\,\delta_{kk'}\,\delta_{\in\in'} - \langle jk\in m\,|S^J\,|j'k'\in'm\rangle|^2 \quad (23)$$

Because of permutational symmetry among the identical hydrogen nuclei in ammonia, the rotational levels can be divided into two sets, which are associated with different nuclear spin states and which interconvert at a negligible rate in thermal energy collisions Levels with $k = 3n$ are designated ortho-NH_3 and levels with $k = 3n \pm 1$ are designated para-NH_3 The CS scattering formalism predicts no transitions from one modification to the other, and this can be seen as follows: From the properties of the $3j$ symbols it is apparent that there are only nonvanishing potential matrix elements $\langle j'k'\in'm\,|V\,|jk\in m\rangle$ with either $\mu = \pm(k' - k)$ or $\mu = \pm(k' + k)$ On the other hand, the molecular symmetry ensures that the expansion of the intermolecular potential will contain only terms with $\mu = 3n$ Thus, both k' and k must be either of the form $3n$ (for ortho-NH_3), or fo the form $3n + 1$ (para-NH_3) Therefore, there will never be coupling between ortho- and paralevels and hence the scattering calculations can be done separately for the two species

The projection of the internal angular momentum onto the body-fixed z axis, m, is contained in the potential matrix only as a parameter The sets of equations involving different values of m are fully decoupled

4. **Results and Discussions.** We have computed state-to-state integral cross sections for the rotational scattering of ortho-NH_3 from He at 97 7 meV, case

for which there are 20 open channels (the ammonia molecule being initially in the ground state). The rotational energies yielded by Eq. (11) with $B_j = 1.23$ meV and $B_k = 0.45$ meV for those open channels are listed in Table I.

Table 1

Rotational energies (in meV) and calculated integral cross sections in Å² for the rotational transitions of ortho−NH_3 from the ground state to the state specified by j', k' and $\in'$.

j'	k'	$\in'$	$E_{j'k'jk}$	$\sigma(jk\in\to j'k'\in')$	
				Ref 5	this work
0	0	+	00 00	48 5780	42 4660
1	0	+	02 46	1 0114	0 9692
2	0	+	07.39	5.1576	6 6828
3	0	+	14 78	1.0281	1 0394
3	3	−	10 72	6 6806	5 5372
4	0	+	24 63	0 5053	0 4017
4	3	−	20 58	4 4772	4 3612
5	0	+	36 95	0 3829	0 3929
5	3	−	32.89	0 2212	0 1733
6	0	+	51 73	0 0615	0 0583
6	3	−	47 67	0 0201	0 0162
6	6	+	35 51	1 1538	1 1063
7	0	+	68 97	0 0012	0 0010
7	3	−	64 91	0 0125	0 0121
7	6	+	52 75	0 6220	0 5197
8	0	+	88 67	0 0002	0 0002
8	3	−	84 62	0 0000	0 0001
8	6	+	72 46	0 0153	0 0123
9	6	+	94.62	—	0 0000
9	9	−	74 35	—	0 0143

For the ortho-modification the ground state is characterized by the quantum numbers $j = 0$, $k = 0$, $\in = 1$, $m = 0$. From Eq. (21) it can be seen that the parity of the final state is $\in' = (-1)^{k'}$. Therefore in the scattering calculations the final states j', k', $\in' = (-1)^{k'}$, $m = 0$ have to be included, leading to the above-mentioned basis set of 20 open channels.

Some of the expansion coefficients $V_{\lambda\mu}$ of the spherical harmononics series (1) are presented in Fig 1 The $V_{\lambda\mu}$ coefficients have been obtained employing the procedure described in Sec 2 The interpolation of these coefficients has been accomplished using the Akima algorithm, which was found to work better than the cubic spline interpolation in what concerns the absence of oscillations.

The coupled equations of the scattering (19), subject to the asymptotic conditions (22), have been solved using an algorithm based on the method of Sams and Kouri [10]−[11] From the obtained scattering matrix S^J, state-to-state integral cross sections $\sigma^J(jk\in\to j'k'\in')$ for a certain total angular momentum J may be computed Fig 2 shows the J dependence for two such integral cross sections, $\sigma^J(00+\to 00+)$ and $\sigma^J(00+\to 10+)$. It should be noted the typical smooth behaviour of the elastic cross section $\sigma^J(00+\to 00+)$ for the ground state Total state-to-state rotational integral cross sections

$\sigma(jk\epsilon \rightarrow j'k'\epsilon')$ are listed in Table I, where they can be compared with the corresponding cross sections obtained in [5]. The two sets of cross sections are in fair agreement. Some discrepancies could be explained by the fact that

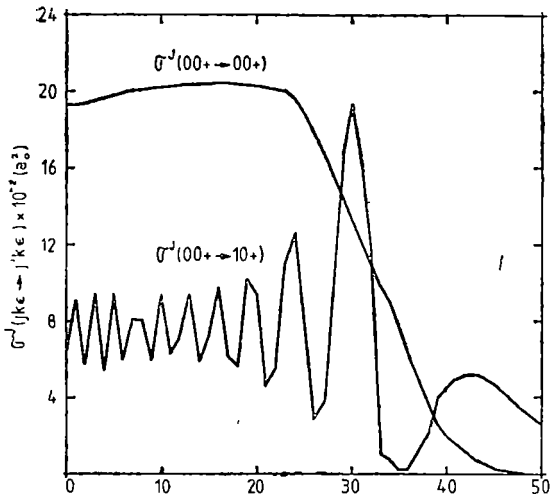

Fig 1. Expansion coefficients $V_{\lambda\mu}$ as defined in Eq. (3) vs internuclear distance

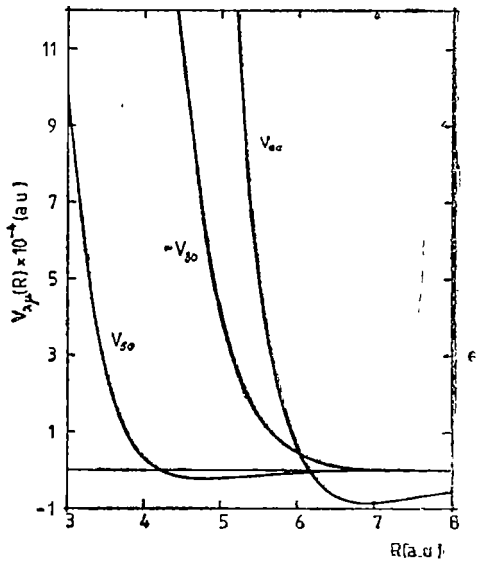

Fig 2 Total angular momentum dependence of the integral rotational cross sections $\sigma J(00^+\rightarrow 00^+)$ and $\sigma J(00^+\rightarrow 10^+)$.

we have included only 50 total angular momentum values J in our calculations, and consequently, some cross sections could probably not be fully converged.

The numerical calculations have been performed on a CORAL 4030 computer and the total CPU time required to obtain the results presented in Table I was about 75 hours Therefore, we investigate at present the possibility of using "cheeper" approximations in order to perform such molecular scattering calculations.

REFERENCES

1. T L Wilson and C. M Walmsley, in *Molecular Astrophysics*, (G H.F Diercksen, W. F Huebner and P W Langhoff, eds) Reidel, Dordrecht (1985), p. 177.
2 S. Green, *J Chem. Phys*, **64** (1976), 3463
3 S Green, *J Chem Phys*, **70** (1979), 816
4 S Green, *J Chem Phys*, **73** (1980), 2740
5. H Meyer, U Buck, R Schinke and G H F Diercksen, *J Chem Phys*, **84** (1986), 4976
6 R Ahlrichs, R Penco and G Scoles, *Chem Phys*, 1° (197) 119
7 K T Tang and J P Toennies, *J Chem Phys*, **80** (1984), 3726
8 C Douketis, J M Hutson, B J Orr and G Scoles, *Mol Phys*, **52** (1984), 763.
9 R T Pack, *J Chem Phys*, **60** (1974), 633
10 W N Sams and D J Kouri, *J Chem Phys*, **51** (1969) and **51** (1969), 4815
11 D Secrest, in *Methods of Computational Physics* (B Alder, S Fer bach and M Rotenberg, eds), vol 10, Academic Press, New York (1971), pp 243

STUDIA UNIV BABEŞ-BOLYAI, PHYSICA, XXXIII, 1, 1988

DETERMINATIONS OF DOUBLE IONIZATION POTENTIALS IN SOME AROMATIC COMPOUNDS WITH WIEN FILTER DOUBLE FOCUSING MASS SPECTROMETER

STELA CUNA*, CORNEL CUNA* and MIRT TONI**

Dedicated to Professor IOAN URSU on his 60 th anniversary

Received February 10, 1988

ABSTRACT. — The stripping reaction of benzene, toluene, p-xilene, Br-benzene, phenol, anisol and aniline have been studied at a double focusing mass spectrometer with inhomogeneous Wien filter using air as collision gas From the position of the maximum of the peaks in spectra we have measured the values for Q, and these values give the difference between the double ionization potentials and the single ionization potentials of the compounds The values of double ionization potentials are in good agreement with our experimental results

The IKE spectra with Wien filter double focusing mass spectrometer realized in our Institute have about the value E/2 of the potential applied to the electric deflector, a cluster of peaks, partially overlapped This cluster of peaks, appearing when the precision in the analyser is 6.6×10^{-3} Pa, is the result of the collision induced processes

From the detailed analysis of each cluster of peaks corresponding to the studied substances (benzene, toluene, p-xilene, Br-benzene, phenol, anisol, aniline) it is possible to say that they result from the following processes.

— the formation of the double charged ions $[C_6H_5X]^{2+}$,

— for the ions $[C_6H_5X]^+$ with even mass, the fragmentation into one ion and one fragment with the same mass is possible

After the collision of the ions $[C_6H_5X]^+$ with the molecules of the residual gas, the ions are excited This fact is possible due to the initial kinetic energy of the ions This energy is very close to the energy corresponding to the value E/2 The energy necessary to yield in this way double charged ions is brought from the kinetic energy of the reactant ions

Taking into account that the ions undergoing the stripping reaction are in the fundamental state, these reactions may be used to determine double ionization potentials. For the ions with many atoms, having the kinetic energy in the range of KeV and near zero scattering angles, the minimum difference in kinetic energy of the ions $[C_6H_5X]^+$ and $[C_6H_5X]^{2+}$ may be well approximated by [1]

$$Q_{min} = DIP[C_6H_5X]^+ - IP[C_6H_5X]^{2+}$$

* *Institute of Isotopic and Molecular Technology, 3400 Cluj-Napoca, Romania*

** *rie al Leee, Sascut, Cluj-County, Romania*

The stripping reaction of benzene, toluene, p-xilene, Br-benzene, phenol, anisol and aniline has been studied with the double focusing mass spectrometer with inhomogeneous Wien filter [2], using air as collision gas This mass spectrometer has "reversed geometry". the ions traverse the Wien filter ahead of the electric deflector As a function of the applied fields the Wien filter may

Table 1

The Q values and the double ionization potentials of some aromatic compounds

Compound	Ion composition	Q (eV)	Double ionization potentials (eV)	
			Experimental	Literature
Benzene	C_6H_6	16	25 2	26 0
Toluene	C_7H_8	15	23 8	24 5
p-xilene	C_8H_{10}	11	19 7	—
Br-benzene	C_6H_5Br	8	16 9	—
Phenol	C_6H_5OH	8	16 5	—
Anisol	C_7H_8O	5	13 2	—
Aniline	$C_6H_5NH_2$	14	21 7	—

have a focusing action in the median plane or have a defocusing action The electric deflector having auxiliary plates may work with a variable field index. In order to study spontaneous or collision-induced transition the instrument may be switched from MIKE to IKE mode without breaking the vacuum. Examining the IKE spectra of the abovementioned aromatic compounds, obtained with this mass spectrometer, we rended evident the peaks corresponding to the reactions giving rise to the double charged ions $[C_6H_5X]^{2+}$ From the position of the maximum of the peaks in spectra we have measured the values for Q and these values give the difference between the double ionization potentials and the single ionization potentials of the compounds For the values of the single ionization potentials we have used the data from literature [3] Table 1 gives the Q values and the double ionization potentials determined using the method described by R G Cooks, T. Ast and J H. Beynon.

The values of DIP that we find in literature are in good agreement with our experimental results (see Table 1)

REFERENCES

1. R G Cooks, T Ast and J H. Beynon, *Int J Mass Spectrom Ion Phys*, **11**, (1973), 490.
2 C Cuna and D Ioanoviciu, *Int J Mass Spectrom. Ion Phys*, **54** (1983), 333
3 J L Franklin, J. D Dillard, H M Rosenstock, J H Herron, K Drasel and F M Field in „Ionization Potentials, Appearance Potentials and Heats of Formation of Gaseous Positive Ions", *NSRDS—NBS No* **26**, National Bureau of Standards, Washington, (1969).

STUDIA UNIV BABEŞ-BOLYAI, PHYSICA, XXXIII, 1, 1988

LINEAR SWEEP VOLTAMMETRY ON PALLADIUM ELECTRODE

II Blocking effect of sulphur compounds upon the hydrogen adsorption

FELICIA BOTA* and CRISTINA RADU*

Dedicated to Professor IOAN URSU on his 60 th anniversary

Received March 28, 1988

ABSTRACT. — The linear sweep voltammetry technique applied on effective surfaces determination of an electiode is presented Also, the surface coverage with an adsorbed poison is evaluated, either by changing the concentration, for a constant immersion time, or by changing the immersion time, for a constant concentration of poisoning solution

1 **Introduction.** The galvanostatic desorption of hydrogen held in a finite quillibrated (Pd—H) electrode is strongly influenced by the properties of the interface region These properties are depending either on the physical structure of the surface layer (electrodeposition of Pd black with different roughness factors), or on the chemisorption of some surface active substances, which could affect the electronic state of the electrode surface [1, 2] We have reported that the presence of sulphur compounds at the electrode surface alters the kinetic parameters values, whatever the initial suplhur compounds were (thiourea or cysteine), because the poisoning product should be a monolayer of sulphur [3]

In this paper, the adsorption of thiourea on palladium electrodes is studied, either for different concentrations of THU solution, or for different immersion times of palladium in a given solution It is known that the amount of sulphur chemisorbed on the palladium surface is strictly equivalent to the amount of THU previously adsorbed on the surface and consequently the sum of the charges consumed for oxidation of surface layer enable us to evaluate the adsorption concentration of THU [4]

2 **Experimental.** The working electrode was a Pd disc, with a geometrical area exposed to solution $S_g = 0\,277$ cm², supported on a small Pt clamp, in order to be able easily to remove the sample It was covered with Pd-black by electrodeposition of Pd from a bath tested by Ibl [5] The electrodeposition was carried out under conditions of natural convection, at constant current This electrode, having a roughness factor $f_w = 260$ was poisoned by immersion in a THU solution with a concentration ranging between 10^{-4} M — 10^{-2} M for three minutes It was then removed from the THU solution, carefully rinsed with a stream of twice distilled water and further introduced into an electrochemical cell filled with 1 M KOH solution, at 20°C The cell was provided with a hydrogen reference electrode connected to it by a Luggin capillary and an auxiliary Pt wire electrode The solution was continuously stirred by babbling pure argon.

The amount of THU adsorbed on the Pd electrode was estimated by anodic oxidation with the linear sweep voltammetric technique The current-potential curves have been recorded at a

* *University of Cluj-Napoca, Faculty of Mathematics and Physics 3400 Cluj-Napoca, Romania*

constant scan rate of 20 mV/s, using an Electroscan TM Electroanalytical system (Beckman) We started to scan the potential always from the equilibrium value of Pd electrode, first towards the anodic region up to 1 6 V and backwards to the cathode region, up to 0 3 V At this time the applied potential was switched off, the Pd electrode removed from the cell, and carefully rinsed with a stream of twice distilled water Further, it was replaced into the cell and there was a rest period until the new equilibrium potential was established The next scan of the potential started from this new equilibrium value, and a new current-potential curve was recorded This operation was repeated until reproducible I—E curves were obtained, indicating that the adsorbed substance was completely removed from the electrode surface, and its initial electrochemical characteristics restored

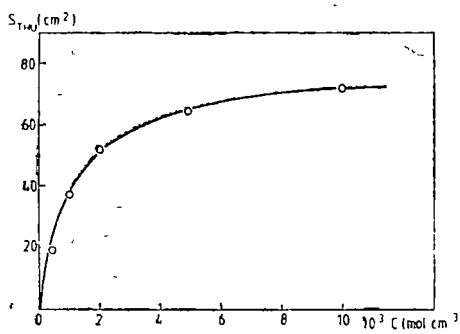

Fig 1

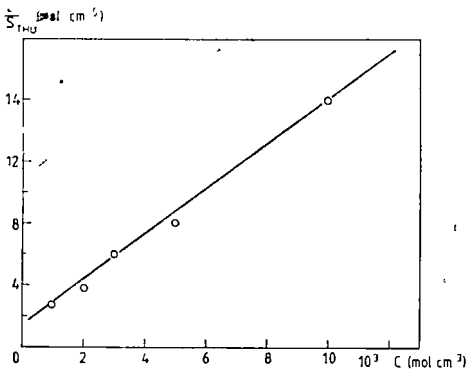

Fig 2

Table 1

t (min)	S_{THU} (cm²)	S_w (cm²)	S_w (cm²)	C_{THU} (M)	θ (%)
3	72	80		$1 \cdot 10^{-2}$	91
3	63 6	79 1		$5\ 10^{-3}$	83
3	56 5	76 9	77 75	$3\ 10^{-3}$	73
3	51 6	76 8		$2\ 10^{-3}$	67
3	36 7	79		$1\ 10^{-3}$	47
3	18 4	74 7		$5\ 10^{-4}$	25

3. Discussion. The sum of the anode charges Q_a spent for removing THU from the electrode surface enables us to estimate the amount of adsorbed compound at the surface of Pd electrode, and consequently the values of the surface area S_{THU} occupied by THU, for different concentrations. The cathode charges Q_c, spent for removing the oxide from the electrode surface also enable us to estimate the real surface S_w of the clean electrode. So, we were able to calculate the degree of electrode coverage (Table 1)

The dependence of the surface area S_{THU} on the THU solution concentration is illustrated in Fig. 1 which represents the adsorption isotherm. The plot of C/S vs C is a straight line, which is a good confirmation of the adsorption isotherm (Fig 2)

If the working electrode is changed by another, with a roughness factor $f_w = 26$ (ten times smaller than the first one), the adsorption isotherm is the same. It is interesting that the coverage can also be watched by keeping the concentration constant, for different time intervals of immersion in THU solution with a constant concentration $C = 10^{-3}$ M (Table 2) At the same time, the dependence of S_{THU} vs time represents an adsorption isotherm, too. (Fig. 3), with a linear dependence between t/S vs time (Fig. 4)

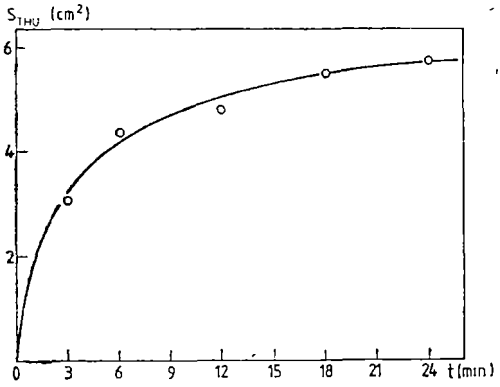

Fig 3.

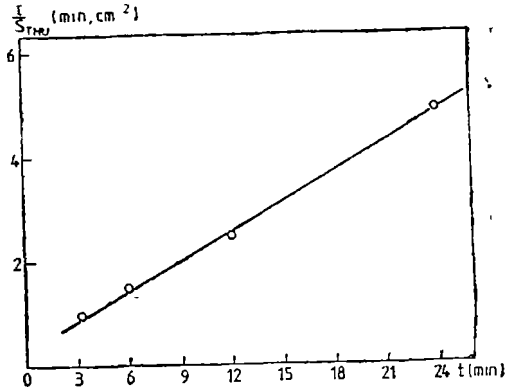

Fig 4

Table 2

t (min)	S_{THU} (cm²)	S_w (cm²)	S_w (cm²)	0 (%)
3	2 98	7 56		39
6	4 31	7 28		59
12	4 80	7 32	7 35	64
24	5 75	7 24		81

We conclude that the linear sweep voltammetry technique is very useful for adsorption phenomena studies. A lot of surface parameters can be determined by means of this technique. It is very important to be able to determine effective surfaces for electrodes with different roughness factors, and to evaluate the areas occupied by some adsorbed substances.

REFERENCE

1 R V Bucur and F Bota, *Electrochim Acta*, **27**, 521 (1983)
2 R V Bucur and F Bota, *Electrochim Acta*, **29**, 103 (1984)
3. R V. Bucur and F Bota, *Electrochim Acta*, **29**, 1283 (1984)
4 Felicia Bota and R V. Bucur, *Studia univ „Babeş-Bolyai"*, *Physica*, **32** (1), 9 (1986)
5 N Ibl, G Gut and M Weber, Electrochim. Acta, **18**, 307 (1973)

STUDIA UNIV BABEŞ-BOLYAI, PHYSICA, XXXIII, 1, 1988

ESR EVIDENCE OF STRUCTURAL PHASE TRANSITION IN Na_2SeO_4

I. BARBUR* and S. SIMON*

Dedicated to Professor IOAN URSU on his 60 th anniversary

Received March 23, 1988

ABSTRACT. — The temperature dependence of the powder ESR spectrum of the paramagnetic centers in gamma-irradiated Na_2SeO_4 is discussed The appearance of a new ESR line at $g = 2\,0216$ attributed to the SeO_4^- radical indicates a possible structural transition at 165 K in Na_2SeO_4

1 **Introduction.** The magnetic resonance studies organized and developed at the University of Cluj-Napoca by I Ursu [1, 2] had a significant role in the later investigations concerning the correlation between structural and physical properties of the solid state [3—6]. A persistent problem throughout this study was that of detecting, using the ESR method, of many kinds of radicals trapped in radiation-damaged inorganic crystals, especially ferroelectric crystals [7—10]

Electron spin resonance (ESR) spectroscopy has proved to be an elegant tool for the study of radiation defects in crystals It should be noticed that the absence of an ESR spectrum does not necessarily prove the absence of radiation damage though The initial products may have been unstable at the temperature of the experiment, having recombined or decomposed to form diamagnetic products The presence of the latter may be inferred by optical spectroscopy or other methods, but is not revealed by ESR

The utility of ESR method as applied to a study of structural transition in solids consists in the identification of the type of defects produced by radiation and in the investigation of its ESR parameters through transition temperature

This paper will attempt to present new aspects concerning the structural changes which appear in Na_2SeO_4 near the transition point evidenced by the ESR properties of the SeO_4^- radical

Sodium selenate belongs to a class of substances as $NaNH_4SeO_4$, K_2SeO_4, which presents ferroelectric transition [11, 12] As it has been shown [13] gamma irradiation of Na_2SeO_4 produces paramagnetic species identified as SeO_2^-, SeO_3^-, SeO_4^-. The radicals SeO_2^- and SeO_3^- are observable at room temperature. The SeO^- radical is used as a probe of structural phase transition in Na_2SeO_4.

2 Experimental. Paramagnetic centers were produced in powdered samples of Na_2SeO_4 by a ^{60}Co gamma source for 100 hours at room temperature. The ESR spectra were recorded at X-band (~9 2 GHz) frequencies, using a JES—3B spectrometer at room temperature (300 K) and at 77 K Variable temperature studies on the powder samples were achieved by means of

* *University of Cluj-Napoca, Faculty of Mathematics and Physics, 3400 Cluj Napoca Romania*

cold nitrogen gas flow technique using a JET—VT—2 variable temperature accesory. The temperature was monitored with a copper-constantan thermocouple

Experiments were carried out in the temperature range from 300 K to 137 K and 77 K.

3. Results and discussion. As in previous measurements [13] the species SeO_3^- is the main product in gamma irradiated Na_2SeO_4. The g — tensor of this radical is of cylindrical symmetry. The second radical identified at room temperature is SeO_2^-, the g — tensor of which is similar to those which have already been reported [13, 14].

The temperature dependence of ESR absorption line in the derivative form is shown in Fig 1

As the temperature decreases a distinct line A at g = 2 0216 appears at about 165 K This line may be attributed to SeO_4^- radical which was first observed in K_2SeO_4 by irradiation at 77 K [12] This radical disappears on warming the sample to room temperature and is reversible The ESR lines show no hyperfine features due to ^{77}Se All this leads us to conclude that the appearance of the SeO_4^- at 165 K denotes a structural change in Na_2SeO_4 at this temperature The appearance of the SeO_4^- at low temperatures indicates a distortion of this radical below 165 K. The high symmetry of the SeO_4^- radial at high temperatures is thought to be due to fast reorientation of this group.

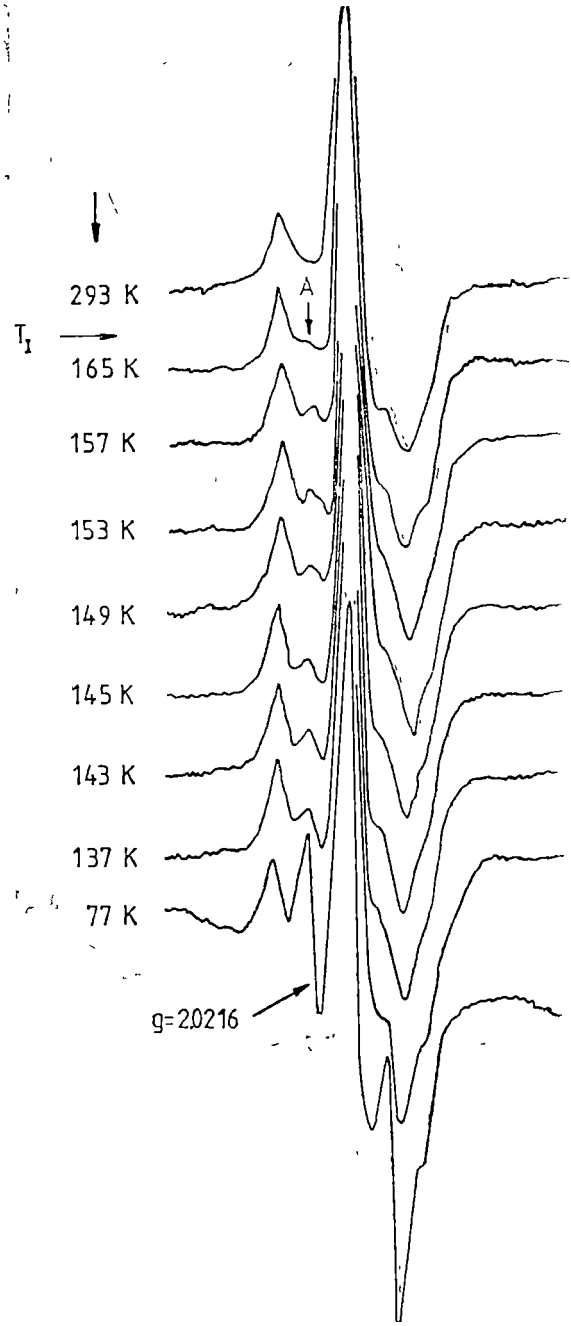

Fig 1 The temperature dependence of ESR absorption line in gamma-irradiated powder Na_2SeO_4

The structural phase transition in Na_2SeO_4 at 165 K may be connected with the structural phase transition from the paraelectric normal phase to an incommensurate phase at $T_I = 129.5$ K detected in isomorphous K_2SeO_4 [15].

The investigations of a possible transition between 137 K and 77 K are in progress.

REFERENCES

1 I Ursu, *Rezonanta electronică de spin*, Ed Acad R S R , Bucureşti, 1965
2 I Ursu, *La resonance paramagnetique electronique*, Dunod, Paris 1968
3 I Ursu, *Rev Roum Phys* , **9**, 263 (1964)
4 I Ursu, V Grecu, I Barbur, *Rev. Roum Phys* , **10**, 585 (1965)
5. I Ursu, V Lupei, S. V Nistor, *Atomic Energy Review* (Viena), **5**, 97 (1967)
6 I Ursu, *Rezonanţă magnetică în compuşi cu uraniu*, Ed Acad R S.R , Bucureşti, 1984
7 A Căluşaru, I Barbur, I Ursu, *J Chim Phys* , **2**, 249 (1965).
8. I Barbur, *Phys Stat Sol.*, **34**, 711 (1969)
9 I. Barbur, *Phys. Stat Sol* (*b*), **45**, K 129 (1971)
10. I. Barbur, *Physica*, **58**, 324 (1972)
11 K. S Aleksandrov, I P Aleksandrova, L I Zherebtsova, M P Zaitzeva, A. T. Anistratov, *Ferroelectrics*, **2**, 1 (1971).
12. P W. Atkins, M. C. R. Symons, H. W Wardale, *J Chem Soc* , **5**, 5215 (1964).
13. I Barbur, L. Stănescu, *Studia Univ Babeş-Bolyai, Physica*, **31**, 41 (1986).
14 K. Aiki, *J Phys. Soc. Japan*, **99**, 379 (1970)
15. M. Fukui, R. Abe, *Jap J Appl Phys* , **20**, L, 533 (1981)

STUDIA UNIV BABEŞ-BOLYAI, PHYSICA, XXXIII, 1, 1988

VELOCITY DETERMINATION FOR STEADY DOMAINS IN TRANSFERRED ELECTRON DEVICES

G. BUZAS* and AL. NICULA**

Dedicated to Professor IOAN URSU on his 60 th anniversary

Received March 22, 1988

ABSTRACT. — A method for the determination of steadily travelling domains in transferred electron devices is described Two cases are considered a) quasi-equilibrium between high and low mobility valleys, and b) the influence of infervalley transitions is taken into account. It is shown that the former is a limit case of the latter The resulting expressions show that the domain velocity is slowly influenced by its shape. Numerical results are in good agreement with data based on other methods

1. **Introduction.** It is important to determine the domain velocity in transferred electron devices, since this parameter determines the oscillation frequency if the geometry is fixed. The general theory of the differential equations for those governing the process of the domain propagation gives solutions for the (E, ρ, x) space only. Because this method is complicated and it is difficult to interprete its results, there are other methods to evaluate the domain velocity. The method of equal areas was developed by Butcher and Fawcett [1], [2], while its generalization belongs to Gelmont and Shur [3]. Volkov [4] sets the domain velocity in terms of the analogy between the equations of the problem and the equations of an undamped oscillation of a mass centre

In this paper we present a method to determine the domain velocity and the current through the sample in the presence of steadily travelling domains. The method can be used in conjunction with its applicability to transferred electron devices whose functioning is based on the RWH mechanism. Namely in which, as was developed by Ridley and Watkins [5] and Hilsum [6], the negative differential conductivity is due to the field dependent electron transfer from the high mobility valley to the low mobility valley. Two cases will be considered a) the case of quasi-equilibrium between high and low mobility states (instantaneous transitions), and b) the case of non-instantaneous transitions. Further on, we consider that the domain represents a space charge wave propagating with velocity u.

2 **Velocity Determination.** The process of domain propagation in transferred electron devices can be studied by equations describing the behaviours

* *Research Institute for Computer Technique and Informatics, 3400 Cluj-Napoca, Romania*
** *University of Cluj-Napoca, Faculty of Mathematics and Physics, 3400 Cluj-Napoca, Romania*

of the electrons and the electric field within the sample. These equations are: the equation of total current, the continuity equation and the Poisson equation.

$$\vec{j} = \rho_i \cdot \mu_i \vec{E} + \operatorname{grad}(D_i \cdot \rho_i)$$
$$\frac{\partial \rho_i}{\partial t} - div\, \vec{vj} = (-1)^i \varphi_{12}(\rho_i, E) \tag{1}$$
$$div\, \vec{E} = \frac{4\pi}{\varepsilon}(\rho_0 - \rho_1 - \rho_2) = \frac{4\pi}{\varepsilon}\rho$$

In equations (1) $\rho_i = q \cdot n_i$. The index "1" refers to values from high mobility central valley, while "2" to those from low mobility upper valley. ρ_i and n_i represent the space charge densities, respectively the concentrations. ρ_0 is the positive space charge. D_i are the diffusion coefficients for which the Einstein relation is valid. $\varphi_{12}(\rho_i, E)$ is the function describing intervalley transitions. The electron transfer in both senses is characterized by the transition times τ_{12} and $\tau_{21} \cdot \varphi_{12}(\rho_i, E)$ has the form [7]:

$$\varphi_{12}(\rho_1, \rho_2, E) = \frac{\rho_1}{\tau_{12}} - \frac{\rho_2}{\tau_{21}} \tag{2}$$

and implicitly depends on E.

Our purpose is an analytical investigation of steadily travelling domain velocities when the total current is given [8] by

$$j = u \quad \rho + j_d = \text{const} \tag{3}$$

that is, the whole conduction and displacement current through the sample is constant

If we consider the one-dimensional case and using the relations (1) and (3) we obtain

$$j = \frac{u \cdot \varepsilon \cdot E}{4\pi} + j_d \tag{4}$$

$$j' = u \cdot \rho' = \frac{u \cdot \varepsilon \cdot E''}{4\pi} \tag{5}$$

$$E' = \frac{4\pi}{\varepsilon}(\rho_0 - \rho_1 - \rho_2) = \frac{4\pi}{\varepsilon}\rho \tag{6}$$

$$u \cdot \dot{\rho}_1 + j_1' = \varphi_{12}$$
$$u \quad \dot{\rho}_2 + j_2' = -\varphi_{12} \tag{7}$$

It must be pointed out that in order to discuss the domain displacement, this requires a solution of an essentially non-linear differential equation system (4)—(7) Let us consider two cases: a) assuming the quasi-equilibrium between valleys, namely the transitions take place instantaneously and b) taking into account their influence on the domain displacement.

a) *Quasi-equilibrium between Valleys* Knowing the orders of magnitude of time constants, as a first approximation we assume that inside the domains a quasi-

equilibrium exists between the high and low mobility states In this situation $\varphi_{12} \equiv 0$ and consequently, from (2) we have $\frac{\rho_2}{\rho_1} = \frac{\tau_{21}}{\tau_{12}} = \gamma(E)$. Then from (6) we obtain :

$$\rho_1 = \frac{\rho_0 - \varepsilon \cdot E/4\pi}{1+\gamma}, \qquad \rho_2 = \frac{\gamma(\rho_0 - \varepsilon \cdot E'/4\pi)}{1+\gamma} \tag{8}$$

As a main variable it is recommendable to choose the electric field because it is generally known from experiments The differential equation for E is obtained by replacing these expressions in (6). The domain velocity and the current are computed by the relations (4), (5), (7) and (8) To simplify further calculations, it is convenient to introduce the following average values :

$$V = \frac{v_1 + \gamma v_2}{1+\gamma}, \qquad D = \frac{D_1 + \gamma D_2}{1+\gamma}, \qquad D' = \frac{D_1' + \gamma D_2'}{1+\gamma} \tag{9}$$

and

$$\tau = \frac{\varepsilon}{4\pi \rho_0 \mu_1}, \qquad \delta = \frac{E}{\gamma}\frac{d\gamma}{dE}, \qquad F_i = \frac{\varepsilon}{4\pi}\left(\frac{d^i E}{dx^i}\right)$$

A simple but longer calculation gives the domain velocity and the current

$$-u = v + \frac{\delta \cdot \gamma(D_1 - D_2)}{\tau \; v_1(1+\gamma)^2} - \frac{D' \cdot E}{\tau \cdot v_1} + D\frac{F_3}{F_2} \tag{10}$$

$$j_d = v \quad \rho_0 - D \quad F_2 \tag{11}$$

Notice that, by means of F_i factors, the computed amounts depend on the domain shape, i e. the high field distribution in space.

To determine the order of magnitude of the term influenced by the domain shape let us use the following data [9] which refer to GaAs : $\mu_1 = 8 \times 10^3 \text{cm}^2/\text{Vs}$, $\mu_2 = 200 \text{ cm}^2/\text{Vs}$, $D_1 = 240 \text{ cm}^2/\text{s}$, $D_2 = 60 \text{ cm}^2/\text{s}$, $\varepsilon = 12\,5$, $\rho_0 = 10^{14}\text{cm}^{-3}$, $\tau_{12} = 5 \times 10^{-14}\text{s}$, $\tau_{21} = 5 \times 10^{-12}\text{s}$, $E_{\text{th}} = 4\,3 \times 10^3 \text{ V/cm}$, $\gamma(E) = (E/E_{\text{th}})^k$, $k = 2\,3$. We admit the Gaussian shape for the domains $E = E_0 \exp[(-x/d)]^2$ with $d = 20\ \mu m$, $E_0 = 5 \times 10^4 \text{V/cm}$. With these data we get an order of magnitude of 10^5 cm/s This value is small as compared to the order of magnitude of $10^6 - 10^7$ cm/s of domain velocities. To illustrate that diffusion makes only a small contribution to the domain velocity, here are the values of terms two and three from (10) $T_2 = 1\,.53 \times 10^5 \text{ cm/s}$, $T_3 = 1.054 \times 10^4 \text{ cm/s}$

b) *The Influence of Transitions on the Domain Velocity* Taking into account the intervalley transitions, computing is more difficult since $\varphi_{12} \neq 0$. For the sake of simplicity the mobilities and the diffusion coefficients were assumed field independent in both valleys The method previously used can be applied in a similar way At first we express the charge densities, further on we also set the other quantities in terms of electric field and its derivatives Finally we conclude

$$-u = \frac{(D_1/v_1 \quad \tau_{12})(\alpha_1 + \delta \quad \tau_{21} + \alpha_2)}{(D_1/v_1^2 \quad \tau_{12})\alpha_3 + \alpha_2 + \delta \quad \alpha_4} \tag{12}$$

$$j_d = \frac{v_1^3 \quad \rho_0 \cdot \tau}{D_1}\left[\alpha_2 + D_1 \quad \tau(1 + \mu_2/\mu_1)\frac{F_2}{F_0}\right] \tag{13}$$

The concrete form of the terms α_i iś complicated, they depend on γ, τ_{12}, τ_{21}, D_1, D_2 and F_i. Introducing the shape parameters α_i, an algebraic equation system ıs derived to determine the domain velocity and current. (12) and (13) are also influenced by the field distribution in space.

We will now examine the conditions to be satisfied by some quantities to make the quasi-equilibrium valid

As we mentioned above, we may admit in the first approximation that the domain velocity is independent by its shape Neglecting the terms influenced by the domain shape and taking into account D_1, D_2 = const, relation (12) for velocity may be rewritten as follows:

$$-u = \frac{v + \delta\ \gamma(D_1 - D_2)/v_1 \cdot \tau(1+\gamma)^2 + v_2\tau/\tau_{12}}{1 + (\tau/\tau_{12})(1 + \gamma\mu_2/\mu_1)/(1+\gamma)} \qquad (14)$$

If the field is high enough then $\gamma \gg 1$ and $\tau/\tau_{12} \ll 1$ thus from (14) ıt reappears $-u \approx v + \frac{\delta}{\tau}\frac{\gamma(D_1 - D_2)}{v_1(1+\gamma)^2}$. Consequently we demonstrated that what was treated in quasi-equilibrium approximation ıs a limit case of the general case in which the influence of the intervalley transitions ıs taken into account.

3 **Results.** We found few information on computed or measured values of domain velocity with today's literature Most of them refer to GaAs, the most adequate material for transferred electron devices In Table I we present a comparison of the domain velocities computed by the relation (10) with those obtained by method of equal areas [10], by means of an empirical formula [11] and those determined experimentally [11]. Notice that we have taken into account only those values of E for which we have found comparative data

Table 1

E	u ($\times 10^6$ cm/s)	u[10] ($\times 10^6$ cm/s)	u[11] ($\times 10^6$ cm/s)	u[11] ($\times 10^6$ cm/s)
$2E_{th}$	14 82	9 9	10	
$3E_{th}$	9 189	8 6	8 5	
$4E_{th}$	6 592	6 3	5 9	9 8
$5E_{th}$	5 578	5 8	5 5	8 8
$6E_{th}$	5 195	5 3	5 1	8 6

Comparing columns 2, 3 and 4 we see a good agreement between the results computed here and those issued in [10], [11] If a problem does arise, ıt refers to the experimentally determined velocities Generally, experimentally measured velocities are smaller Based on experimental research, this ıs due to the influence of traps. There are some theoretical studies (e g [12]) in which this problem is treated

4 **Conclusions.** In this section we summarize the main results of the paper as follows

A method for the determination of the domain velocity and total current in transferred electron devices is described. In both cases considered (quasi-equilibrium between valleys and noninstantaneous transitions) the domain velocity and the current are given in terms containing the influence of domain shape. As ıt is shown, the former is a limit case of the latter. Assuming a proper domain shape and concrete parameters of GaAs our numerical results are in good agreement with data based on other methods

REFERENCES

1. P. N Butcher, W. Fawcett, *Phys Lett*, **21,** 489 (1966)
2. P N Butcher, W. Fawcett, *Britt. J. Appl. Phys*, **18,** 755 (1967)
3. B. L Gelmont, M S Shur, *Fiz i Tehn Poluprov*, **5,** 2116 (1971)
4. A F Volkov, *Phys. Lett.*, **20,** 598 (1966)
5. B. K Ridley, T B. Watkins, *Proc Phys Soc London*, **78,** 293 (1961)
6. C. Hilsum, *Proc IRE*, **50,** 185 (1963).
7. B K. Ridley, *Proc. Phys Soc London*, **86,** 637 (1965)
8. V L Bonci-Bruevici, *Fiz Tverd Tela*, **8,** 1753 (1966)
9. M. Neuberger, *Handbook of Electronic Materials*, Plenum Press, New York, 1971
10. Y. Nishimura, *Electronics Lett*, **4,** 249 (1968)
11. T Toyabe, H Kodera, *Proc of the Int Conf on Physics of Semiconductors*, Stuttgart, 1974, p 619
12. B. K. Ridley, *Britt J Appl Phys*, **17,** 595 (1965).

STUDIA UNIV BABEŞ-BOLYAI, PHYSICA, XXXIII, 1, 1988

PHASE TRANSITIONS OF THE Y-TYPE ZEOLITES INVESTIGATED BY THERMAL ANALYSIS, XRD AND EPR METHODS

ELEONORA TRIF*, DORINA STRUGARU*, I. IVAN**, R. RUSSU***, GABRIELA GHEORGHE*** and AL. NICULA*

Dedicated to Professor IOAN URSU on his 60 th anniversary

Received April 2, 1988

ABSTRACT. — Thermal analysis in relation to XRD and EPR methods provides useful tools in studying various properties of zeolites, it being conclusive that the thermal stability and various structural changes depend on the nature and content of exchangeable cations Cation exchange with rare earth and protons increases the thermal stability of Y zeolite, whereas the iron containing zeolites exhibits lower thermal stability

1. **Introduction.** Zeolites are enjoying tremendous interest in both the scientific and industrial world. They are used on a large industrial scale for a great variety of processes, from simple drying to complicated catalysis reactions in sophisticated combinations with other compounds The zeolites of type X and Y have been extensively used as catalysts for petroleum cracking and hydrocarbon conversion reactions High thermal stability is one of the important prerequisites for solid catalysts such as zeolites The thermal stability of the zeolite framework depends considerably on the type of cations, their distribution among the non-framework sites and the degree of cation exchange.

The zeolites of type A, X and Y modified with multivalent cations were the subject of a number of our previous studies [1—4] The aim of the present work is to evidence some structural and thermal properties of the cation exchanges NaY-type zeolites obtained from ICITPR-Ploieşti The compounds have been analysed by thermal analysis, XRD and EPR spectroscopy methods.

2 1 **Thermal analysis.** The chemical composition of the investigated sample is presented in Table 1

Table 1

Composition of the samples

Samples	SiO_2/Al_2O_3 mol	Na_2O % *wt*	MnO % *wt*	Fe_2O_3 % *wt*	Ads capac *g* C_6H_6/100 g
1 NaY (sol silicic acid)	5 1	9 68	0 003	0 10	25 0
2 Fe NaY (sol silicic acid)	5 1	9 40	0 003	0 36	25 4
3 FeNaY (sol silicic acid)	5 1	6 6	0 01	2 55	25 8
4 NaY (sodium silicate)	5 06	10 1	0 010	0 28	26 6
5 ReY (sodium silicate) % wt Re_2O_3—12 98	5 06	3 23	0 009	0 72	22 0
6 HY (sodium silicate)		0 41	0 005	0 27	20 3
7. FeNaY (sodium silicate)	5 06	9 80	0 009	0 54	26 0
8 FeNaY (sodium silicate)	5 06	6 6	0 021	3 00	26 2

* *University of Cluj-Napoca, Faculty of Mathematics and Physics, 3400 Cluj-Napoca, Romania*
** *ICI TPR, 2000 Ploieşti, Romania*
*** *ICIPMSM, 3400 Cluj-Napoca, Romania*

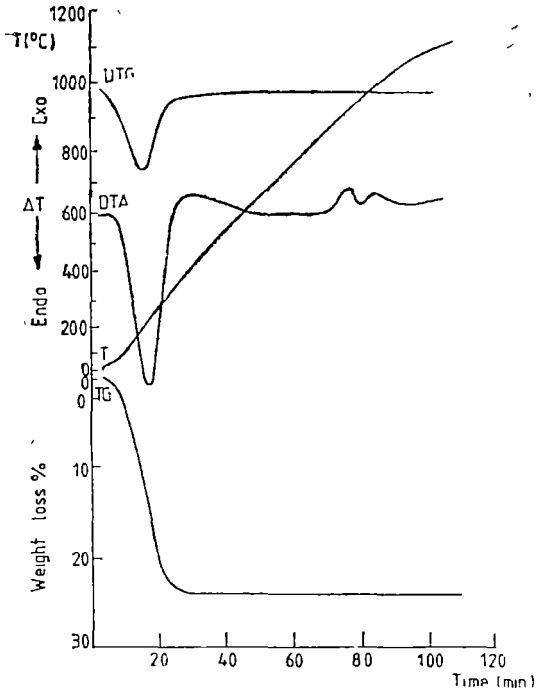

Fig 1 Typical thermal analysis curves for FeNaY—8 samples

The thermal analysis curves (TG, DTA and DTG, Fig. 1), were obtained by using the derivatograph type Paulik Samples were run in air atmosphere with constant heating rate of 10°/min and a maximum temperature of 1100°C.

The thermal analysis provides an excellent method of separating and identifying different structural changes of the samples The DTA curve is characterized by a sharp and strong endotherm peak (60—400°C) and two exoterm peaks. The low-temperature endotherm, $T_{peak} \approx 220$°C, is due to the loss of water from zeolite cavities. The high-temperature exotherms are attributed the first one, T_1, to the structural collapse of the zeolite lattice, and it is taken as a measure of thermal stability of the zeolite; the second one, T_2, corresponds to the phase transition to another crystalline phase (mullit, crystobalit, or quartz) as confirmed by the X-ray analysis The results of the thermal analysis on the parent and modified zeolites are presented in Table 2.

The partial replacement of sodium by rare-earth cations (ReY), or hydrogen (HY) enhances the thermal stability, as evidenced by both the increased exothermic T_1 peak values (Table 2) and the temperature, T_{amf}, at which the collapse of the zeolitic structure begins Although for iron exchanged samples

Table 2

Thermal analysis results

Samples	% Loss in *wt* from *TG*	*DTA*				*E* KJ/mol
		Min of endotherm peak (°C)	Base width °C	Exotherms (°C) T_1	T_2	
1 NaY (sol sil. acid)	26 0	230	70—400	930	—	18 66
2. FeNaY	26 0	230	40—480	950	1050	40 60
3 FeNaY	24 00	220	60—480	920	1060	30 74
4 NaY (sodium silicate)	26 4	230	60—400	830	920	18 70
5 ReY	24 3	220	60—400	960	—	23 90
6 HY	13 0	190	100—370	1000	—	26 70
7 FeNaY	24 0	230	100—420	850	920	22 80
8. FeNaY	22 0	220	90—410	920	1000	40 60

the values of T_1 increases, the modification of the skeleton structure begins at temperatures lower than that of the parent ones (Table 3) as evidenced by the XRD data for calcined samples.

The thermal analysis method has also been useful in an investigation of the intracrystalline water properties.

The process of dehydration of zeolites is reported by Freeman and Caroll [5] as belonging to the reaction type:

$$A(\text{solid}) \rightleftarrows B(\text{solid}) + C(\text{gas}) \tag{1}$$

and is usually described by equation

$$\frac{d\alpha}{dt} = A_0 \exp\left[-\frac{E}{RT}\right](1-\alpha)^n \tag{2}$$

where n is the order of reaction, α is the degree of conversion, whereas A_0 and E are constants representing the frequency factor and activation energy, respectively. The value of n were evaluated from DTA curves by means of Kissinger [6] methods

$$n = 1{,}26\sqrt{S}$$

where S is the shape index factor. It results that the process of dehydration of the studied zeolites follows the first-order kinetics ($n = 1$). The values of the „average" activation energy, given in Table 2, have been evaluated from

Table 3

Lattice constants

Samples	$a_0 \pm 0\,025$ (Å)						T_{amf} (°C)
	25 °C	600 °C	700 °C	800 °C	900 °C	1000 °C	
1. NaY (sol. acid)	24 57	—	24 61	24 50	—	—	820
2 FeNaY	24 61	—	24 62	24 58	24 55	—	800
3. FeNaY	24 59	—	24 56	24 53	24 58	—	650
4. NaY (sodium silicate)	24.52	—	24 51	24 63	—	—	700
5. ReY	24 46	—	24 50	24 54	24 54	—	820
6. HY	24 40	24.35	24 34	24 39	24 38	24 22	900
7. FeNaY	24 62	—	24 52	24 62	—	—	650
8. FeNaY	24.61	—	24 53	24,52	—	—	650

TG curves by applying the Coats-Redfern method [7]. At low temperatures, $T < T_{peak}$, the function

$$\ln\left[-\frac{\ln(1-\alpha)}{T^2}\right] = C - \frac{E}{RT} \tag{3}$$

is a straight line, Fig. 2, and, from its slope, activation energy can be derived. As the data from Table 2 evidence, the E values grow when the iron content is increased. This suggests that the water molecules are more strongly bonded to the multivalent cations [8] and confirms the formation of hydrated hydroxide clusters [9].

2.2. **XRD analysis.** The changes in the zeolite phase content were monitored from XRD spectra evolution. The X-ray powder patterns were obtained

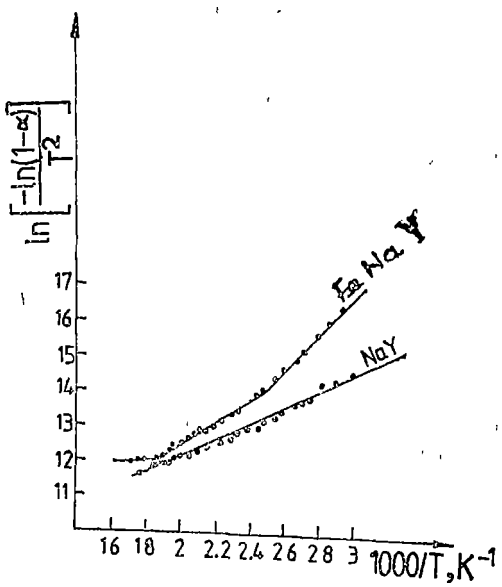

Fig 2 Linearization of TG curve for FeNaY—8 with the Coats—Redfern method ($n = 1$)

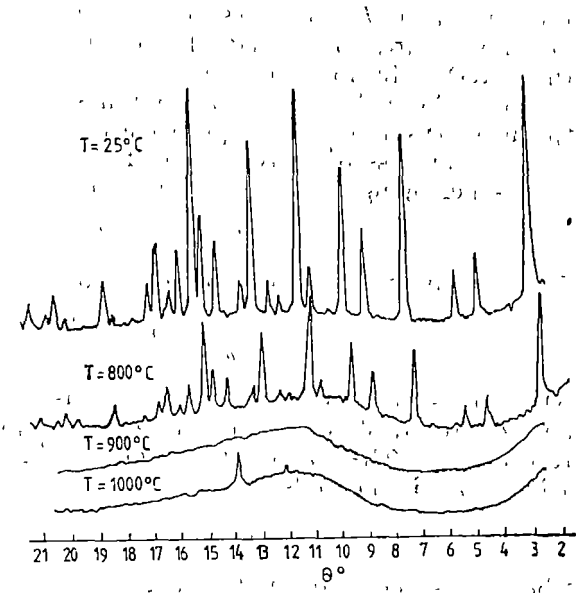

Fig 3 X-ray patterns of NaY—4 heated at different temperatures

at room temperature by a DRON-3 apparatus by means of CuK radiation ($\lambda = 1\,54178$ Å) and a rate of 10 mm/min. The samples were heated at different temperatures, between 300 and 1100 °C, for 4 h, in air atmosphere, and then rehydrated at room temperature.

The typical X-ray patterns for the studied samples, Fig. 3, are in agreement with the literature [10, 11] data. They can evidence the changes in crystallinity of the samples at high temperature, i.e., the break-down of the zeolite lattice and/or the transition to another crystalline phase.

The relative intensities and d values are dependent both on the degree of cation echange and on the nature of cations. Hence, for samples with rare-earth ions (ReY) the intensity of the peak corresponding to the 311 plane is diminished and lines 220, 620 and 444 are missing. It seems likely that the multivalent ions may not hold positions coincident with those held by the alkali metal cations, since they determine the modifications of the scattering factors.

The lattice constants, a_0, were calculated from the average of the $a_{hkl} = \sqrt{h^2 + k^2 + l^2}$, d_{hkl} values (cubic lattice) obtained from the Bragg spacings of the reflexions with $\theta > 10°$, for which the error of $\pm 0.05°$ in the determination of the reflecting angle gives rise to an uncertainty in a_0 within 0.025 Å. Hence, it results that the structure collapse begins at temperatures, T_{amf}, lower than that corresponding to the T_1 peak of the DTA curve. On the other hand, our investigations have evidenced that the exchangeable cations alter the size of the unit cell. Hence, the ReY and HY modified zeolites pre-

sent lattice contraction, and the iron exchanged ones evidence the dilation of the framework. By plotting the T_{amf} temperature of the samples against the corresponding lattice constant values of uncalcined samples, one can relate the thermal stability of the modified samples to their unit cell dimension, Fig. 4, a greater stability being related to one smaller a_0 value [12]. At the

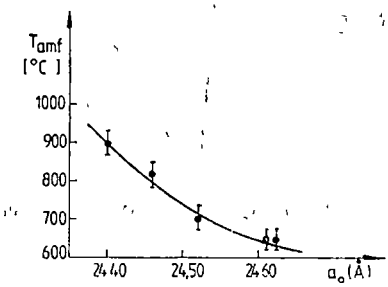

Fig 4 Lattice constant values, a_0, of uncalcined sample and the structural collaps temperature, T_{amf}, for samples derived from NaY—4 zeolite.

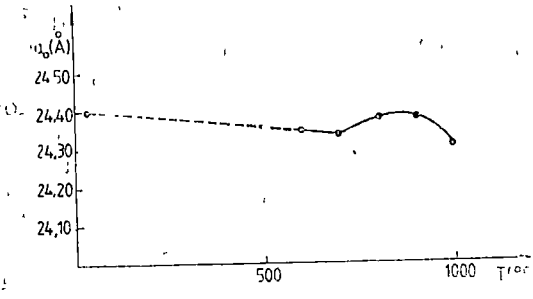

Fig 5 Lattice constant, a_0, versus the heating temperature for HY sample.

same time the stability depends on the nature and concentration of the exchangeable cations Our analysis evidenced the increase of the thermal stability of the modified zeolites of about 170 °C for HY zeolites, and of about 130 °C for ReY samples, respectively. On the contrary, the iron exchanged samples evidenced a decrease of the structural stability of about 50 °C. By following the dependence of a_0 on the calcination temperature, we obtained diagrams like the one presented Fig. 5. The results obtained for HY modified zeolites show that the most important feature of the curve is the minimum of a_0 at 700 °C. This means that the sample reaches a maximum degree of stabilization after 4 h of treatment at 700 °C. From decrease of a_0, entailed by increasing calcination temperature, $T > T_{amf} = 900$ °C, it may be inferred that the zeolite is neither homogeneous from the point of wiew of stability nor from that of its lattice constant values. Hence, the X-ray patterns evidence the gradual degradation of the structure. It is evident that in the course of heating, the less stable zeolite part will collapse first, whereas the remaining part, undamaged by thermal treatment will have a much lower destruction speed.

2.3. **EPR analysis.** Iron is always present in trace amount in parent zeolites [13]. When sodium silicate is chosen as starting reactant, for example in the case of NaY—4 zeolite, a broad resonance with $\Delta B = 0.16\ T$, at $g = 2\ \ 3 \pm 1$ is observed. This signal, in Fig. 6, suggests the presence of small particles of ferromagnetic substances (Fe_3O_4 or mixed ferrites) formed during nucleation of zeolites, from iron impurities present in the zeolitic starting reagents [14]. On the contrary, NaY—1 sample prepared from silicic acid, containing less that 20 ppm iron impurities, exhibits no observable ferromagnetic signal Since the main aim of this study is to detect the structural changes wich occur during the ion exchange and heat treatment, and since any ferromagnetic pattern disturbes the signal evolution for samples loaded with paramagnetic ions by ion

exchange, our paper is only concerned with the EPR results of the purer NaY —1 zeolite and of the modified FeNaY —2,3 samples The modified zeolites were prepared from the parent one, NaY—1, by ion exchange with aqueous solutions of trivalent iron Together with Fe^{3+} impurities, about 0 01 wt % of Mn^{2+} (expressed as MnO) was introduced in samples. It is to noteworthy that samples loaded withiron by ion exchange do not show ferromagnetism.

The effect of the thermal treatment was followed by comparing the EPR spectra taken at room temperature (JES—3B spectrometer) for three types of samples:

a) original, hydrated ones, used as prepared;

b) samples heated for 4 hours in air at temperatures between 300 and 1100°C;

c) samples undergoing the treatment under (b) followed by rehydration at room temperature.

The hydrated NaY—1 zeolite shows an isotropic EPR signal at $g = 4\,3$, with a line width of $\Delta B = 10$ mT It is the only one we detected in the purer zeolitic material. The spectrum at $g = 4.3$ evidences no significant changes upon heating Only a slight increase of its intensity and a shoulder at $g \approx 8$ was observed. This indicated a negligible effect of hydration and dehydration on the coordination and valency of the paramagnetic species, and hence this signal is attributed [15] to Fe^{3+} ions substituting for Al^{3+} in the framework of zeolites The slight increase in the signal intensity from hydrated sample tos heated ones certifies a small amount of ions solvated in the "intracrystalline fluid". Due to their short relaxation times, the $Fe(H_2O)_6^{3+}$ tumbling complexes cannot be evidenced by EPR experiments at room temperature [16] Dehydration forces the Fe^{3+} ions pierce into localized I', II or II' cation sites, which account for the slight increase of the $g = 4\,3$ signal intensity [13, 16]

As for ion exchanged zeolites, the hydrated samples show, Fig. 7a, a signal at

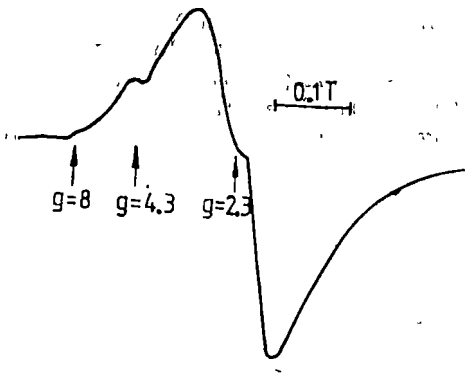

Fig 6 EPR spectrum for NaY—4 sample.

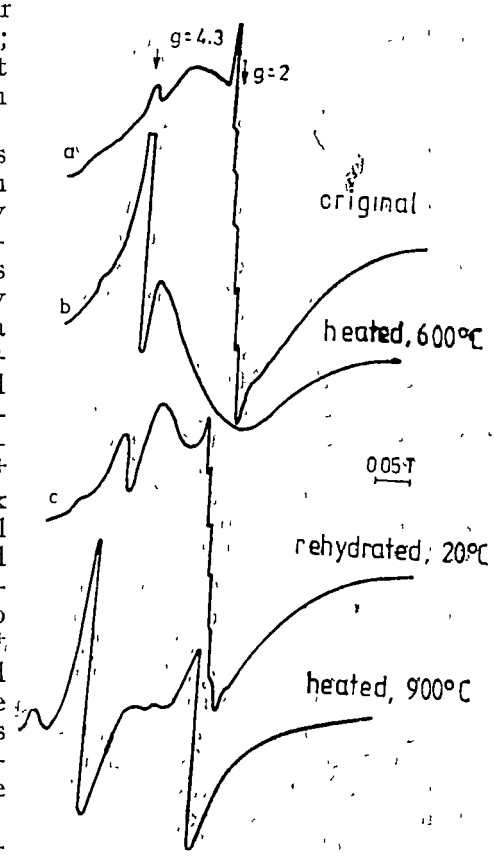

Fig 7 EPR spectra for FeNaY—8 sample.

$g = 4.3$ and a broad resonance at $g \approx 2$, upon which a hyperfine structure ($A \approx 10$ mT) is superposed. Fig. 7 presents the spectra evolution for samples containing 2% Fe_2O_3 and 0.01% MnO. The typical h.f. structure ($A \approx 10\,mT$) is due [17] to the presence of Mn $(H_2O)_6^{2+}$ complexes in the supercages. The broad line at $g = 2$, with $\Delta B = 120\,mT$ is attributed to the superparamagnetic species, i.e., to hydrated hydroxide clusters formed through hydrolysis of Fe^{3+} within the supercages. The calcination leads to cancellation both of the broad signal and of the h.f. structure, Fig. 7b, whereas a significant increase of the $g = 4.3$ signal has been observed. For samples which maintain their crystallinity upon heat treatment, $T < 650$°C, the room temperature rehydration results in the appearance, once again, Fig. 7c, of the EPR spectrum typical of original hydrated material. Under condition of severe treatment only, $T > 650$°C, an irreversible EPR signal occurs at $g = 2$ ($\Delta B = 30$ mT), suggesting the formation of several Fe^{3+}-rich phases.

The mechanisms likely to be responsible for the spectra evolution may be related to the decomposition of the hydrated hydroxide clusters, to the valency changes of the ions and/or to their migration to cation sites. The oscillating Fe^{3+} ions distributed among sites I′, II and II′ account for increased signal at $g = 4.3$. Actual point symmetry of the ligand field for all cation sites and for fully hydrated ones is orthorhombic or lower. Although for vibrational and EPR purpose, sites I′, II or II′ can be considered to have pseudo—C_{3v} or C_3 symmetry [18, 19] and hence an isotropic resonance, typical of disordered compounds [20, 21] occurs at $g = 4.3$.

The reversible character of the h.f. structure supports the idea of reversible valency changes for manganese ions. If these ions preserved their bivalent state they should always give resonance at $g = 2$, for both hydrated and dehydrated samples [17]. The redox reactions including Fe^{3+}, Mn^{2+}/Fe^{2+} Mn^{3+} couples, with the thermochemical decomposition of water [22] may explain the annihilation of the broad resonance and of the h.f. structure. On the other hand, a considerable fraction of the ions may form diamagnetic or antiferromagnetic bridged complexes of the type M—O^{2-}—M or M—OH—M [23, 24], which exhibit no EPR signal or exhibit a very large one at $g = 2.3$. In our opinion, the very large resonance, $\Delta B = 200$ mT, at $g = 2.3$, Fig. 7b, must have been due mainly to Fe^{3+} ions with a weak antifferomagnetic coupling.

On contact with water and air the Fe^{2+} and Mn^{3+} species are almost entirely converted back to original valency states. For samples treated at temperatures lower then $T_{amf} = 650$°C, the rehydration results in movement of ions from localized positions toward the supercage. This determines a decrease of the $g = 4.3$ resonance intensity and a regeneration of both the resonance with $\Delta B = 120\,mT$ at $g = 2$ and of the h.f. structure.

When a part of the zeolitic material collapses in the course of heating, $T > T_{amf} = 650$°C, clusters of stable oxides [9] (Fe^{3+}-rich phases) with a strong exchange coupling [25] are likely to be produced. Since the partial or total destruction of the zeolitic structure prevents migration of water and ions through the denser collapsed phase, the EPR signal exhibits no changes upon dehydration and rehydration. The intensity of this signal ($\Delta B = 30\,mT$, $g = 2$) increases if the content of the collapsed phase is increased and it is not sensitive

to any dehydration of the sample. Only by melting the material, $T > 900°C$, the paramagnetic ions get, once again, isolated in the vitreous matrices; the signal at $g = 2$ ($\Delta B = 30\ mT$) fades away and the intensity of the $g = 4.3$ signal increases again.

We may conclude by stating that the EPR study allowed us to follow not only the thermal stability of structure but also the ion dynamics and redox behaviour of iron and manganese contained simultaneously in the zeolite.

3 **Conclusions.** The thermal analysis provides a useful tool to estimate changes in the thermal properties and modifications in the zeolite lattice as a consequence of cation exchange.

Calculation of the energy of activation for dehydration involves the assumption that the water molecules are more strongly bonded to the multivalent cations and confirms the formation of hydrated hydroxide-type clusters. Supporting evidence is provided by EPR anylysis.

The thermal properties can be related to structural characteristics such as unit-cell dimensions. A decrease in lattice constant for modified zeolites is connected to an increased thermal stability. The results indicate that cation exchange with rare earth and protons increases the thermal stability of Y-type zeolite, whereas the iron containing zeolites exhibit lower thermal stability.

The EPR study allows to follow the ion dynamics, the redox behaviour, the thermal stability and the phase transitions of the sample.

The information acquired from thermal analysis in relation to XRD and EPR methods provide a useful beckground in studying various aspects of zeolites, it being concludent that the thermal stability and the structural changes of the modified zeolites depend on the nature and content of exchangeable cations.

This contribution is dedicated to Acad Prof Ion Ursu's 60th anniversary.

REFERENCES

1. I. Ursu and Al Nicula, *Rev Roum Phys*, **9**, 343 (1964)
2 Al Nicula, D Stamires and J Turkevich, *J Chem Phys*, **42**, 3684 (1965)
3. Al Nicula, I Ursu and S Nistor, *Rev Roum Phys*, **10**, 229 (1965)
4. D Strugaru and Al Nicula, *Studia Univ B B*, **1**, 56 (1977).
5. E. S Freeman and B Carrol, *J Phys Chem*, **62**, 394 (1958)
6. H E Kissinger, *Anal Chem*, **29**, 1702 (1957)
7. A W Coats and J P Redfern, *Nature*, **68**, 201 (1964)
8. A. J Chandwadkar and S B Kulkarni, *J. Therm Anal*, **19**, 313 (1980)
9. J R Pearce W. J Mortier, J B Uytterhoeven and J H Lunsford, *J. Chem Soc Faraday Trans*, **77**, 937 (1981)
10 V D Shiralkar and S B Kulkarni, *J. Thermal Anal*, **25**, 399 (1982)
11 D W Breck, „Zeolites Molecular Sieves", chap 2, Wiley Interscience, New York, 1974
12 I Tsolovski, Chr Minchev, E E Senderov and V Penchev, „Zeolites, Studies in Surface Science and Catalysis" (B Drzaji, S Hocevar and S Pejovic, Eds), Elsevier 1985 (p. 377).
13 B. Wichterlova and P Jiru, *React Kinet Catal Lett*, **13**, 197 (1980)
14. L S Singer, D N Stamires, *J Chem Phys*, **42**, 3299 (1965)
15. B D Mc Nicol, and G D Pott., *J Catal*, **25**, 223 (1973)
16 V K Nestorov, I. D Mrkheikin, Y S Khodakov, V B Kazauskii and K. V. Minacev, *Kinet Katal*, **14**, 1348 (1972)

17 I Ursu, *Rezonanța Electronică de Spin*, chap 8, Ed Acad R S R , 1965
18 G A Ozin, M D Baker, J Godberg and Wu Shihua, *J Am Chem Soc* , **107,** 1955 (1985)
19 E Trif and Al Nicula, *Phys Stat Sol (b)*, **133.** 683 (1986)
20 E Trif and Al Nicula, *Proc 7-th S C A* , Bucharest, sept 1985 CIP Press Romania 1986 (p 485)
21 J Kliava, *Phys Stat Sol (b)*, **134,** 411 (1986)
22 P H Kasai, K J Bishop Jr , *J Phys Chem* , **81,** 1527 (1977)
23 R L Garten, W N Delgass and M Boudart, J Catal , 18, 90 (1970)
24 S Hidaka, A Iino, T Mibuchi, K Nita, N Yamazoe, *Chem Lett* , 1213 (1986).
25. D L Griscom, *J. Non-Cryst Sol* , **40,** 211 (1980).

STUDIA UNIV BABEŞ-BOLYAI, PHYSICA, XXXIII, 1, 1988

CHEMICAL DEPOSITION OF PbSe THIN FILMS AND THERMAL ANNEALING EFFECTS

AL. DARABONT*, P. FITORI* and L. P. BIRÓ*

Dedicated to Professor IOAN URSU on his 60 th anniversary

Received: April 20, 1988

ABSTRACT. — A method of growing photoconductive PbSe thin films on glass substrates by chemical deposition using selenourea and lead citrate complex is given An *in situ* spectrophotometric method is presented for the study of the thin film deposition Six distinct stages are identified in the deposition reaction The effect of thermal annealing in air at 350 °C on the photoconductive behaviour of the PbSe thin films is also investigated

1. **Introduction.** Chemical thin film deposition is a problem of current interest because of the increasing number of thin film applications and relative simplicity of the deposition technology A particular interest has been shown for the chemical deposition of semiconductor thin films, like PbSe photoconductors, for detection of IR radiation in spectral range of 3—5 μm PbSe films are used as high sensitivity IR detectors for the mentioned spectral range if the deposition on glass substrates is made by one of the following methods : vacuum evaporation, epitaxial deposition, or chemical deposition from aqueous solutions [1, 2, 3].

In a previous work [4] we described our method of growing photoconductive PbSe thin films on glass substrates by chemical deposition using sodium selenosulfate as selenium ion source.

The formation of PbSe films from solutions on a substrate is determined mainly by the chemical reaction kinetics between Pb^{2+} and Se^{2-} ions We were interested in the controlled film formation and this was achieved by severe component concentration regulation.

We are describing now our procedure to prepare PbSe films by homogeneous precipitation from aqueous solutions using selenourea as selenium ion source.

Pb^{2+} ions were taken in citrate complex form in weak alkaline medium (pH . 9,5).

2. **Experimental details.** 2 1 *Preparation of selenourea* selenourea was obtained by following the diagram in Fig 1 First was prepared a cyanamide solution by the continuous carbonation of a cooled aqueous calcium cyanamide slurry maintaining the pH at 6 0—6.5 [5] This solution was concentrated in a rotating evaporation system and the cyanamide was extracted in a methyl-

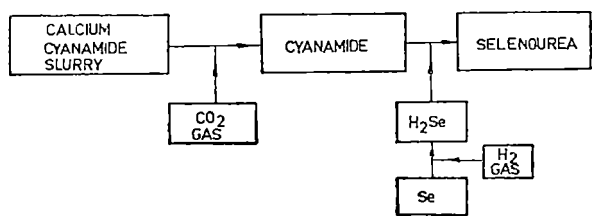

Fig 1 Technological diagram for selenourea preparation.

* *Institute of Isotopic and Molecular Technology, 3100 Cluj-Napoca, P O Box 700, Romania*

ethyl cetone solvent Selenourea was obtained in an etheric solution of cyanamide by the chemical reaction between cyanamide and H_2Se in presence of a small amount of NH_4OH [6] The H_2Se was obtained from elementary Se and H_2 gas in a furnace at 250 °C Later we obtained selenou Mreame too frorck—Schuchard cyanamide of synthesis grade

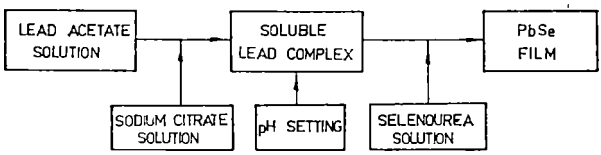

Fig 2 Technological diagram for PbSe film deposition

2 2 *The deposition of PbSe films*: the deposition of PbSe films from aqueous solutions containing selenourea may be achieved following the diagram in Fig. 2

The deposition procedure and the experimental laboratory setup were the same as in our previous work [4]

2 3 *Spectrophotometric method in thin film deposition study* The properties of thin, polycrystalline films are strongly connected with the history of the film growing It has been shown that the photoconductive behaviour exhibit a strong dependence on their microstructure [7, 8] The first attempts to use the attenuation of a light beam due to the deposition taking place in the reaction vessel [9, 10] yielded some data regarding the incubation period and the autocathalitical stage of the deposition reaction

Our intention was the study of the film deposition and the volumic precipitation as well, and for this reason the intensity of the emergent light was measured in a direction parallel to the incidence direction

An UV—VIS Specord (Carl—Zeiss—Jena) was used in the range $30-12\,5\times10^3$ cm^{-1} The reaction mixture was measured in comparison with the lead complex solution used to prepare it Both selenourea and selenosulphate using depositions were studied

The extinction of the reaction mixture was recorded at every 3 minutes From time to time substrates were taken out from the reaction mixture, prepared simultaneously with one used in the cell of the spectrophotometer, and extinction measurements were made on the substrates covered with the PbSe films [11]

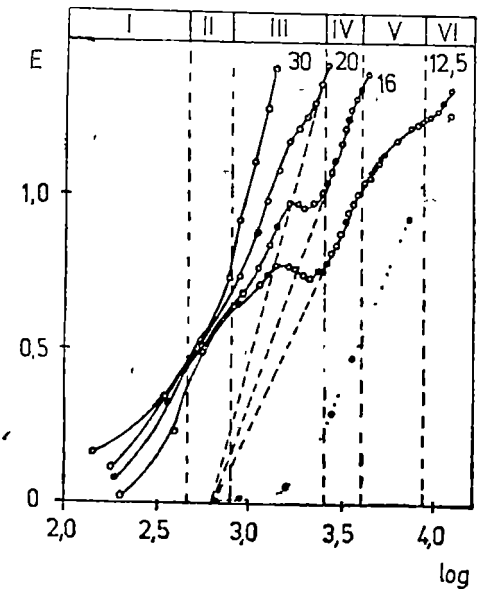

Fig 3 Variation of the extinction of the reaction mixtures vs. the logarithm of the reaction time for four values of $1/\lambda$ The dotted line represents the variation of the extinction of the substrates covered with PbSe measured at $12\,5\times10^3$ cm^{-1}

Fig 3 gives the variation of the measured extinction at several wave-numbers plotted vs. the logarithm of the elapsed reaction time The fact that the dotted line corresponding to the extinction values measured at $12\,5\times10^3$ cm^{-1} on the deposited PbSe films is parallel to the straight segments of stages IV and VI shows that the reaction take place identically in the deposition vessel and the cell of the spectrophotometer

2 4 *Thermal annealing of the PbSe films*· As-grown PbSe films were subjected to a sensitization in order to improve photoconductive behaviour The most significant effect is reported in the case of sensitization in air or oxygen [12—15]

The films were placed in a quartz boat in an open, horizontal furnace preheated to 350 °C. The annealing time ranges from minutes to days. After the treatment the resistance and the photoresponse of the films were measured The experimental data for one set of samples plotted vs treatment time are shown in Fig. 4 [16]

This behaviour was found to be characteristic of all the chemically deposited films we studied. In the first few minutes a very sharp drop in resistance and photoresponse takes place, this is followed in the range of 6—8 hours by a simultaneous maximum in resistance and photoresponse, a second maximum of the resistance and the photoresponse is evidenced in the range of 24—26 hours The maximum photoresponse on untreated films is obtained at 1 5 — 1 8 μm, while the treatment shifts this maximum to 3,6 μm

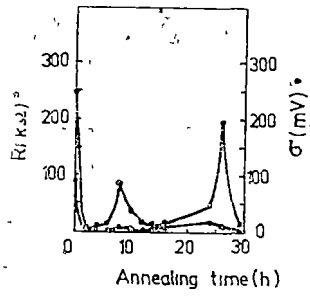

Fig 4 The variation of resistance $R(0)$ and photoconduction $\sigma(\ )$ vs annealing time

3 Results and discussions. 3.1. Using the procedure described above, we obtained photoconductive films The quality of the films was influenced by several factors

— the addition time of lead acetate and selenourea solutions to a dilute reaction mixture at a given pH value and temperature of the bath with glass substrates in it influenced the adherence and the thickness of the films; continuous addition of the reaction components gave better results, microstructure of the films depends on this parameter.

The evolution of the reaction using selenourea is faster than that of the reaction using sodium selenosulphate, so that the slow addition of the reactants is desired for the formation of thick films with good microstructure

— the deposition time has a direct influence on the thickness and on the microstructure, longer deposition times yielded better results For example in approx. 2 hours one can reach a thickness up to 0.8 μm

— the stability of the lead complex and selenourea determine a relatively narrow pH domain 9 3—9.7

— in order to control the dimensions of the crystallites forming the deposited film, the reactant concentrations ought to be near 10^{-1} M.

— at lower temperatures the reaction was slow, the film adherence was weaker and longer deposition times had to be used in order to achieve the desired thickness.

— it was found that the age of the solutions influences the deposition; a newly prepared lead complex solution reacts rapidly, while a few days old complex solution slowly. Selenourea solutions were always freshly prepared from solide selenourea because of the instability properties of the selenourea solutions.

3 2. As it may be seen in Fig. 3, there are six distinct stages in the development of the deposition reaction.

Stage I is the so called autocathalitical stage [10] characterized by a strong acceleration of the process due to a fast increase in the number of the existing cathalitical sites.

Stage II the volumic precipitation reaches a kind of dynamic equilibrium, all the curves plotted tend toward the same values This indicates that the number of particles of different sizes floating in the liquid is uniformly distributed all over the entire size range of particles producing a significant light scattering.

Stage III is a stage of transition from a dominantly volumic precipitation to the growth of the film. In this stage formation of a continuous film takes place from the nuclei produced at the end of stage II.

Stage IV is dominated by fast growth of the film An extremely thin film was observed on the substrate; the films are bright and mirror like microscopical observation did not show grains grown out from the smooth surface of the film.

Stage V: due to the lowering of the concentration of the reactants the supersaturation reaches the critical value at which a transition takes place from "layer-like" growth to "island-like" growth.

Stage VI: the growth is characterized by an "island-like" mechanism, the films exhibit a rough surface of together-grown grains. The "valley-hill" profile is fairly well evidenced by microscopical observation in dark field illumination at a magnification of 650×.

3.3. A possible explanation for the first sharp drop in resistance may be that after preparation the film is considered as consisting of an amorphous tissue in which small single crystals are uniformly distributed. The amorphous material surrounding the small crystals causes the high resistance values measured on asgrown films. The amorphous PbSe is in a metastable state till the activation energy needed for the structural transition is supplied to it. We observed that amorphous PbSe exists from room temperature to about 220 °C.

The shift of photoresponse maximum from 1 6—1.8 μm on untreated samples to 3.6 μm after treatment is in accordance with the size quantization effect reported in [17] for PbSe and HgSe. The amorphous PbSe may be regarded as constituted of crystallites with diameter less than 50 Å; the carriers injected from "crystalline islands" need a supplementary activation energy to produce the photoconductive effect in the amorphous substance [18] surrounding the "crystalline islands" and this causes the shift of the photoconduction maximum to lower wavelengths. After the crystallization of the amorphous PbSe and the recrystallization due to the thermal treatment, one gets the value reported in the literature for PbSe photoconduction maximum, 3.8 μm [19].

4 **Conclusions.** Chemical deposition procedure of PbSe films in a lead citrate — selenourea bath is a complex process which may be monitored keeping all reaction parameters under control. Selenourea is a quite instable substance and for this reason the deposition technology needs more attention (rigurously pH control, light-tight conditions during selenourea solution adding). Identification of distinct stages in the carrying on the deposition reaction by spectrophotometric method suggest the possibility of using it for deposition monitoring if real-time curve computation is used. The method permits the study of the influence of several factors on the going through of the deposition reaction

There were identified two different types of processes governing the phenomena taking place when heating chemically deposited PbSe films in air at 350°C: a fast crystallization of the amorphous material, producing the charp resistance and photoresponse drop and slow processes of diffusive nature which cause the resistance and photoresponse maximum at (6—8) hours and (24—26) hours, respectively

REFERENCES

1. D. G. Coates, *J Electrochem Soc*, **110,** 174 (1963)
2. R. B. Schoolar, J. R Lowney, *J Vac Sci Technol*, **8** (1), 224 (1971)
3. C J Milner, B N Watts, *Nature*, **163,** 322 (1949)
4. Al Darabont, P Fitori, L P Biró, *Studia Univ Physica*, **XXXI,** 2, 50 (1986)
5. S. A Miller, B. Bann, *J Appl Chem*, **6,** 89 (1956)
6. Houben-Weyl, *Methoden der Organischen Chemie*, 4 Auflage, Eugen Muller Vol 9, x1187
7. W D Lawson, F A Smith, A S Young, *J Electrochem Soc*, **107,** 206 (1960)
8. V I Petrov, A V. Prokhorov, E A Yunovich, *Fiz Techn Poluprov*, **18,** 484 (1984)
9. R A Zingaro, D O Skovlin, *J Electrochem Soc*, **111,** 42 (1964)
10. A B Lundin, G A Kitaev, *Izv Akad Nauk SSSR Neorg Mat*, **1,** 2107 (1965)
11. L P Biró, P Fitori, Al Darabont, *7-th Int Conf on Thin Films, Dec* 7—11, 1987, New-Delhi, India
12. B N McLean, *U S Patent* 2, 997, 409 Aug 22 1961
13. T M Johnson, *US Patent* 3, 178, 312 April 13, 1965
14. R M Cândea, R Turcu, P Mărgineanu, D Dădârlat, *Phys Status Solidi A*, **96,** 337 (1986)
15. R M Cândea, R. Turcu, G Borodi, I Bratu, *Phys Status Solidi A*, **100,** 149 (1987)
16. L P Biró, Al Darabont, P Fitori, *Europhysics Lett*, **4** (6), 691 (1987)
17. J. M Nedeljkovic, M T Nenadovic, O J Micic, A J Nozik, *J Phys Chem*, **90,** 12 (1986)
18. N F Mott, E A Davis, *Electronic Processes in non-Crystalline Materials*, Clarendon Press, Oxford, 1979, p 200, 209
19. R. Dalven, *Infrared Phys*, Vol 9, Pergamon Press, London, 1969, p 147.

STUDIA UNIV BABEŞ-BOLYAI, PHYSICA, XXXIII, 1, 1988

ARGON OF HIGH PURITY

F. ATANASIU*, A. RĂDOI*, V. ALMĂŞAN*, L. MUREŞAN*, M. ATANASIU* and S. DRONCA*

Dedicated to Professor IOAN URSU on his 60 th anniversary

Received November 15, 1987

ABSTRACT. — The most common methods for argon production and purification are summarized The removal of some trace impurities from refined argon is also described A laboratory plant for argon high purification is presented

I. Introduction. Argon has been largely employed in technology and scientific research from the beginning of its availability First, it was used as shielding gas for the inert-gas-shielded arc welding and to provide an inert atmosphere in which chemically reactive materials, such as hot titanium and transistor-grade-silicon, could be handled without contamination Most incandescent lamp bulbs are filled with argon containing a little nitrogen and most fluorescent lamps are filled with argon-krypton mixtures New applications of argon are in the field of laser technology, determination of the age of rocks, cryogeny, as filling gas for radiation detectors, as raw material for stable isotopes separation, (^{36}Ar, ^{38}Ar), as carrier gas in gas-chromatography, a s o [1]

Almost 1% of the earth's atmosphere is argon, and so, industrially, this gas is produced by the liquefaction and rectification of air A small quantity of argon is produced by distillation of the bleed-off gas of the ammonia plants, containing hydrogen, nitrogen and argon [2]

II. Methods for argon production and purification. The liquefaction and distillation of air results in a gas containing 97—98% argon [3]. At this level of purity, the crude argon contains oxygen and nitrogen as the main impurities. The oxygen is usually removed by catalytic combustion with hydrogen. The combustion process reduces the oxygen content to a few ppm by volume and leaves about 1% hydrogen and 1% nitrogen as the major impurities in the resulting argon [1, 2] Another usual method to remove the oxygen is by adsorption on Linde molecular sieve Type 4A [1].

Refining the "crude" argon by rectification one can obtain 99 996% purity gas or better [1, 4] A purity of 99 996% corresponds to total impurities of 40 ppm Actually, the total impurities are almost always less than this, their concentrations are usually in the following ranges. 1 to 10 ppm nitrogen, 0 to 5 ppm oxygen, 0 to 5 ppm carbon dioxide, about 1 ppm hydrogen, 0 to 6 ppm moisture [1, 4, 5].

Special purification methods offer research grade argon which has a purity of 99 999—99.9999% [1, 5, 6].

* *Institute of Isotopic and Molecular Technology 3400 Cluj-Napoca, Romania 5, P.O. Box 700*

III. Removal of trace level impurities from argon. Typical trace level impurities in 99.99—99 995% grade argon are. oxygen, nitrogen, hydrogen, carbon dioxide, methane and moisture [3, 7].

Most common methods for oxygen removal from primarily refined argon are by catalytic combustion with hydrogen added [1], by adsorption on molecular sieve, or by passing the gas on activated charcoal [8], on copper and activated nickel (which both reduce also the moisture level) [3], on MnO [9], on Al—Mg or Ca—Mg alloys at temperatures between 250—450°C [10], on Ba [11, 12] and on uranium furnaces which can reduce the nitrogen content also at 900°C [13].

The removal of nitrogen traces is accomplished by adsorption on molecular sieves [1, 3, 14, 15], or by absorption in lithium, magnesium and calcium getters [1, 3]

The water vapors can be reduced on molecular sieves moisture traps at liquid nitrogen temperature [1, 3], or by using chemical active media like KOH, P_2O_5 and calcium chloride [3].

The methane traces are removed in the same time by the catalytic combustion of oxygen; passing through copper oxide or calcium furnaces [1], or by adsorption through synthetic dehydrated zeolitic sodium (calcium) aluminium silicate at low temperatures [16].

Hydrogen level is reduced on copper oxide and palladium at 250—300°C [3].

Carbon dioxide is often absorbed by passing the gas through sodium or potassium hydroxide solutions [17].

IV. Laboratory plant for ultrapure argon production. Using the experimental sequence presented in Fig. 1, one obtains ultrapure argon with a purity of minimum 99.999% from industrial "crude" argon which had a purity of

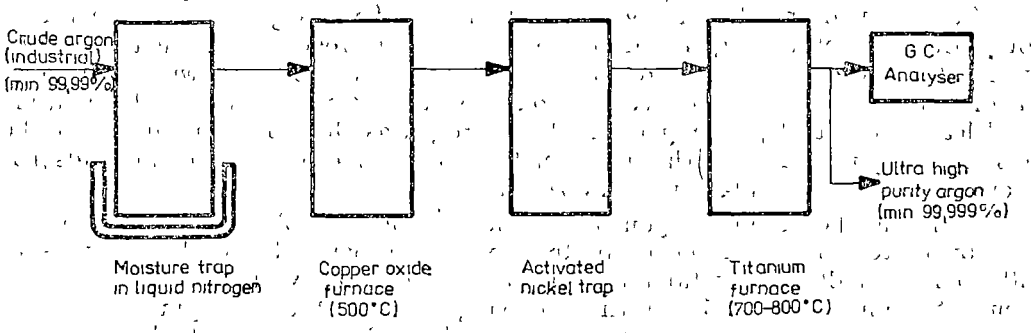

Fig 1. Schematic diagram of a laboratory plant for ultrapure argon production

min. 99.99%. The contents of the main impurities are: max. 1 ppm hydrogen, max. 1 ppm nitrogen, max. 1 ppm methane, about 2 ppm moisture, about 2 ppm oxygen and max. 1 ppm carbon dioxide, [6, 18]. The analyses of trace level impurities was accomplished on a Varian Aerograph 1732.

REFERENCES

1 „Argon, Helium and the Rare Gases", vol. I—II, ed G A Cook, Interscience Publishers, J. Wiley and Sons, (1961).
2 M Ruhemann, „The Separation of Gases", 2nd ed., Oxford, New York, (1949).
3 A Klemenc, „Die Behandlung und Reindarstellung von Gasen", Springer-Verlag, (1948).
4 British Oxygen Company, „Special Gases Catalogue" (1985).
5. UCAR, Union Carbide, „Specialty Gases and Related Equipment, Catalogue" (1986)
6 F. Atanasiu, A Rădoi, M Atanasiu, Al. Fărcaş, V. Almăşan, L. Mureşan, S Dronca, *CSEN—ITIM, Report, sept.* (1987)
7 G Muller, G Gnauck, „Reinste Gase", VEB Deutscher Verlag der Wissenschaften, Berlin (1965).
8 * * *, *Patent, U S*, 2, 962, 343, Nov, 29, (1960).
9 * * *, *Soobschmiya Akad Nauk Gruzn SSR*, **25**, 677 (1960).
10 * * *, *Patent, Fr*, 1, 150, 662, Nov 20 (1958).
11. D S Gibbs, H T. Svec and H E. Harrington, *Ind. Eng. Chem.*, **48**, 289 (1956).
12 W. R Bennett, *Jr*, *Rev Sci Instr*, **28**, 1092 (1957).
13 G H Dicke, H M. Crosswhite, *J. Opt. Soc. Am.*, **42**, 433 (1952).
14 * * *, *Patent, Czech.*, 107,947 (1963)
15 R M Barrer, *Brit Chem Eng*, **4**, No 5, 267 (1959).
16. *J W Armond*, to the British Oxygen Company, *U.S. Patent*, 2, 893, 512, July 7 (1959).
17 J. Janak, *Chem Listy*, **47**, 464 (1953)
18 V Almăşan, A Rădoi, F Atanasiu, L Mureşan, M Atanasiu, S Dronca, *CSEN—ITIM, Report, Dec* (1987)

STUDIA UNIV BABEŞ—BOLYAI, PHYSICA, XXXIII, 1, 1988

STRUCTURAL AND MAGNETIC BEHAVIOUR OF THE $Dy_2Ni_{17-x}Al_x$ INTERMETALLIC SYSTEM

IULIU POP*, NATALIA DIHOIU and OLIVIA POP*****

Dedicated to Professor IOAN URSU, on his 60th anniversary

Received June 27, 1988

Abstract. — The structural and temperature dependence of the reciprocal magnetic susceptibility were investigated for the intermetallic system $Dy_2Ni_{17-x}Al_x$ ($0 \geqslant x \geqslant 17$) A new intermetallic compound Dy_2Al_{17} was obtained It was pointed out that the isostructural intermetallic compounds Dy_2Ni_{17} and Dy_2Al_{17} give rise to a continuouse solid solutions series The lattice parameters *a* and *c* monotonously change with x nickel concentration From the magnetic point of view, the investigated intermetallic compounds with the general formula, $Dy_2Ni_{17-x}Al_x$ are ferrimagnetic and their behaviour is interpreted on the basis of the Yafet and Kittel model The new intermetallic compound Dy_2Al_{17} is paramagnetic and obeys a Curie—Weiss law, with the negative paramagnetic Curie temperature $\theta p = -90$ K

1 **Introduction.** The intermetallic compounds Dy_2Ni_{17} and Dy_2Al_{17} are isostructural and give rise to a continuous solid solutions series with the general formula $Dy_2Ni_{17-x}Al_x$ The compounds crystallize in the hexagonal Th_2Ni_{17} structure type In a previouse paper [1] we have investigated the magnetic behaviour in the ordered state and also in the paramagnetic state for some of these compounds, namely $Dy_2Ni_{17-x}Al_x$, with $x = 0, 0\,2, 0\,4, 0\,6, 1$ The results were interpreted on the basis of the magnetic interactions Ni—Ni and Ni—Dy, taking into account the positions of the magnetic ions in the lattice. There are in these compounds four crystallographically inequivalent sites for Ni atoms (4f, 6g, 12j and 12k) and two for Dy atoms (2b and 2d) [2] The Ni atoms on 6g, 12k and 12j sites give rise to identical hexagons and between the atomic planes formed by these three Ni sites are located the Ni atoms on 4f sites The Dy atoms are located in the center of the hexagons formed by Ni atoms on 12j sites The ground state at 0 K is formed from three collinear sublattices A, B and C The sublattices A and B comprises the spins on 4f sites (sublattice A) and 6g, 12j and 12k sites (sublattice B) The sublattice C compricces the Dy atoms on 2b and 2d sites Because the B—C interaction is dominant, the sublattices B and C will be magnetized in opposite directions, so the sublattice C is parallel to sublattice A When the triangular arrangement in the B sublattice appears, the spins on C sites fall into two similar sublattices, whose magnetizations also form a triangular arrangement due to the strong B—C interaction, their resultant being antiparallel to that of B sublattices and consequently parallel to A So the magnetic behaviour for these intermetallic compounds may be well explained by Yafet and Kittel theory [3]

* *University of Cluj-Napoca, Faculty of Mathematics and Physics, 3400 Cluj-Napoca, Romania*
** *University of Braşov, 2200 Braşov, Romania*
*** *Polytechnical Institute of Cluj-Napoca, 3400 Cluj-Napoca, Romania*

2 **Experimental.** The compounds $Dy_2Al_{17-x}Ni_x$ ($0 \geqslant x \geqslant 17$) were prepared by arc-melting stoichiometric amounts of the elements in an argon atmosphere. The purity of the starting elements was 99 9% for Dy and Ni and 99 99% for Al. The samples were checked for homogeneity by X-ray analysis and only single phases were found. The magnetic susceptibility was measured between 100 and 1,100 K with a Weiss-Forrer type o magnetic balance, with a sensitivity of 10^{-8} cm /g [4] in a magnetic field of 9,500 G intensity

3 **Results and discussion,** The X-ray measurements were performed on a TUR-M-62 equipment, using the Debye—Scherrer method on powdered samples For the investigated intermetallic pseudobinary compounds the lattice parameters *a*, *c* and their ratio *c/a* are listed in the Table 1.

Table 1

Intermetallic compounds	Lattice parameters		Ratio
	a, Å	*c*, Å	*c/a*
Dy_2Al_{17}	11 788	11.322	0,9604
$Dy_2Ni_2Al_{15}$	11.322	10 314	0 9109
$Dy_2Ni_4Al_{13}$	10 842	9 667	0.8916
$Dy_2Ni_6Al_{11}$	10 395	9 409	0 9051
$Dy_2Ni_8Al_9$	9 925	9 188	0 9257
$Dy_2Ni_{10}A_7$	9 451	9 035	0 9559
$Dy_2Ni_{12}Al_5$	8 980	8 850	0 9855
$Dy_2Ni_{14}Al_3$	8 536	8 704	1 0916
$Dy_2Ni_{15}Al_2$	8 311	8 770	1 0552
$Dy_2Ni_{16}Al$	8 045	8 677	1 0785
$Dy_2Ni_{16\ 2}Al_{0\ 8}$	7 995	8 672	1 0846
$Dy_2Ni_{16\ 4}Al_{0\ 6}$	7.954	8 669	1 0898
$Dy_2Ni_{16\ 6}Al_{0\ 4}$	7 902	8 666	1 0966
$Dy_2Ni_{16\ 8}Al_{0\ 2}$	7 851	8 663	1 1034
Dy_2Ni_{17}	7 828	8 660	1 1062

As one can see from Fig 1, the lattice parameter *a* decreases linearly with the nickel concentration increase while the lattice parameter *c* decreases monotonously The concentration dependence of the lattice parameters ratio *c/a* is given in the figure 2 One can see that the curve has a minimum for $x = 4$

The monotonouse variation of the lattice parameters with the concentration x in the compounds formula shows that the system $Dy_2Al_{17-x}Ni_x$ forms a continuous solid solution series

The temperature dependence of the reciprocal magnetic susceptibility for the intermetallic new compound Dy_2Al_{17} and for the pseudobinary intermetallic compounds $Dy_2Ni_{17-x}Al_x$, with $x = 1$; 2 is given in the Fig. 3 As one can see the magnetic susceptibility for the Dy_2Al_{17} obeys the Curie—Weiss law with the negative paramagnetic Curie temperature $\theta p = -90$ K, suggesting a possible antiferromagnetic ordering of the dysprosium magnetic moments at lowered temperatures The effective maguetic moment per formula unit determined from the Curie—Weiss constant of 15.144 μ_B is in very good agreement with that calculated taking into account the values of 10 64 μ_B/Dy^{+3} and 1 64 μ_B/Ni atom. For the pseudobinary intermetallic compounds the reciprocal magnetic susceptibility is linear at high temperatures, but is not linear

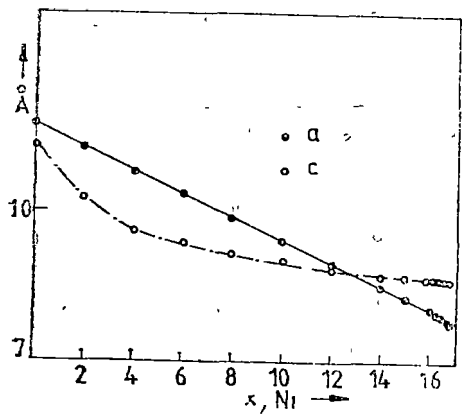

Fig. 1. Nickel concentration dependence of the lattice parameters

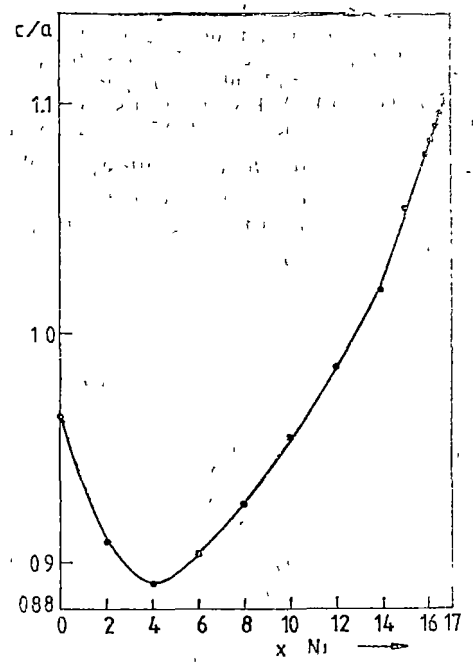

Fig 2 Nickel concentration dependence of the c/a ratio

at lower temperatures suggesting the ferrimagnetci ordering at low temperatures, as on can see from the Figs 3, 4 and 5 for the all investigated compounds

From the linear part of the curves $1/\chi(T)$ we have determined the effective magnetic moments per formula unit As one can see from the Table 2. the calculated and the experimental determined values are in good agreement.

Table 2

Intermetallic compounds	Effective magnetic moment per formula unit, μ_B calculated	determined	Effectiv magnetic moment per nickel atom μ_B
Dy_2Al_{17}	15 146	15 144	—
$Dy_2Ni_2Al_{15}$	15 322	15 264	1 64
$Dy_2Ni_4Al_{13}$	15 400	15 434	1 67
$Dy_2Ni_6Al_{11}$	15 574	15 555	1 65
$Dy_2Ni_8Al_9$	15 745	15 726	1 71
$Dy_2Ni_{10}Al_7$	15 915	15 910	1 70
$Dy_2Ni_{12}Al_5$	16 084	16 044	1 62
$Dy_2Ni_{14}Al_3$	16 250	16 290	1 64
$Dy_2Ni_{15}Al_2$	16 332	16 396	1 62
$Dy_2Ni_{16}Al$	16 415	16 419	1 65

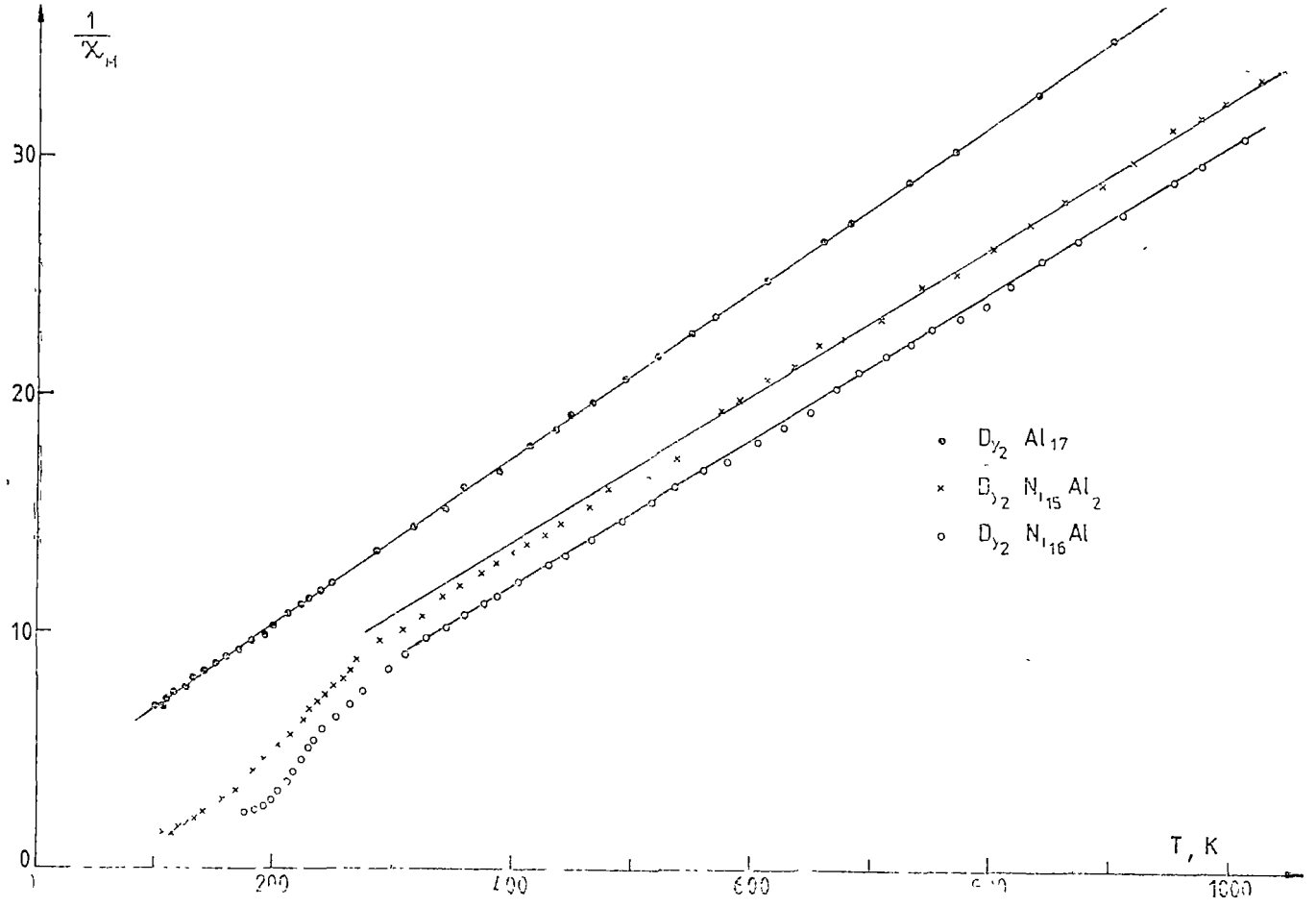

Fig 3 Temperature dependence of the molar reciprocal magnetic susceptibility for Dy_2Al_{17}, $Dy_2Ni_{15}Al_2$ and $Dy_2Ni_{16}Al$ intermetallic compounds

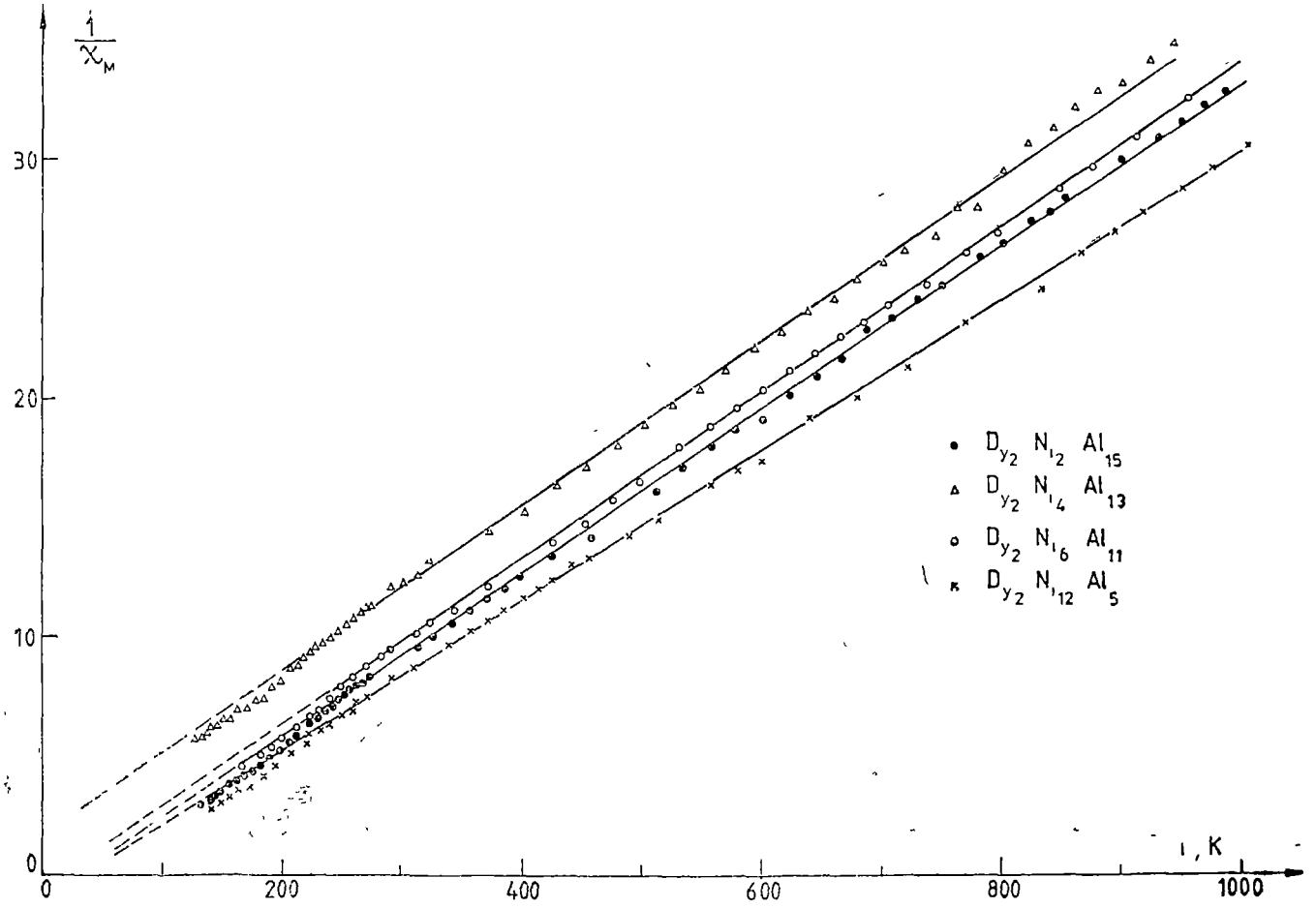

Fig 4 Temperature dependence of the molar reciprocal magnetic susceptibility for $Dy_2Ni_2Al_{15}$, $Dy_2Ni_4Al_{13}$; $Dy_2Ni_6Al_{11}$; $Dy_3Ni_{12}Al_5$ intermetallic compounds

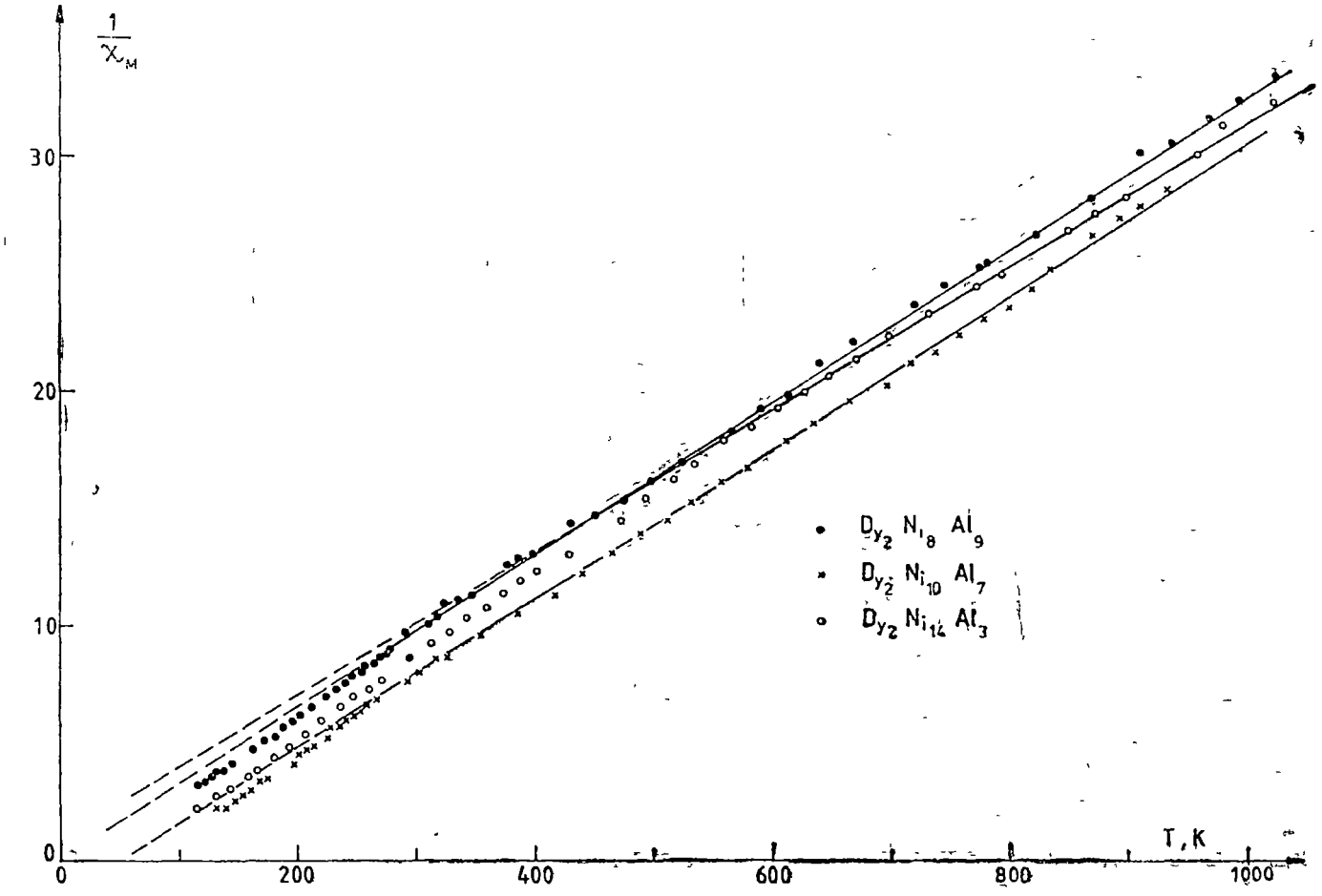

Fig. 5 Temperature dependence of the molar reciprocal magnetic susceptibility for $Dy_2Ni_8Al_9$, $Dy_2Ni_{10}Al_7$, Dy_2NiAl_3 intermetallic compounds

In the last column are given the effective magnetic moments values, determined per nickel atom by taking into account 10 64 μ_B/Dy^{3+}. All the determined values are in good agreement with the experimental value per nicke atom for pure nickel metal of 1 64 μ_B.

4. **Conclusions,** The intermetallic system $Dy_2Ni_{17-x}Al_x$ give rise to a continouse series of solid solutions. The system crystallizes in a hexagonal lattice of Th_2Ni_{17} type. The intermetallic compound Dy_2Al_{17} is a new compound, isostructural with Dy_2Ni_{17}.

The lattice parameters a and c continously changes with the x nickel or aluminium concentration.

The intermetallic system $Dy_2Ni_{17-x}Al_x$ is ferrimagnetic, excepting Dy_2Al_{17} which is paramagnetic in the investigated temperature range, obeying the Curie—Weiss law with negativ paramagnetic Curie temperature, $\theta p = -90$ K

In the paramagnetic regime for the more nickel concentrated compounds the temperature dependence of the reciprocal magnetic susceptibility obeys a Néel law. For the less nickel concentrated compounds only a small nonlinearity is observed at law temperatures suggesting the ferrimagnetic order.

REFERENCES

1. M Coldea, I Pop and N Dihoiu, *J M.M M*, 31—34 (1983).
2. N M Henry and K Lonsdale, „International Tables for X-Ray Crystallography", vol 1 (The Kynach Press, Birmingham, England, 1952) p 304.
3 Y. Yafet and C Kittel, *Phys Rev.*, **87** (1952) 290.
4 I. Pop and V I. Tchetchernijov, *Pribory Tekh. Eksp*, **5** (1964) 180

STUDIA UNIV BABEŞ-BOLYAI, PHYSICA, XXXIII, 1, 1988

RECENZII

Laser Spectroscopy of Solids, W M Yen and P M Selzer (Eds), Second Edition, Springer—Verlag, Berlin—Heildelberg, 1986, pp

The theoretical and experimental study of optical properties, which has known wide development mainly by employing laser as an exciting source, is continuously spurred by the advanced technologies that require ever more efficient optical materials

This book (second, revised edition) covers a survey of the spectroscopic properties of insulators as derived from application of tunable laser spectroscopic techniques. An outline of the optical spectroscopy of ions and molecules in solids is given in Chapter 1, which serves as a background for the following chapters. Further on, in Chapters 2 and 3 the microscopic and macroscopic aspects of the theory of dynamics of optically excited states with emphasis on ion-ion interactions, which are responsible for optical energy transfer in condensed phases, are considered. Chapter 4 reviews the recently developed experimental methods that allow the observation of the various dynamical processes. Much stress is laid on the fluorescence line narrowing technique — a very versatile method for observing both relaxation and energy migration Investigation of the optically active ions in insulator by laser spectroscopic technique is considered in Chapter 5 The next chapters relate the same technique to the study of fluorescence spectroscopy in glasses. Finally, aspects on processes entailing relaxation, quencing, and transfer out of excited optical states in ordered and disordered solids are brought to light in the final chapter.

The material is organized in such a way that the student obtains a good understanding of the properties of insulators as derived from the application of tunable laser spectroscopic techniques, as he gets familiarized with this important tool provided by laser spectroscopic techniques.

The book can successfully be referred to by either first time domain-contacting students and by specialists, who all encounter here a relevant up-to-date documentation on both experimental techniques and theoretical researches.

TRAIAN ILIESCU

K. Shimota, **Introduction to Laser Physics,** Second Edition, Springer—Verlag, Berlin—Heidelberg—New York—London—Paris—Tokyo, 1986.

Lasers have brought an actual revolution in science and technique. New fundamental and applicative developments in physical optics, quantum electronics, non-linear optics and spectroscopy have emerged. Fundamental research is today unconceivable without the use of lasers, nor is it possible to solve varied technical and technological problems.

The author of this book, who has been involved in laser research, considers here both the basic concepts and the theoretical aspects of lasers and the effects induced by laser radiation. After reviewing, in Chapter 1, the types of lasers and the spectral range covered by the laser radiation emitted by these, in the next two chapters the concept of coherence and the electromagnetic theory of the light applied to lasers are discussed. The processes of the absorption and emission of light described in Chapter 4 are meant to pave the way for the reader so as to better understand the principles of lasers, which make the core of Chapter 5. By resorting to the rate-equation theory, the interaction between the light and atoms in the resonators under the influence of pumping and relaxation is considered in Chapter 6, while Chapter 7 is focused on the interaction of the atom with the coherent light when it aquires a dipole moment of certain fixed phase with respect to the optical field The final two Chapters, (8 and 9), in a semiclassical treatement way, deal with the non-linear effects of the coherent light and the theory of laser ocillations

An easy mathematical language is employed in the book, the somewhat difficult aspects beeing treated in details. Contribution to enforcement of the exposed ideas is provided by each chapter-end problems, as well as by the answers and solving given in the end

This is a useful refference book both to undergraduate students and to those directly involved in researches on lasers.

TRAIAN ILIESCU

ÎNTREPRINDEREA POLIGRAFICĂ CLUJ,
Municipiul Cluj-Napoca, Cd. nr. 258/1988

În cel de al XXXIII-lea an (1988) *Studia Universitatis Babeș-Bolyai* apare în specialitățile:

matematică
fizică
chimie
geologie-geografie
biologie
filosofie
științe economice
științe juridice
istorie
filologie

In the XXXIII-rd year of its publication (1988), *Studia Universitatis Babeș-Bolyai* is issued as follows:

mathematics
physics
chemistry
geology-geography
biology
philosophy
economic sciences
juridical sciences
history
philology

Dans sa XXXIII-e année, *Studia Universitatis Babeș-Bolyai* paraît dans les spécialité :

mathématiques
physique
chimie
géologie-géographie
biologie
philosophie
sciences économiques
histoire
philologie

43 904

Abonamentele se fac la oficiile poştale, prin factorii poştali şi prin difuzorii de presă, iar pentru străinătate prin „ROMPRESFILATELIA", sectorul export-import presă, P. O. Box 12—201, telex. 10376 prsfir, Bucureşti Calea Griviţei nr. 64—66.

Lei 35